May 2020

Integrated Additive and Subtractive Manufacturing of Glass Photonic Sensors for Harsh Environment Applications

Qi Zhang
Clemson University, qzhang9@g.clemson.edu

INTEGRATED ADDITIVE AND SUBTRACTIVE MANUFACTURING OF GLASS PHOTONIC SENSORS FOR HARSH ENVIRONMENT APPLICATIONS

A Dissertation
Presented to
the Graduate School of
Clemson University

In Partial Fulfillment
of the Requirements for the Degree
Doctor of Philosophy
Electrical and Computer Engineering

---

by
Qi Zhang
May 2020

Accepted by:
Dr. Hai Xiao, Committee Chair
Dr. Fei Peng
Dr. Kuangching Wang
Dr. Lin Zhu

ABSTRACT

Research and development in advanced manufacturing for sensors and devices fabrication is continuously changing the world, assisting to giving sensing solutions in the physical, chemical and biological fields. Specifically, many modern engineered systems are designed to operate under extreme conditions such as high temperature, high pressure, corrosion/erosion, strong electromagnetic interference, heavy load, long reaching distance, limited space, etc. Very often, these extreme conditions not only degrade the performance of the system but also impose risks of catastrophic failures and severe consequences. To perform reliably under these harsh conditions, the materials and components need to be properly monitored and the systems need to be optimally controlled. However, most existing sensing technologies are insufficient to work reliably under these harsh conditions. Innovations in sensor design, fabrication and packaging are needed to address the technological challenges and bridge the capability gaps.

Optical fiber sensors have been widely researched and developed for energy, defense, environmental, biochemical and industry sensing applications. In general, optical fiber sensors have a number of well-known advantages such as miniature in size, high sensitivity, long reaching distance, capability of multiplexing and immunity to electromagnetic interference (EMI). In addition, optical fiber sensors are capable of operating under extreme environment conditions, such as high temperature, high pressure, and toxic/corrosive/erosive atmospheres. However, optical fiber sensors are also fragile

and easy to break. It has been a challenging task to fabricate and package optical fiber sensors with predicable performance and desired reliability under harsh conditions.

The latest advancements in high precision laser micromachining and three-dimensional (3D) printing techniques have opened a window of opportunity to manufacture new photonic structures and integrated sensing devices that deliver unprecedented performance. Consequently, the optical sensor field has quietly gone through a revolutionary transition from the traditional discrete bulk optics to today's devices and structures with enhanced functionalities and improved robustness for harsh environment applications.

Driven by the needs for sensors capable of operating in harsh environments, integrated additive and subtractive manufacturing (IASM) for glass photonics sensor fabrication process has been proposed and developed. In this dissertation, a series of high-performance optical fiber sensors were proposed and fabricated. In addition, several significant sensing measurements (e.g., pressure, temperature, refractive index variation) of the proposed sensors and structures with enhanced robustness were demonstrated in this dissertation. To realize measurement of above parameters, different working principles were studied, including mechanical deflection, light-material interaction and utilizing properties of fluidics. The sensing performance of the fabricated sensors and structures were characterized to demonstrate the capabilities of the developed IASM process on advanced manufacturing of glass photonic sensors with specific geometry and functions, and the realization for information integrated manufacturing purpose.

DEDICATION

This dissertation is dedicated to my family

ACKNOWLEDGMENTS

Upon finishing this dissertation, I would like to express my sincerest gratitude to my advisor Dr. Hai Xiao, who offered me this precious opportunity to pursue a doctoral degree at Photonics Technology Lab. What Dr. Xiao taught me is not only the academic knowledge, but also the way to become a better person that I will benefit during my lifetime. Without his encouragement, patient guidance and supports, I will not be able to complete my Ph.D. program.

I want to thank Dr. Fei Peng, Dr. Kuangching Wang and Dr. Lin Zhu for serving as my academic committee members to provide guidance on my dissertation and my research.

I am immensely grateful to all my collogues that I worked with in Photonics Technology Lab. I really appreciate their help both in my research and daily life. I enjoy the time working with them and it will be my best memory in Clemson. A special “thank you” is given to Dr. Yang Song, Dr. Jincheng Lei, Dr. Yizheng Chen and Dr. Liwei Hua. In addition, I would like to thank my friends for their help and supports all these years.

Last but not least, I would like to express my deepest gratitude to my parents and my family. I would like to thank my cousin Dr. Wenjuan Zhu for her continuous support and acting as a role model in my life. For my parents, without their continuous encouragement, endless love and unwavering support in my life, I will not be able to overcome any adversity and accomplish all the achievements.

TABLE OF CONTENTS

LIST OF FIGURES

LIST OF TABLES

CHAPTER ONE

Introduction

1.1 Nature and challenges for harsh condition sensing

Energy is required to sustain and improve quality of life [1]–[3]. The dramatic society changes and the population growth since the industrial revolution have required vast amounts of energy provided mainly by coal and petroleum [4]. In the near future, further population growth and improvements in quality of life will increase the demand for non-renewable fossil fuels and intensify the associated environmental implications. In the meantime, the high rate of fossil fuel consumption accelerates their depletion. Despite the growing supply from alternative and renewable energy sources, it is reported that we will still rely on fossil fuels for most of our energy needs until 2050 [4]. As such, to minimize the consumption of fossil fuels and make them economically and environmentally viable long terms, improvement in energy transfer efficiency and conservation are needed.

While we highly depend on conventional sources for energy generation, and to ensure that these power generation systems operate efficiently, it is known that conventional energy is mostly generated in harsh environments such as in turbines, gasifiers [5]. Some common features of harsh environment include high temperature, high pressure and chemical corrosive environment, which makes them not easy to access. At the same time, the ability to collect data and transduce signals within harsh environments will change the way we engineer engines, turbines, and gasifiers (e.g. geothermal and oil and

gas exploration). In addition, harsh-environment sensing will allow us to understand environments that are challenging to assess[6]–[8].

However, there are very limited number of sensors for harsh condition monitoring. As when applied for harsh condition sensing, more requirements will be needed, including capability of operating in high-temperature and high-pressure conditions, dependable performance, high chemical resistance, long term stability and survivability, and good robustness. Meanwhile, from the industrial/commercial perspective, easy installation, minimum maintenance and low-cost during application are also concerns. Typical conventional, commercially available and general-purpose electrical sensors have been prevented from the challenging requirements. Optical fiber sensors, composed of fused silica with high temperature resistance, may provide viable solution for sensing and monitoring in these challenging, harsh conditions [6], [9]–[16].

1.2 Fiber optic sensors

The optical fiber field has undergone tremendous growth and advancement over the past several decades [6], [9]–[17]. Initially considered as a medium of transmitting light and imagery for medical endoscopic applications, optical fibers were later widely applied as an information carrier for telecommunication applications in the mid 1960s [18]. Since then, the research and development of optical fiber in communication area has been widened immensely and become competitive [19]. As the technology advances, optical communication has proven to be the primary method to transmit huge amount of data and information with high speed and large capability.

In addition to the optical communication applications, fiber optic sensing has become widely used in different application areas for physical, chemical and biological sensing in structural health monitoring, harsh condition sensing, biological sensing and imaging areas [6], [9]–[17]. Optical fiber, which is made of fused silica, consists of fiber core, fiber cladding and outside buffer protection layer, as shown in Fig. 1.1. Considering the small amounts of doping elements in the fiber core area (like germanium-doped), the refractive index of the fiber core (n_1) will be slightly larger than the refractive index of the fiber cladding (n_2). As such, the light can propagate inside the fiber core due to the total internal reflection working principle. Optical fiber sensor shares the same technology platform as fiber optic communications. In telecommunication areas, a whole industry has enabled by the simple fact that fibers can carry more bandwidth along a long distance and at the same time, with cost that may be very small, where no other communication could compete. For optical fiber sensing, competing with other conventional methods, optical fiber sensors share a series of characteristics, including the compact size, light weight. Additionally, fiber-optic sensors offer the prospect that they can be multiplexed effectively on a single fiber network. Considering optical signal transmitted inside optical fiber, the nature of immunity to electromagnetic interference (EMI), chemical resistance of optical fiber provided another advantage of the application in harsh conditions compared with conventional sensors. Most parameters of interest in industry, commerce and the domestic environment can be adequately measured using dozens or more entirely different approaches [8], [20]–[24].

Optical fiber sensor can be categorized as intrinsic and extrinsic devices [14], [16], [25]–[31]. When talking about intrinsic devices, the interaction occurs within an element of the optical fiber sensors itself. Extrinsic devices are the optical fibers that are applied to couple light, to or from the region where light beam will be influenced by the measurand. Although the region may be external to the optical fiber, the region may be attached to optical fiber in some suitable way, by different manufacturing techniques. Over the last several decades, optical fiber sensor fabrication techniques are evolving, from the early micro-assembly technique to the laser assisted fabrication techniques [10], [11], [16], [28], [32]–[34].

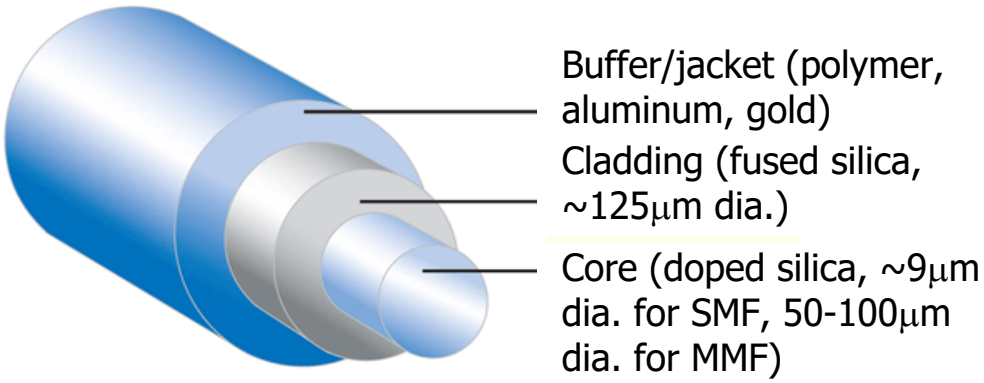

Figure 1.1 Schematic of the commercial optical fiber (which consists of fiber core, fiber cladding and the outside buffer protection layer)

1.3 Fabrication techniques for fiber optic sensors

Optical fiber sensors have been envisioned as a cost-effective candidate for a lot of applications. Over the several decades, a steady growth of optical fibers has been proposed

and applied in different applications. Advantages of optical fiber sensors including immunity to EMI, chemical resistance, high temperature operating point have been proven over the decades of applications. And optical fiber sensors are continuing to involve as the technology advances.

At the early stage, micro-assembly technique has been applied for fiber-optic sensor fabrication [10]. Generally, the fabrication process is complicated and time consuming. From the material perspective, typically different materials will be applied during fabrication process, for example, glues or adhesives will be applied for bonding different parts. Coefficient of Thermo-efficient (CTE) mismatch between different materials will lead to decreased robustness and unguaranteed performance under harsh conditions [8], [10], [24], [27], [35]. Taking all of these into consideration, micro-assembly technique may not be the optimal solution to fabricate sensors for high temperature harsh condition sensing.

As the technology advances, two assembly-free technique have been developed and popular for device fabrication, including the micro-electromechanical system (MEMS) and laser micromachining technique. Devices fabricated by both processes show the unique advantages of improved robustness (without CTE mismatch), dependable performance and dependable performance (which are guaranteed by the design). In addition, the fabrication processes are fast in time and low in cost. These advantages make the two fabrication processes promising approaches for harsh condition sensor fabrications. And laser processing has been widely applied for optical fiber sensors fabrication [11], [33], [36]–[38].

Owing the unique features of high dimensional fabrication accuracy, 3D fabrication capability, femtosecond (fs) laser micromachining has become a powerful tool for optical-fiber sensor/device fabrication. In addition, multi-material (including metal, silica, polymer and sapphire) processing capability enlarges its working flexibility. Over the years, various robust sensors have been fabricated around the world [11], [39]–[43].

In general, MEMS and laser micro-machining processes are material removal-based fabrication process, which show better dimensional accuracy and control. Although robust optical fiber sensors have been fabricated utilizing the assembly-free fabrication process and showed the capability of operating under extreme conditions, considering the fragile nature of optical fiber, during installation process, the sensors may be broken or even their performance may be degraded. In general, the lack of effective methods to package and install sensors into harsh conditions is still a challenging issue[44].

Compared with the top-down subtractive manufacturing process, additive manufacturing, also known as 3D printing process, is a material addition-based fabrication process and a bottom-up fabrication process. It offers better flexibility from both material and structure perspective [44]–[50]. And it offers possibilities for fabricating devices and parts that are not even existing in nature.

It is predicted that additive manufacturing will lead to the third industrial revolution [51]–[53]. With its unique advantages such as rapid prototyping, much less waste, freedom in geometry and material design, shortening the design cycle and near-net-shaped fabrication, some additive manufacturing technologies have been developed for productions [44], [46], [48], [54]. The polymer 3D printers based on stereolithography

(SLA) and fused deposition modeling (FDM) have been commercialized as the desktop printers [55]. One of the typical applications is that people use these printers to print glasses frames. In this way, the design of the frames can be completely customized for every individual.

Recently, additive manufacturing of ceramics and glass have been introduced. Several technologies such as selective laser sintering/melting (SLS/SLM), SLA, direct ink-jet writing (DIW) and Free-forming extrusion (FFE) have been developed for printing ceramic and glass prototypes with unusual geometry and composition [44], [46], [47], [49], [50], [54], which are difficult to obtain by the conventional methods. Furthermore, the additive manufacturing also finds its potential in bio-medical engineering, initiating the so-called "bio-printing" [47,51,52,53].

At the same time, 3D printing has also been widely applied for sensor fabrications over the past years [48], [55], [57], [58]. Generally, 3D printed parts serve as a sensor or part of sensor, and a mechanical supporting platform. With various 3D printing technique and 3D printing materials, a large number of sensors with different sensing mechanism and material composition have been fabricated for different application uses [48], [55], [57]–[59]. Although 3D printed devices with high temperature resistance and sensing performance have not been fabricated yet, the rapid development of 3D printing technique highlights the potential for device/parts fabrication.

More importantly, 3D printed structures can be integrated with 3D printed sensors to form an integrated smart part, thus broadening their application areas[44], [50]. Meanwhile, with the success of micromachining for compact sensor fabrication, additive

manufacturing and subtractive manufacturing could be integrated and realize information integrated manufacturing process, as shown in Fig. 1.2.

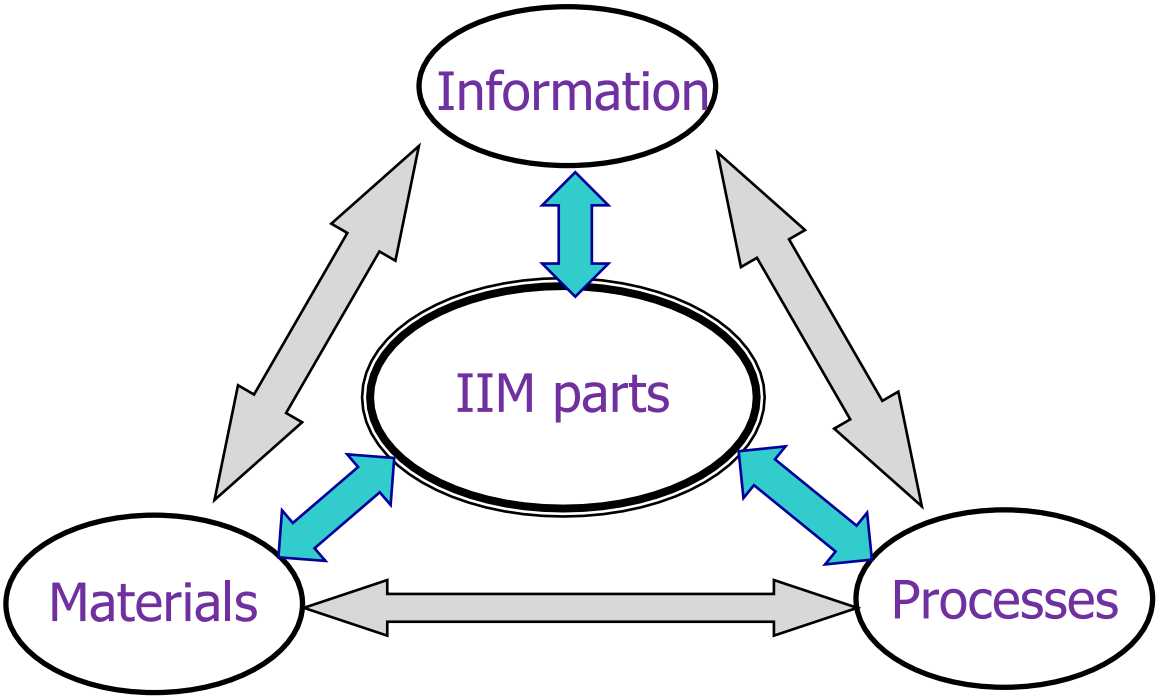

Figure 1.2 Schematic of information integrated manufacturing process

1.4 Motivations and objectives

Motivations: This research was initially motivated by developing novel and advanced fiber-optic sensors/devices based on advanced additive and subtractive manufacturing method that are robust, with high chemical stability and capable to working in extreme environments of advanced energy systems.

Although fiber-optic sensors have shown the capability for harsh condition monitoring, it is observed that the implementation is difficult due to the fragile nature of

optical fiber, and the difficulty of mounting and integrating optical fibers into harsh environments like turbines, downhole or specific microfluidic systems. Compared with the conventional sensor integrating method, which is realized by attaching or mounting sensors on structures after being fabricated, additive manufacturing approach in sensor development has been initiated recently by directly embedding and integrating sensors into functional parts or smart structures to realize in situ measurement of parameters of interests.

Sharing the same material properties (e.g., CTE) as optical fiber, fused silica is the natural choice of material for fabricating optical fiber sensor embedded structures. Recently, glass 3D printing utilizing CO_2 laser direct melting method has been demonstrated. It offers great flexibility and simplicity to produce desired 3D structures with no post-treatment and high temperature resistance, which fastens the additive manufacturing of glass process. By combining the advantages of additive and subtractive manufacturing technique, integrated additive and subtractive manufacturing for harsh condition glass photonic sensor fabrication processes are researched and developed, offering a new way to fabricate optical fiber sensors/structures with enhanced robustness and reliability.

Objectives: From the previous reviews, it is concluded that optical fiber is a promising candidate for harsh environment and chemical/biological sensing applications. Although various optical fiber sensors have been fabricated by assembly-based and assembly-free micromachining method, the application of optical fiber into harsh conditions are still challenging due to the fragile nature of optical fiber. Also, in specific

microfluidic systems, where organic solvents or acids will flow through, PDMS systems will not be capable.

Following are the specific objectives of this work:

(1) Utilize the integrated additive and subtractive manufacturing method, including the materials additive techniques, laser machining, laser heating and laser deposition, to fabricate advanced glass photonic sensors and structures with specific geometry, microstructures and functions.

(2) Develop a diaphragm-based fiber-optic Fabry-Perot interferometric pressure sensor. The pressure sensor is made of all fused silica material, and its fiber housing structure is fabricated by direct three-dimensional (3D) printing of glass on top of a fused silica substrate, which also serves as the pressure sensing diaphragm. A cleaved single-mode fiber (SMF) fixed inside a glass tube is inserted into the fiber housing structure and brought in close proximity to the diaphragm, to form the FPI. Theoretical analysis and experimental verification of the pressure sensing capability are presented.

(3) Develop microfluidic sensors with controlled sensitivity to the parameters of interest (temperature and pressure). Specifically, a novel fused silica microfluidic device with pressure sensing capability is fabricated by integrated additive and subtractive manufacturing (IASM) method. The sensor consists of a capillary and a 3D printed glass reservoir, where the reservoir volume change under pressure manifests liquid level deviation inside the capillary, thus realizing the conversion between small pressure change into large liquid level variation. Thanks to the design flexibility of this unique IASM method, the proposed microfluidic device is fabricated with liquid-in-

glass thermometer configuration, where the reservoir is sealed following a novel 3D printing assisted glass bonding process. And liquid level is interrogated by a fiber-optic sensor based on multimode interference (MMI) effect. This proposed microfluidic device is attractive for chemical and biomedical sensing because it is flexible in design, and maintains good chemical and mechanical stability, and adjustable sensitivity and range.

(4) Develop a 3D printed fused silica glass manufacturing process that is applied to embed fiber-optic sensors for information integrated module fabrication. Thanks to the design flexibility of additive manufacturing process and the fabrication accuracy of subtractive manufacturing process, IASM of fused silica has been applied for in-situ embedding optical fiber sensors, providing a potential solution to solve the deficiency in sensor packaging and installation techniques in harsh condition applications.

1.5 Organizations of the dissertation

This dissertation is organized into six chapters.

(1) Chapter 1 gives a general introduction on the importance of harsh condition sensing and current status of sensors for harsh condition monitoring. Optical fiber sensor fabrication processes are reviewed. After reviewing their history, basic mechanism, and current status, the motivation and objectives of this work is discussed.

(2) Chapter 2 introduces the integrated additive and subtractive manufacturing system that is utilized for optical fiber sensor/device fabrication. The system is comprised of three sub-systems: a CO_2 laser heating system, a picosecond (ps) laser microfabrication

system and a free-forming extrusion system. In this chapter, the three sub-systems will be described, and their functions will be introduced. In addition, the integrated additive and subtractive manufacturing system will be discussed.

(3) In Chapter 3, optical fiber sensors fabricated by additive manufacturing process are introduced, including the printing of all-glass high-pressure optical fiber sensor for high temperature applications and bi-material strip-based temperature sensor with high sensitivity. In this chapter, fiber-optic sensors have been demonstrated and fabricated by the unique integrated additive and subtractive manufacturing system. The process flow and processing parameters during IASM process are presented, which are optimized based on the sensor design and requirements. The sensor responses are characterized to demonstrate the unique features and capabilities of this IASM system on sensor fabrications for harsh condition sensing applications.

(4) Chapter 4 presents three advanced optical sensors with high chemical resistance for microfluidic applications. Two microfluidic devices have been developed for different sensing applications. By utilizing fluidic' s different properties, e.g., fluidity of the liquid and refractive index of the liquid, the sensitivity of the fabricated sensors to the related parameters have been increased. Compared with the previously introduced all-glass sensors, fluidic devices will be another candidate for sensing applications and possess high sensitivities.

(5) Chapter 5 presents the 3D printed fused silica glass process to integrate optical fiber sensors for information integrated module fabrication. Thanks to the design flexibility of additive manufacturing process and the fabrication accuracy of subtractive

manufacturing process, IASM of fused silica has been applied for in-situ embedding optical fiber sensors, providing a potential solution to solve the deficiency in sensor packaging and installation techniques in harsh condition applications.

(6) Chapter 6 summarizes this dissertation.

1.6 Innovations and contributions

The innovations and contributions of this dissertation are summarized as follow:

(1) Based on the unique, home-made and innovative integrated additive and subtractive manufacturing system, sensor and device fabrication process flows have been researched and developed. The system enables additive manufacturing for 3D printing and precise materials deposition at a specific location. For in-situ heating process, the system allows in-situ material processing. In addition, the system is capable of high-resolution laser machining. In this way, the additive and subtractive tools have been integrated into one system and applied for information integrated manufacturing process and information integrated device and sensor fabrication.

(2) An all-glass fiber-optic pressure sensor was fabricated by the three-dimensional printing based on direct laser melting method. The pressure sensor was made of all fused silica material, and its fiber housing structure was fabricated by direct three-dimensional (3D) printing of glass on top of a fused silica substrate, which also served as the pressure sensing diaphragm. A cleaved single-mode fiber (SMF) fixed inside a glass tube was inserted into the fiber housing structure and brought in close proximity to the diaphragm, to form the FPI. And CO_2 laser irradiation was applied in thermal

bonding process. Based on this 3D printing of glass method, the diaphragm thickness and diameter can be designed to adjust the sensitivity and measurement range. Besides, the sensor can work in high temperature environments. It is believed that this all-glass fiber-optic pressure sensor is potentially useful for pressure measurement in high temperature harsh environments.

(3) We propose an innovative method for fabricating glass and ceramic bi-layer structures, with the help of integrated laser machining method. Glass walls of different geometries can be fabricated using the extrusion-based 3D printing method. After each extrusion layer, CO_2 laser heat treatment will be processed for fused silica paste quick melting and fusing both in the printing layer and between the adjacent layers. After 3D printing of glass, ceramic layer is screen printed on side of the glass wall. And ceramic pattern can be flexibly designed and fabricated with picosecond laser ablation followed by CO_2 laser melting to satisfy different application requirements. To demonstrate the stability and functionality of the bi-layer ceramic and glass structure, a straight wall bi-layer strip was assembled together with an optical fiber to form a Fabry-Perot interferometer. And the FPI was demonstrated for high temperature measurement.

(4) By utilizing fluidic' s different properties, e.g., refractive index of the liquid and fluidity of liquid, the sensitivity of the fabricated sensors to the related parameters have been increased. Compared with the previously introduced all-glass sensors, fluidic devices will be another candidate for sensing applications and possess high sensitivities. Specifically, a microfiber half coupler was investigated for RI sensing. The probe was made by cleaving a fused fiber directional coupler at the center of its taper region.

When used for RI sensing, the reflection spectrum blue-shifted as the surrounding RI increased.

(5) A novel fused silica microfluidic device with pressure sensing capability that is fabricated by integrated additive and subtractive manufacturing (IASM) method. The sensor consists of a capillary and a 3D printed glass reservoir, where the reservoir volume change under pressure manifests liquid level deviation inside the capillary, thus realizing the conversion between small pressure change into large liquid level variation. Thanks to the design flexibility of this unique IASM method, the proposed microfluidic device is fabricated with liquid-in-glass thermometer configuration, where the reservoir is sealed following a novel 3D printing assisted glass bonding process. Liquid level is interrogated by a fiber-optic sensor based on multimode interference (MMI) effect.

(6) An information integrated structure with an embedded IFPI sensor was fabricated by the novel Integrated Additive and Subtractive Manufacturing (IASM) method. Glass 3D printing assisted by CO_2 laser direct melting process was applied for flexible 3D structure fabrication. An integrated picosecond laser micromachining system was used for sensor embedded microchannel fabrication with high dimension accuracy. IFPI sensor was embedded in the glass module during fabrication process for in situ temperature monitoring. SEM images and repeatable high temperature responses indicate the bonding between the printed glass and optical fiber, and the feasibility of sensor embedment utilizing IASM method. The proposed information integrated glass module shows the enhanced mechanical robustness, good high temperature response,

long term survivability at high temperature and is miniature in size, all of which make it attractive for high temperature harsh environment applications.

CHAPTER TWO

Integrated Additive and Subtractive Manufacturing System for Photonic Sensor Fabrication

For the work described in this thesis, an integrated additive and subtractive manufacturing system was utilized. The system is comprised of three sub-systems: a CO_2 laser heating system, a picosecond (ps) laser microfabrication system and a free-forming extrusion system. In this chapter, the three sub-systems will be described, and their functions will be introduced. In addition, the integrated additive and subtractive manufacturing system will be discussed.

2.1 CO_2 laser heating

The schematic of the CO_2 laser heating system is shown in Fig. 2.1. A high-power CO_2 laser (Firestar ti100, SYNRAD Inc.) with wavelength of 10.6 μm is applied to realize

Table 2.1. CO_2 laser specifications.

Model No.	Firestar ti100
Wavelength	10.6 μm
Average Max. Power	100 W
Mode Quality	TEM_{00}, $M^2 < 1.2$
Beam Diameter	2.0 mm ± 0.3 mm
Beam Divergence	< 7.0 mrad

the heating process onto materials. The key specifications of this CO_2 laser are summarized in Table 2.1.

As shown in Fig. 2.1, to move the laser beam during laser heating process, the laser scanning is controlled by a three-axial motorized translation stage (IMS-V series, Newport Inc.). A ZnSe lens with a focal length of ~50 mm was used to focus the CO_2 laser beam into a spot size (D) of ~220 μm. During heating process, CO_2 laser beam interacts with the material and the computer-controlled translation stage moves the material in the predesignated toolpath. The focal point can be controlled flexibly by adjusting the z-axis distance between focal lens and material surface. In addition, the scanning speed of the stage can be tuned accordingly.

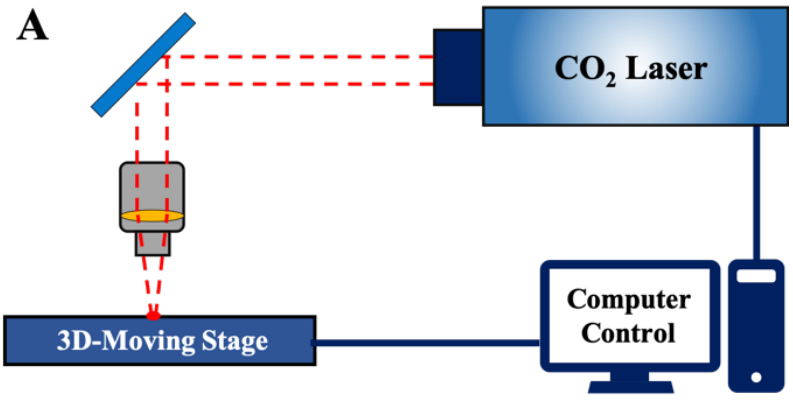

Figure 2.1. Schematics of the CO2 laser heating systems: Laser scanning is controlled by the 3D moving stages.

2.2 Picosecond laser microfabrication

Fig. 2.2 shows the schematic of picosecond laser microfabrication system. One Nd: YAG picosecond laser (APL-4000-1064, Attodyne Inc.) is applied for laser-material interaction. The specifications of the picosecond laser are summarized in Table 2.2. The maximum output power of the ps laser is 4 W. The Gaussian laser beam was guided through a 5X objective lens (NA = 0.13) to obtain a focusing beam with a spot size of ~20 μm and a working distance of ~11 mm. A CCD camera was mounted on top of the objective lens to in-situ monitor the fabrication process. The laser beam is moved by the three-axial translation stage under the computer control in predesignated toolpath with a speed up to 1 m/s.

A Nd: YAG picosecond laser (APL-4000-1064, Attodyne Inc.) was used for high-resolution microfabrication on different materials. The key specifications of the picosecond laser are summarized in Table 2.2.

Laser beam was guided through a 5x objective lens (NA = 0.13) to obtain a focusing beam with a spot size of about 20 μm and a working distance of roughly 11 mm. A dichroic mirror and a charge-coupled device (CCD) camera connected to a computer are involved to in-situ monitor the fabrication process. Front-side and backward illumination methods can be used for different fabrication processes.

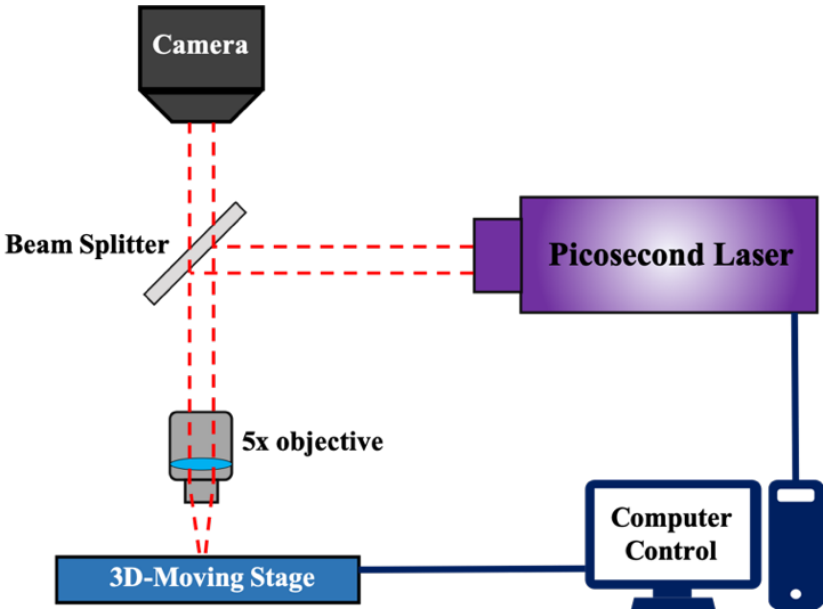

Figure 2.2. Schematic of the picosecond laser microfabrication system.

Table 2.2. Picosecond laser specifications.

Model No.	APL-4000-1064
Wavelength	1064 nm
Average Max. Power	4 W
Pulse Duration	6 ± 2 ps
Max. Pulse Energy	150 μJ @ 10 kHz
Repetition Rate	0.152 Hz – 1 MHz
Mode Quality	TEM_{00}, $M^2 < 1.3$
Beam Diameter	0.5 mm ± 0.3 mm
Beam Divergence	< 3.0 mrad

2.3 Material extrusion system

Figure 2.3 schematically shows the material extrusion system. A micro-extruder (eco-PEN300, Preeflow by ViscoTec Inc.) was used to deposit the materials at the desired locations. Table 2.3 presents the specifications of the micro-dispenser. This micro-extruder can cover a wide range of materials with a viscosity ranging from zero to over 1000 Pa·s, as shown in Fig.2.4. 3D printing is realized by programming the stage to draw the 3D model while the micro-extruder keeps extruding materials.

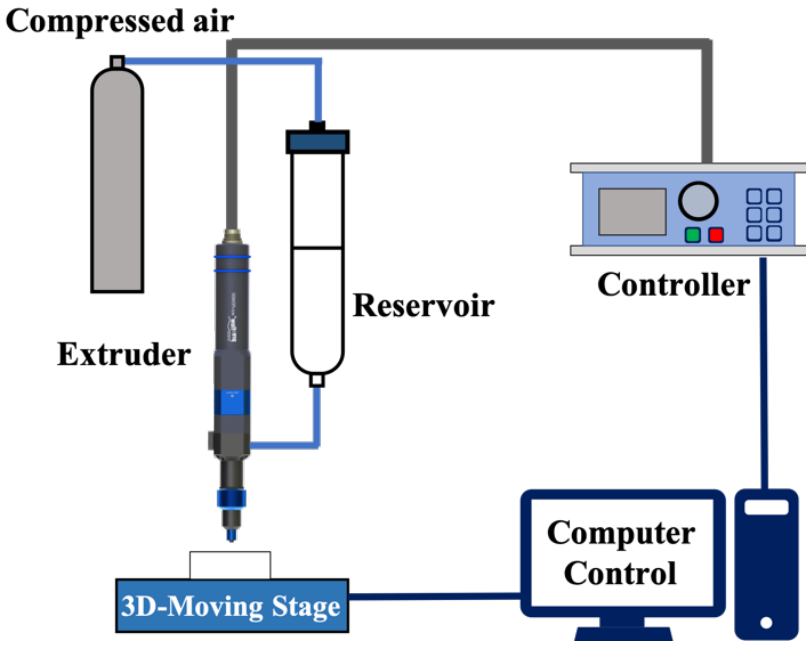

Figure 2.3. Schematic of the free-forming extrusion system.

Table 2.3. Extruder specifications.

Model No.	eco-PEN 300
Min. Dosing Quantity	1 µL
Dosing accuracy	1±%
Flow Rate	0.12 – 1.48 µL/min

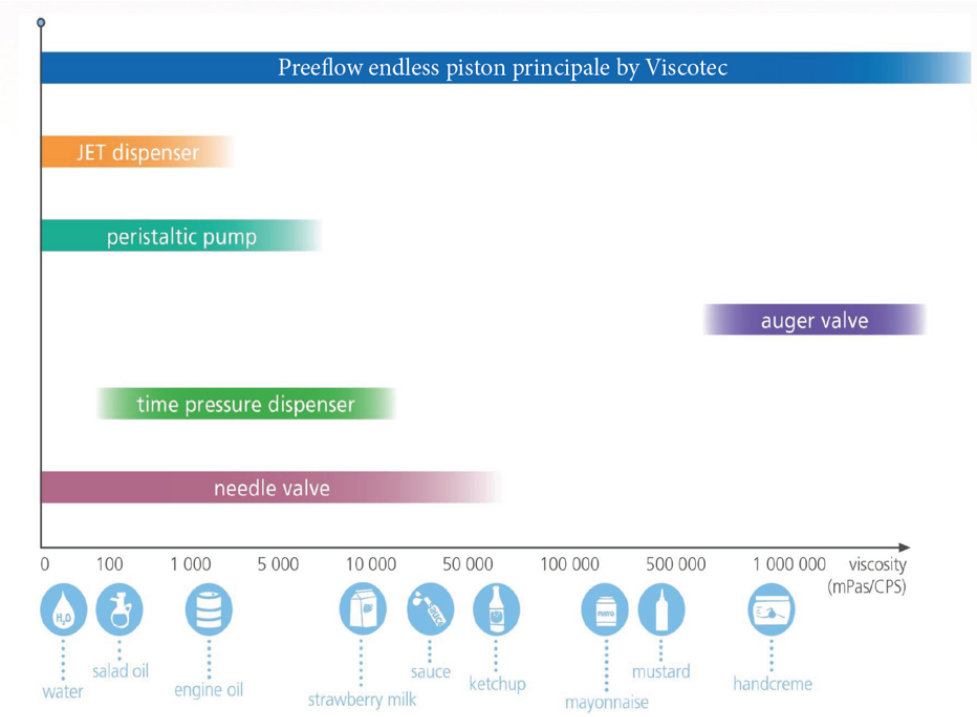

Figure 2.4. The viscosity range of the materials for the eco-PEN 300.

2.4 Integration of the sub-systems for manufacturing

To integrate the sub-systems for manufacturing, a control center was used to control and coordinate all the hardware. Fig. 2.5 shows the configuration of the integrated system. The controllers of the three-dimensional translation stage, lasers and material extruders are connected to the control center and controlled by the Direct Machining Control software (DMC, Newport Inc.). In addition to move of the three-dimensional translation stage, the ACS controller also provides ten digital output (DOut) ports for external trigger control. When the lasers or extruder connect to these DOut ports, the ACS controller can send out a 5V gate signal to trigger the on/off status of the lasers or extruder. In the DMC software, this trigger signal can be programmed to send out at the start/stop position of the toolpath.

In this way, the on/off of the devices is automatically synchronized with the toolpath during manufacturing.

As shown in Fig. 2.6, the integrated additive and subtractive manufacturing (IASM) system was developed, which is a sophisticated platform that combines three sub-systems. The system has a X-Y stage with a travel distance of 500 mm and position accuracy of 1 μm, and a Z stage with a travel distance of 300 mm and position accuracy of 0.1 μm. It has two optical beam scanners that can deliver the laser beams to the parts under manufacturing, an integrated microscopic imaging system that allows in situ observation of the fabrication process, and an interactive software platform that allows importing the part from the CAD model and optimizing the tool-path for fully-automated fabrication by selecting the various tools.

The IASM system/method has a number of unique advantages that make it attractive for additively manufacture sensor-embedded smart components/sensors for harsh environment applications.

1). High dimension accuracy for sensors and devices. Glass 3D printing with direct laser melting process in this IASM system presents the dimension accuracy on the order of tens or hundreds of microns. The addition of laser micromachining allows the fabrication of structures with micron dimension accuracy, showing the unique advantage of IASM system in high dimensional accuracy compared with traditional 3D printing process.

2). User friendly interface. The IASM system can directly take a CAD model and optimize the process for automated fabrication. It also allows the user to interactively

control the fabrication process for embedding sensors and other functional components into the parts being manufactured.

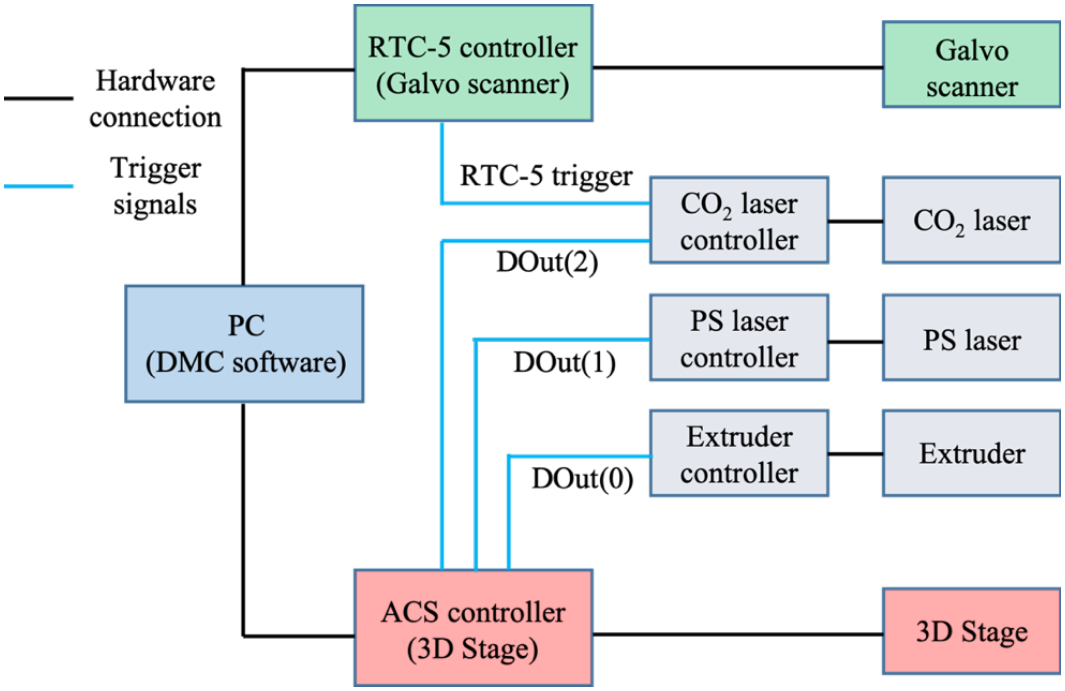

Figure 2.5. Configuration of the integrated laser 3D manufacturing system.

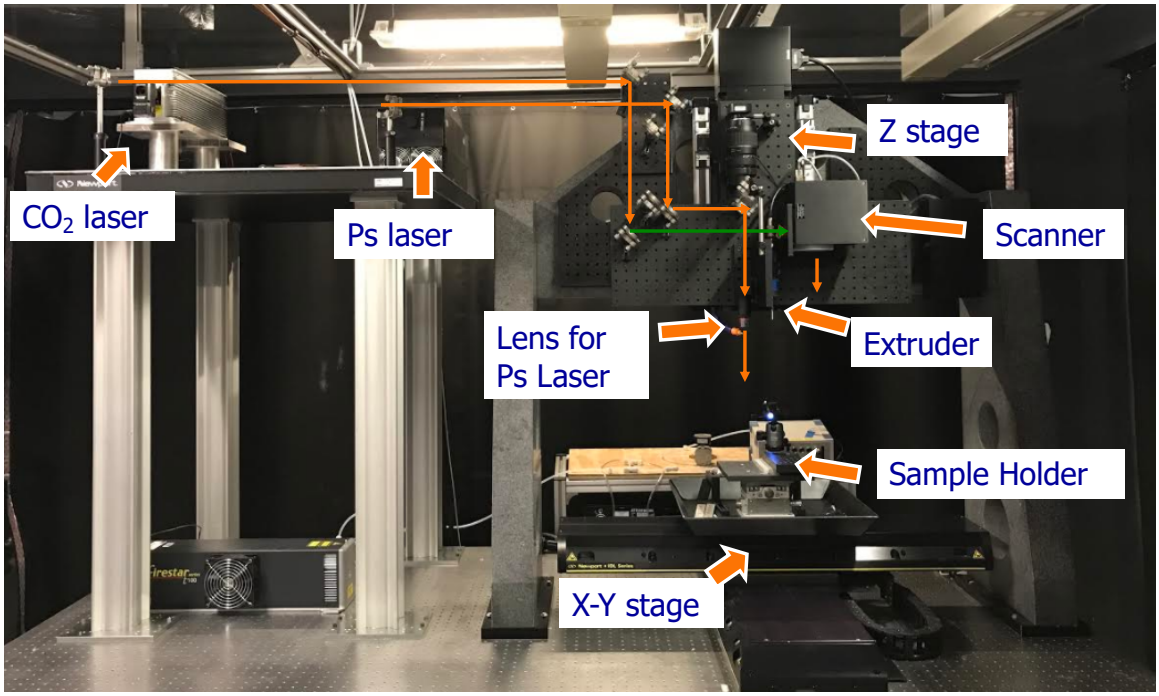

Figure 2.6 Picture and function blocks of the integrated additive and subtractive manufacturing (IASM) system. This platform integrates a number of advanced manufacturing tools into one single system, including freeze form extrusion, inkjet printing, laser sintering, laser micromachining and an interactive interface to import from CAD models.

2.5 3D printing of transparent fused silica glass

The process flow for laser 3D printing of fused silica glass were shown in Fig. 2.7. The CAD model of the printed object will be generated in SolidWorks and loaded into the control software system. CAD model will be then sliced into a bunch of 2D-patterned layers with designated thickness (Fig. 2.7A).

In each sliced layer, two processes will be applied to realize the 3D printing process in this layer. First, micro-dispenser (eco-PEN300, Preeflow by ViscoTec) will be applied to deposit the fused silica paste with designed patterns. After the deposition of each layer, after optimized time delay, a high-power CO_2 laser (Firestar ti100, SYNRAD Inc.) will assist to melt the paste. Thanks to the high-power laser irradiation, fused silica pastes will be melted and the bonding both between the particles in this layer and between the adjacent layers will also be melted (Fig. 2.7B)[54], [60], [61].

By repeating these two processes from layer to layer, the fused silica structure with designed 3D pattern will be directly printed, as shown in Fig. 2.7C. And no post-treatment is needed. by optimizing the laser operating parameters such as the laser output power,

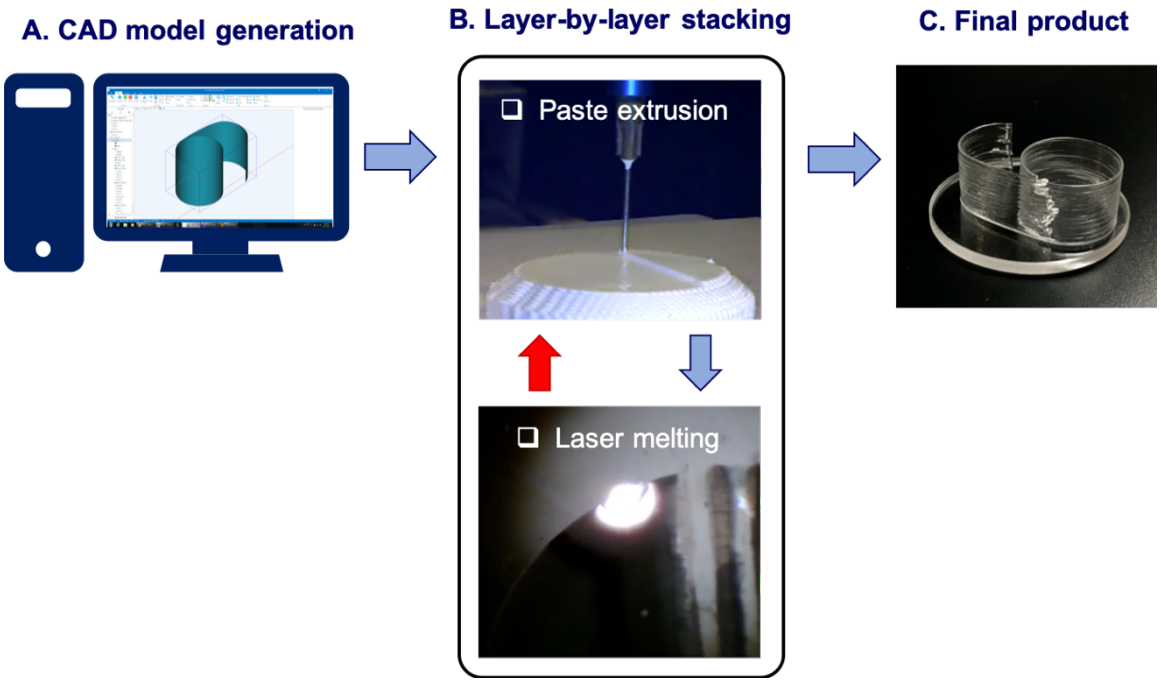

Figure 2.7 Schematic of the process flow of laser 3D printing fused silica glass.

scanning speed and spot size, the porosity of the 3D printed glass could be flexibly tuned[54].

The transparency of the laser-melted fused silica glass can be improved by tuning the laser operating parameters. As shown in Fig. 2.8, the transparency of the laser-melted fused silica can be controlled by tuning the laser output power while other parameters were fixed. Observed from the cross-section SEM images of the samples, the increase of the laser output power reduced the porosity of the laser-melted materials, resulting in the improvement of the transparency. In this way, laser shows its unique capability to flexibly modify the materials properties during the manufacturing process.

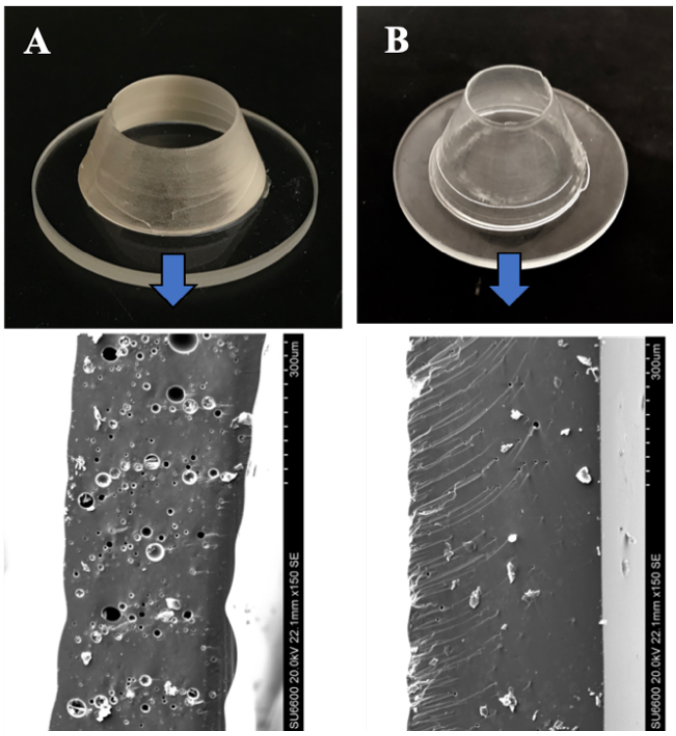

Figure 2.8 Pictures of the 3D printed fused silica glass and its related SEM images of the cross-section view of the thin wall melted by different laser power (A) 12.5 W, (B) 15 W (Scanning speed: 1 mm/s, Spot size: ~2 mm).

The optical transmission of the 3D-printed glass in wavelength range of 200-2000 nm was evaluated. As shown in Fig. 2.9 (B), transmission spectrum of polished printed glass was applied for transmission spectra test. In addition, two other fused silica substrates with purity of 99.9% and Corning 7980 were measured with the same instrument for comparison. As shown in Fig. 2.9, the optical transmission of printed glass reaches 90% beyond the wavelength range of ~650 nm, reaching similar performance with the two commercial substrates. Additionally, in the region of 200 - 650 nm, the transmission of the 3D-printed glass decreases dramatically, showing a huge difference from the two commercial products. The optical loss in the UV to visible region could be probably related to micro-pores in the 3D-printed glass as shown in the inset A of Fig. 2.9, which may scatter light at this wavelength range. Nevertheless, the 3D-printed glass shows comparable optical transmission to commercial fused silica glass products, especially in the red-IR region, indicating that the 3D-printed fused silica glass is suitable for various optical applications (e.g., optical telecommunication applications).

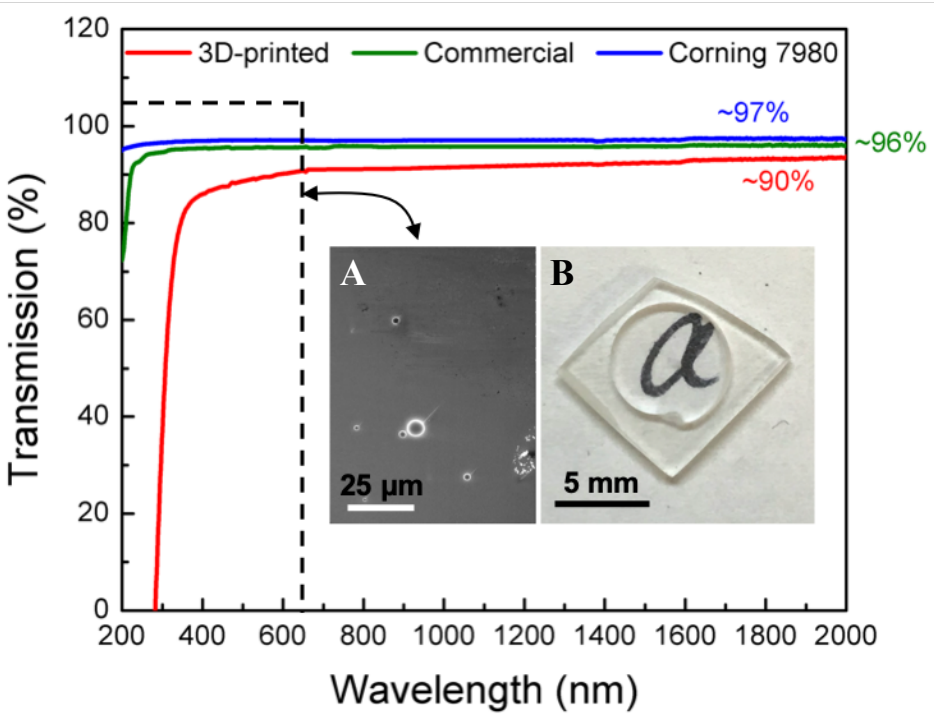

Figure 2.9 Optical transmission spectra between 200 nm and 2000 nm of the 3D-printed fused silica glass (red), the commercial fused silica substrate with silica content of 99.9% (green), and the Corning 7980 fused silica glass, respectively. Inset: (A) Cross section SEM image of the 3D-printed fused silica substrate; (B) Picture of the 3D-printed fused silica glass substrate

CHAPTER THREE

Three-dimensional Printing of High Temperature Fiber-Optic Sensors

In this chapter, fiber-optic sensors have been demonstrated and fabricated by the unique integrated additive and subtractive manufacturing system. The process flow and processing parameters during IASM process are presented, which are optimized based on the sensor design and requirements. The sensor responses are characterized to demonstrate the unique features and capabilities of this IASM system on sensor fabrications for harsh condition sensing applications.

3.1 Three-dimensional printing of all-glass high-temperature fiber-optic pressure sensor

In this paper, we report a diaphragm-based fiber-optic Fabry-Perot interferometric pressure sensor. The pressure sensor is made of all fused silica material, and its fiber housing structure is fabricated by direct three-dimensional (3D) printing of glass on top of a fused silica substrate, which also serves as the pressure sensing diaphragm. A cleaved single-mode fiber (SMF) fixed inside a glass tube is inserted into the fiber housing structure and brought in close proximity to the diaphragm, to form the FPI. Theoretical analysis and experimental verification of the pressure sensing capability are presented.

3.1.1 Harsh condition pressure sensing introduction

Pressure monitoring is of great interests in various important applications where pressure of the environment usually provides real time information to understand and

control the processes [7], [62], such as oil and gas pipelines pressure metering [63], turbines [64] and downhole pressure monitoring [65]. Pressure monitoring in many cases is under harsh environments, like, high temperature, time-varying aqueous environments. As such, it is desirable in harsh environments for pressure sensors to be capable of operating at high temperatures (e.g., 500 ℃) and immune to surrounding environments. Optical fiber sensors have been widely investigated over the last several decades for pressure sensing. Over the years, various optical fiber sensors have been proposed and demonstrated for pressure sensing, such as fiber interferometers [12], [25], [66], fiber Bragg gratings [67], whispering gallery mode optical resonators [34] and micro-bending sensors [68]. Generally, these optical devices have a compact size, high sensitivity, fast response, immunity to electromagnetic interference (EMI), and promising broad applications.

Fiber-optic extrinsic Fabry-Perot interferometer (EFPI) is among the popular choices for pressure monitoring, owing to its advantages of high spatial resolution and independence to polarization changes [12], [66], [69]. A typical EFPI pressure sensor uses a diaphragm as the sensing element. Pressure induced diaphragm's deformation generates the change of interferometer' s optical path difference (OPD). And the change of OPD is monitored by the interferometer with high sensitivity and high resolution. In recent years, both fiber inline EFPI sensors and assembly based EFPI sensors have been reported for pressure monitoring. In general, the sensitivity and pressure range of assembly-based sensors is easy to be adjusted by tuning the dimension of the diaphragm. While at the same time, typically, there exists the mismatch of coefficients of thermal expansion (CTE) between different materials (e.g., glass and bonding materials), resulting in the large

temperature cross-sensitivity and sometimes limitations in working temperatures. Comparatively, Assembly-free fiber inline EFPI sensors have a compact size and improved mechanical robustness, thanks to various micromachining techniques [12], [69], [70]. In our previous work, an all-glass fiber inline EFPI pressure sensor was fabricated by a femtosecond laser [12], which was capable of working at high temperatures up to 700 °C, with small temperature cross-sensitivity. However, the pressure sensitivity was relatively low because of the dimension of the diaphragm. Therefore, there are trade-offs between high pressure sensitivity, low temperature cross-sensitivity, high temperature operating point and mechanical robustness.

Recently, three-dimensional (3D) printing technology has been demonstrated as a powerful approach for the fabrication of sensors [48], [56], [57], [71]. This technique offers great flexibility and simplicity to produce desired 3D structures. Meanwhile, 3D printing process can incorporate with other processes to realize an integrated smart structure. Various 3D-printed sensors have been proposed and demonstrated [56], [57]. In general, 3D printed structures serve as a sensing part or mechanical supporting platform. However, due to the properties of the printing materials, which are typically polymer or metal materials, 3D-printed sensors rarely survive in high temperature environments. Recently, a 3D-printed ceramic part with embedded sapphire optical fiber has been reported for high temperature applications [44]. And a fused silica additive manufacturing method [46], proposed by Kotz et al, was successfully applied to create transparent fused silica components. Components created from both printing processes show high thermal

resistance. However, 3D printed fused silica/ceramic parts with high temperature sensing capabilities have not been reported yet.

Here we present an all-glass EFPI pressure sensor fabricated by Three-dimensional (3D) printing of fused silica technique. In our previous work, we reported the extrusion-based 3D printing of ceramics [50] and glass [54] technique. And in this paper, the extrusion-based 3D printing of transparent glass assisted with CO_2 laser direct melting fabrication process is employed to fabricate sensing structures. The 3D printing of glass technique allows rapid fabrication of a fiber housing and diaphragm integrated part with flexible dimension tuning capability. Optical fiber is brought in close proximity to the diaphragm to form the FPI cavity. And optical fiber is fixed with the help of CO_2 laser irradiation. Simulation and pressure test of the sensor are presented. Meanwhile, the temperature dependence of the all-glass sensor is studied.

3.1.2 Fabrication of pressure sensor

Figure 3.1(a) schematically illustrates the structure of the proposed sensor. The proposed sensor is composed of a fiber housing structure on top of a diaphragm and a single mode fiber (SMF). When the optical fiber is brought in close proximity to the glass diaphragm with gold coating, the Fabry-Perot (FP) cavity is formed between the end-face of optical fiber and glass diaphragm. The low finesse FP device can be modeled using two-beam optical interference equation:

$$I = I_1 + I_2 + 2\sqrt{I_1 I_2}\cos\left(\frac{4\pi n \cdot L}{\lambda} + \varphi_0\right) \quad (3.1)$$

Where I is the intensity of the interference signal, I_1 and I_2 are the reflections at the cavity end-faces, , d is the cavity length, n is the refractive index of the medium filling the

FP cavity, λ is the optical wavelength in vacuum, and φ_0 is the initial phase of the interference.

According the FP cavity equation, if the amplitudes of two reflection beams are the same, the FP interferometer (FPI) will have the largest fringe visibility and dynamic range. In addition, the interference signal reaches its minimum (I_{min}) and destructive interference occurs when the phase term reaches an odd number of π, that is,

$$I = I_{min}, when\ \frac{4\pi n \cdot L}{\lambda} + \varphi_0 = (2m+1)\pi \tag{3.2}$$

Where m is an integer and λ is the center wavelength of the valley. And the optical length of the cavity can be expressed as,

$$L \cdot n = \frac{1}{2}\left(\frac{\lambda_1 \lambda_2}{\lambda_1 - \lambda_2}\right) \tag{3.3}$$

Where λ_1 and λ_2 are the center wavelengths of the two adjacent valleys in the interference spectrum. Eq. (3.3) can be applied to calculate the refractive index (n) of the FP cavity when the length (d) is known/fixed, or the length (L) when the refractive index (n) is known. The nL term is also known as Free Space Range (FSR). When the ambient pressure changes, the diaphragm deforms its shape and, consequently, generates a change in the interference signal that can be correlated with the pressure change.

To fabricate the sensor, 3D printing of glass process is conducted for a fiber housing structure printing [54]. The fiber housing structure consists of a cone shape and a hollow tube structure on its top. First, a cone structure is printed on a thin fused silica substrate (Corning 7980, with a dimension of 10 x 10 x 0.5 mm), which also serves as the pressure sensing diaphragm. During the printing process, the cone structure is printed until the decreasing radius is small enough for a glass tube to be inserted and fixed. Then printing

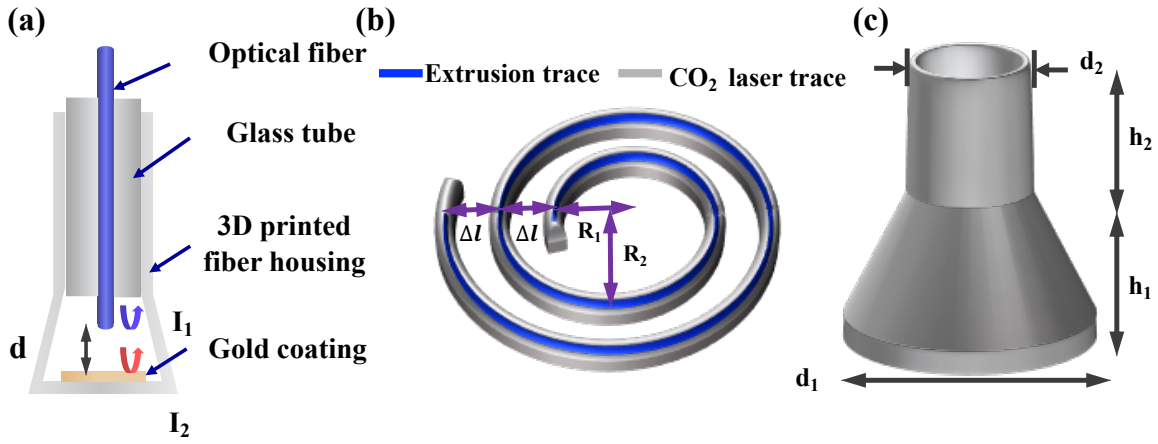

Figure 3.1 (a) Schematic of the pressure sensor. (b) Schematic diagram of the process flow for one single printing layer. Glass paste is extruded following the extrusion trace and then CO_2 laser irradiation going through the CO_2 laser trace will be conducted for melting and fusing the pastes. (c) 3D model for the fiber housing structure.

process continues with the fixed radius to form a tube structure. The cone structure enhances the flexibility for diaphragm dimension tuning, to help realize sensors with adjustable pressure measurement sensitivity and range. And the tube structure makes the perpendicular alignment of glass tube to the diaphragm easy. After the printing of fiber housing structure, gold sputter coating is in process to coat the inner surface of the diaphragm. Then, glass tube is inserted and the gap between tube and fiber housing structure is filled with fused silica paste. And optical fiber is inserted into the glass tube and brought to close proximity to the diaphragm to form the Fabry-Perot cavity. Finally, CO_2 laser irradiation is conducted for tube and optical fiber fixing.

During the 3D printing process, for each printing layer, fused silica paste is extruded at controlled flowrate through an extruder (eco-Pen300, Preeflow) with circular nozzle first. And CO_2 laser irradiation (with a wavelength of 10.6 μm, ti100W, Synrad) is used to heat the paste with optimized output power, spot size and scanning speed. With the help of laser processing, fused silica paste is quickly melted and fused both in the printing layer and between the adjacent layers. Figure 3.1(b) shows the extrusion trace and CO_2 laser irradiation trace. It is noticed that the extrusion trace is in a spiral shape. Considering the extruded paste width, each adjacent trace of the spiral is separated with the same distance to make sure neither paste overlapping nor gaps existing. After 40 seconds time delay, CO_2 laser irradiation follows the same trace as the extrusion trace. In addition, extra path is designed for the irradiation process, as shown in Figure 1(b). With this optimized laser irradiation trace setting, fused silica pastes at the starting and ending point of the spiral will be under the same heating profile from CO_2 laser irradiation as the pastes in middle of the spiral. The next printing layer will be processed 40 seconds after the laser heating process. With this setup for each printing layer, Figure 3.1(c) shows the printing model of fiber housing structure. d_1, d_2 and h_1, h_2 represents the separation between two traces, diameters of bottom and top layer, heights of the hollow cone and tube structures, respectively. And the values were optimized and set to be 0.4 mm, 7.3 mm, 4.2 mm, 1.5 mm and 3 mm respectively.

Figure 3.2(a) shows the printed transparent fused silica fiber housing structure on top of a fused silica substrate. The substrate, which also performed the pressure sensing function, was fused together with the printed glass to form an integrated part, ensuring the

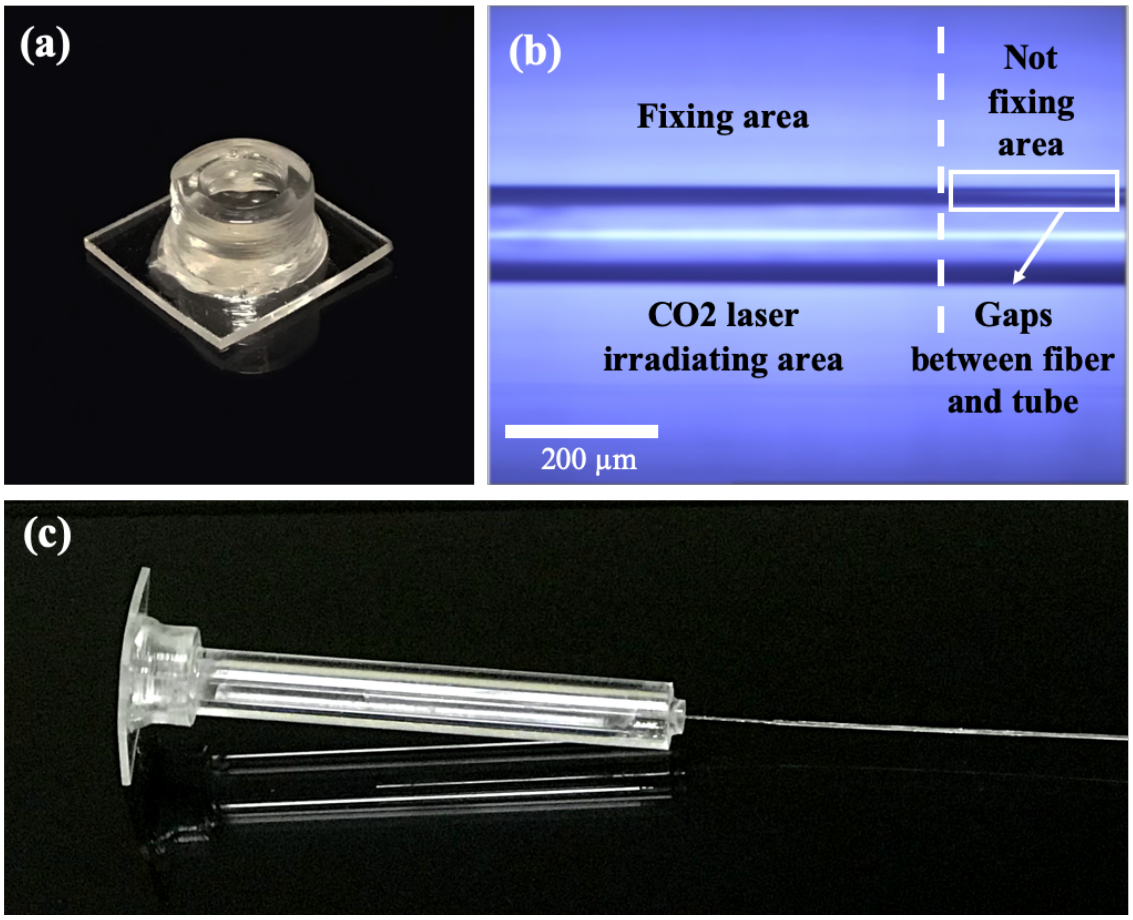

Figure 3.2 (a) photo of the 3D printed fiber housing structure, (b) microscope image showing that optical fiber is fixed inside the tube with the help of CO_2 laser irradiation through cylindrical lens. No gap can be found at the laser irradiation area. (c) Photo of the assembled all-glass pressure sensor.

good mechanical robustness of the structure. Additionally, gold sputter coating (Desk V, Denton) was deposited onto the inner surface of the diaphragm, with the thickness of ~20 nm, to enhance the light reflection as well as the immunity of the sensor to variations in surrounding media. Additionally, a fused silica tube with outer diameter (OD) of 4 mm

Table 3.1. FEM simulation parameter settings

Material	Properties	Value
Commercial Fused silica	Young's modulus	73 GPa at 25°C
	Poisson's ratio	0.17 at 25°C
	Density	2.201 g/cm^3
	Diaphragm diameter	7.3 mm
	Diaphragm thickness	500 μm

was inserted into the printed structure and the gap between them was filled with fused silica paste. Laser irradiation was in progress for paste melting and fusing. Finally, a cleaved single mode fiber (SMF) was inserted into the tube and brought into the designated position to form the FPI. During this process, a monitoring system was used to acquire the spectra, which consisted of an optical spectrum analyzer (AQ6370D, Yokogawa), fiber coupler and broadband light source (Agilent 83437A). Then CO_2 laser irradiation with ZnSe cylindrical lens was processed to deform the tube and eliminate the gap between tube and optical fiber.

The CO_2 laser was set to 30 W and scanned one time with a speed of 2mm/s in a direction perpendicular to the fiber placement. As shown in Figure 3.2(b), no gap existed in the laser irradiation area (left part of Fig. 3.2(b)). And gaps between tube and SMF is clearly shown in the unirradiated area (right part of Fig. 3.2(b)). Figure 3.2(c) shows the assembled all-glass pressure sensor.

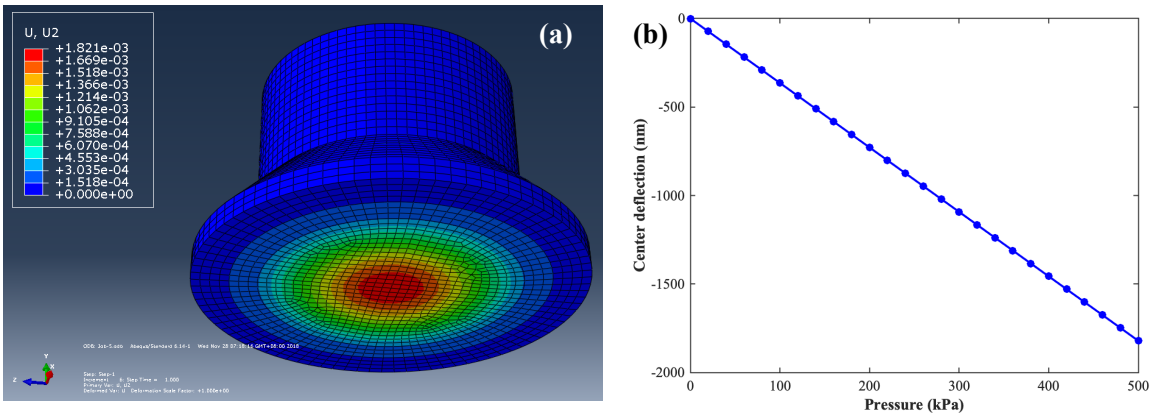

Figure 3.3 (a) Simulation results from Abaqus showing the deflection distribution of the fiber housing structure under external pressure of 0.5 MPa. (b) Center deflection of the diaphragm in response to external pressure change.

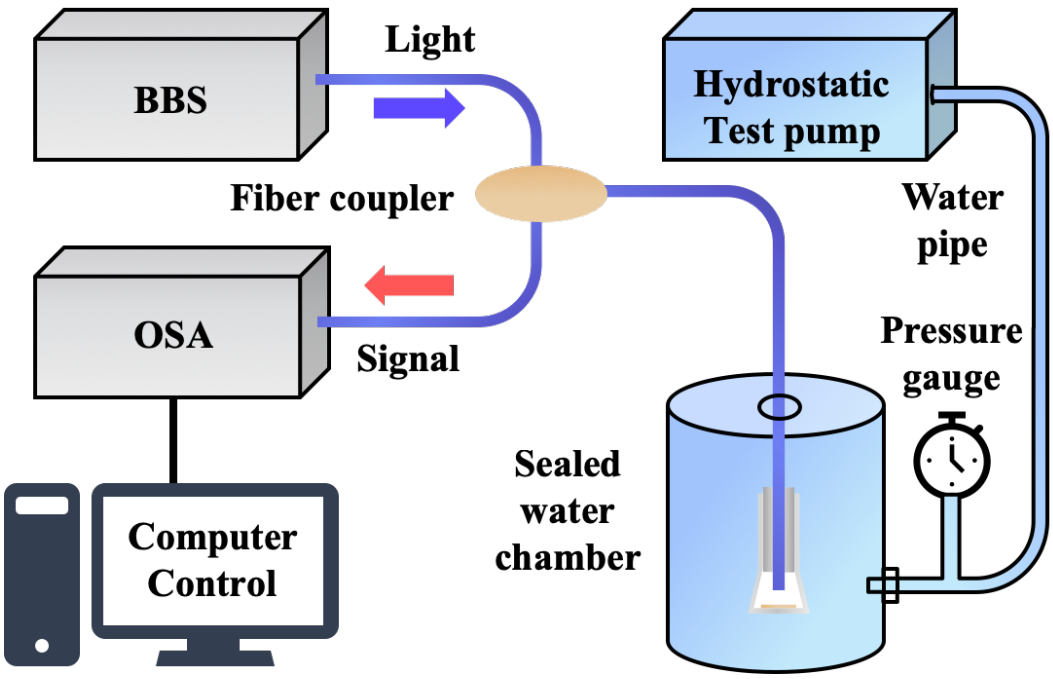

Figure 3.4 Schematic of the experiment setup to test the pressure measurement capability of the all-glass FPI sensor.

When the sensor is exposed to external pressure, deflection of the fiber housing structure can be modeled and analyzed using a finite element method, with the parameters set the same as the parameters shown in Fig. 3.1(c). Figure 3.3(a) shows the deflection distribution of the proposed structure in Abaqus when it is under the external pressure of 0.5 MPa. The majority of the simulated structure is in blue, indicating that no deflection is observed. And the largest deflection (in red) is located at the center of the diaphragm, which is 1.821 μm. Figure 3.3(b) shows the center deflection under pressure change. A linear relationship is observed, and the slope of the fitted line is calculated as the simulated pressure sensitivity, which is estimated as 3.6 nm/kPa.

Through the simulation, only diaphragm is sensitive to external pressure change. As such, the pressure sensitivity for a circular diaphragm can be also described as [12]:

$$S = \frac{3(1-\mu^2)a^4}{16Eh^3}(\mu m/Pa) \tag{4}$$

where a and h are the radius and thickness (in μm) of the diaphragm. E and μ are the Young' s modulus and Poisson' s ratio of the diaphragm. When the diaphragm is exposed to external pressure P, the deflection of the diaphragm is given by:

$$\Delta d = \frac{3(1-\mu^2)a^4}{16Eh^3}P\ (\mu m) \tag{5}$$

3.1.3 Experimental results and discussion

The pressure sensitivity of the fabricated sensor was characterized. As shown in Fig. 3.4, the sensor was sealed in a sealed water chamber, where the hydrostatic pressure was supplied using a hydrostatic test pump and monitored with a commercial pressure gauge (with 0.5% measurement accuracy). The light from a broadband light source was

injected into the sensor through a fiber coupler and reflected interference spectra were detected via the OSA and recorded for every 20 kPa increasement from 0 to 0.5 MPa. Figure 3.5(a) shows the spectra of the sensor when exposed to external pressures of 0 kPa, 200 kPa and 500 kPa, respectively. Figure 3.5(b) plots the FFT of the spectra in Fig. 3.5(a). Three main frequency components with different spatial position are located in Fig. 3.5(b). When pressure increased, the peak position shifted left, meaning that the cavity length decreased, which agreed well with the simulated results. And cavity length change of the sensor as a function of the external pressure was plotted in Fig. 3.6. Under 0.5 MPa pressure change, a cavity length change of 2148.7 nm was observed. The response curve shown in Fig. 3.5 was nonlinear in the large pressure range. As such, a second order polynomial fit was used to correlate the relation between the cavity length change and applied pressure. It is noticed that the linear term coefficient is much larger than the coefficient of second order term. Therefore, the linear term dominated, and the coefficient of the linear term was calculated as the averaged pressure sensitivity, to be 3.18 nm/kPa. Additionally, considering the changing slope in the large pressure test range, the cavity length change in relation to pressure variation was plotted into three separated small pressure ranges, which were 0 to 160 kPa, 180 to 340 kPa and 360 to 500 kPa, respectively, as shown in the insets of Fig. 3.6. A linear fit was applied to the three separated regions and sensitivities were calculated to be 3.52 nm/kPa, 4.30 nm/kPa and 5.22 nm/kPa, with the coefficients of determination (or the R-squared values) of the curve fittings being 0.998, 0.999 and 0.998, respectively. The sensitivity shows the trend of improvement when the sensor was exposed to larger external pressures.

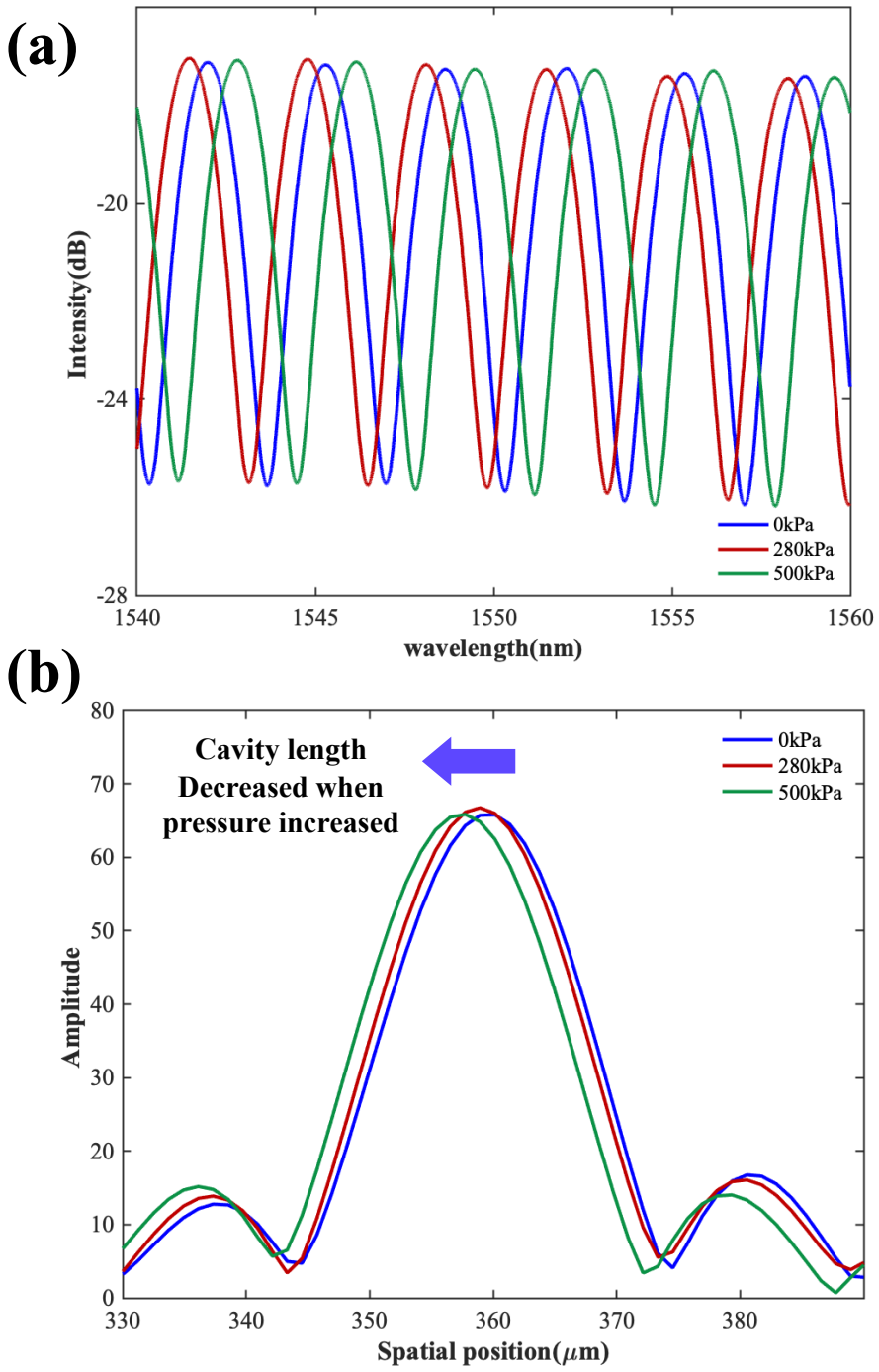

Figure 3.5. (a) Spectra shift in response to external pressure changes. (b) FFT results of the sensor spectra. When external pressure increased, the cavity length decreased.

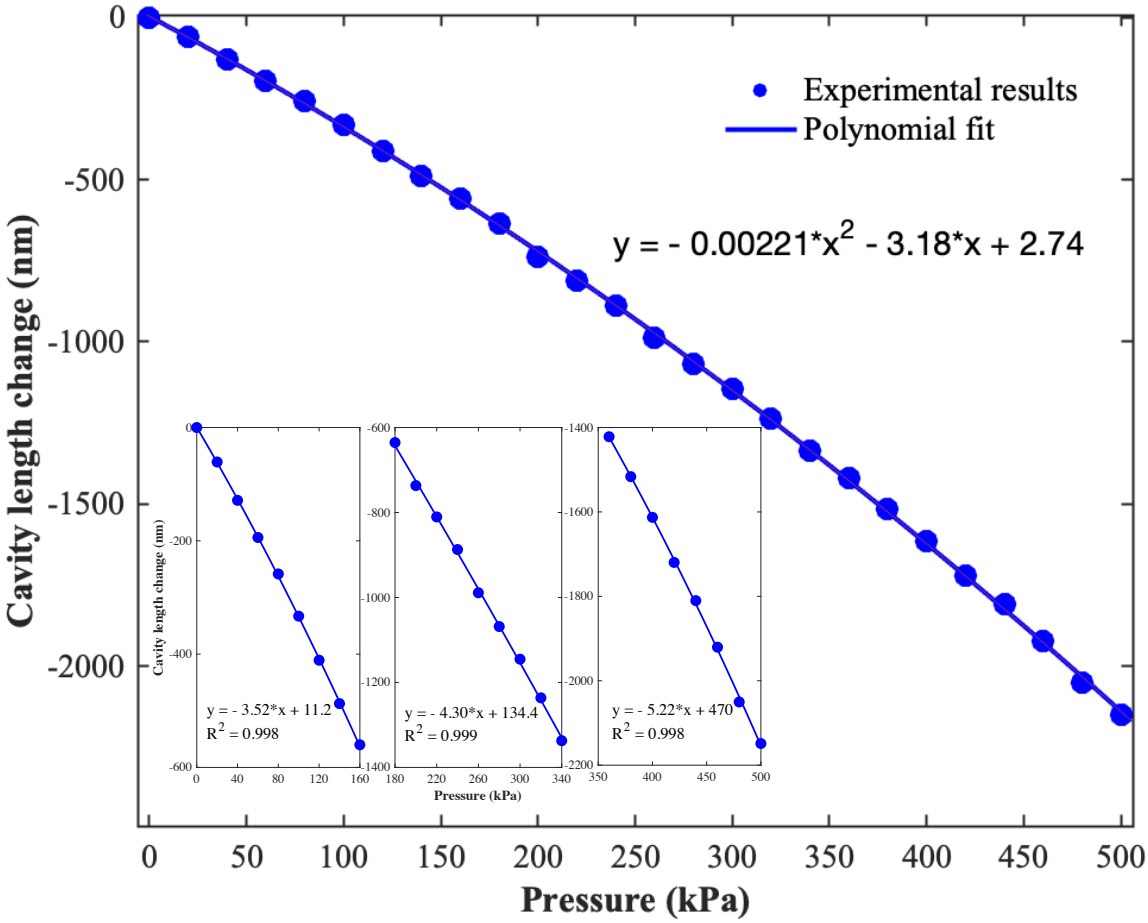

Figure 3.6. Pressure-induced cavity length change of the pressure sensor. Insets: Cavity length change with respect to the pressure change in the range of 0 to 160 kPa, 180-340 kPa and 360 to 500 kPa, respectively.

In addition, the radius of the diaphragm could be calculated from the cavity length change using Eq. (3.5). The calculated diaphragm radius was 3.803 mm, which was close to the proposed radius of 3.65 mm. And the difference between experimental results and simulation results were related to the sensor fabrication process. As shown in Fig. 3.1(b), during the 3D printing process, for each printing layer, due to the spiral-shape extrusion

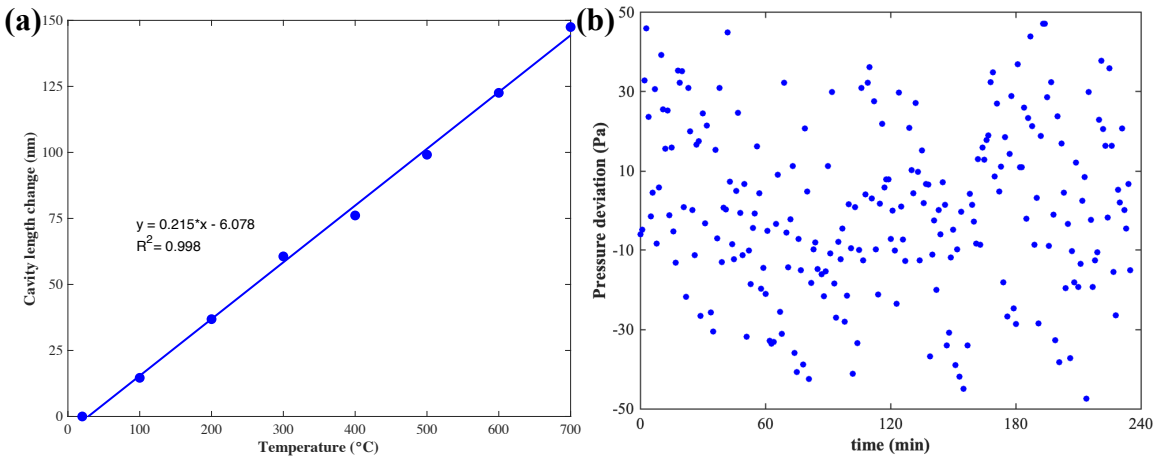

Figure 3.7. (a) Cavity length change with respect to temperature change. (b) Measured pressure deviation in a time period of 240 mins.

process, the area inside the printing trace was not a perfect circle. While in equation calculation and model simulation, the radius applied was the value of R_1 in Fig. 3.1(b). But the size of the printed diaphragm should be in the range of a circle with radius between R_1 and R_2, which was 3.65 mm and 3.85 mm. As such, the printed structure matched the designed model in dimensions, showing the small shrinkage of the all-glass part fabricated by this 3D printing of glass based on direct laser melting method.

To demonstrate the feasibility as a high temperature pressure sensor and study its temperature dependence, the pressure sensor was measured in an electrical tubular furnace and the interference spectra were monitored as the temperature varied programmatically from room temperature 20℃ to 700 ℃. As the temperature increased, the cavity length increased, as shown in Fig. 3.7(a). Linear regression was applied to fit the response curve and the slope was calculated as the temperature sensitivity, which was estimated to be

$0.215nm/℃$. And the cavity length change was mainly induced by the thermal expansion of the cavity. Taken the sensor's cavity length of 359386.018 nm into consideration, the thermal expansion ratio of the cavity was calculated to be $5.9824 \times 10^{-7}℃$, which was close to the thermal expansion coefficient (CTE) of fused silica glass of $5.5 \times 10^{-7}℃$. The difference between the two values could be related to the sealed air cavity expansion under higher temperature environments, and slightly porous glass structure during 3D printing process. Nevertheless, the sensor showed the low temperature dependence and its capability of working in high temperature environments. Based on the measurement results, the temperature-pressure cross-sensitivity is found to be $67.6\ Pa/℃$.

The stability of the pressure sensor was measured by continuously recording the sensor's cavity length for a time period of 4 hours. To eliminate the influence of environmental changes, the sensor head was put in the sealed water chamber at room temperature, as shown in Fig. 3.4. The results are plotted in Figure 3.8(b). The standard deviation of the data within this period was found to be $\sigma = 22.17Pa$. The resolution of the sensor was estimated to be $2\sigma = 44.34Pa$, which is equivalent to 95% confidence.

3.1.4 Summary

In summary, an all-glass fiber-optic pressure sensor was fabricated by the three-dimensional printing based on direct laser melting method. The pressure sensor was made of all fused silica material, and its fiber housing structure was fabricated by direct three-dimensional (3D) printing of glass on top of a fused silica substrate, which also served as the pressure sensing diaphragm. A cleaved single-mode fiber (SMF) fixed inside a glass tube was inserted into the fiber housing structure and brought in close proximity to the

diaphragm, to form the FPI. And CO_2 laser irradiation was applied in thermal bonding process. Test results showed that the pressure sensitivity and resolution were 3.18 nm/kPa and 44.34 Pa, respectively, which agreed well with the simulated results, showing that the printed sensor matched the 3D model, small shrinkage was observed, and the accuracy and precision of this 3D printing of glass method were high. Moreover, temperature dependence of the sensor has been tested up to 700℃. Based on this 3D printing of glass method, the diaphragm thickness and diameter can be designed to adjust the sensitivity and measurement range. Besides, the sensor can work in high temperature environments. It is believed that this all-glass fiber-optic pressure sensor is potentially useful for pressure measurement in high temperature harsh environments.

3.2 Three-dimensional printing of bi-material strip for temperature sensing with increased temperature sensitivity

We propose an innovative method for fabricating glass and ceramic bi-layer structures, with the help of integrated laser machining method. Glass walls of different geometries can be fabricated using the extrusion-based 3D printing method. After each extrusion layer, CO_2 laser heat treatment will be processed for fused silica paste quick melting and fusing both in the printing layer and between the adjacent layers. After 3D printing of glass, ceramic layer is screen printed on side of the glass wall. And ceramic pattern can be flexibly designed and fabricated with picosecond laser ablation followed by CO_2 laser melting to satisfy different application requirements. To demonstrate the stability and functionality of the bi-layer ceramic and glass structure, a straight wall bi-layer strip

was assembled together with an optical fiber to form a Fabry-Perot interferometer. And the FPI was demonstrated for high temperature measurement.

3.2.1 High temperature sensing review

Cantilever structures have been attractive for sensing applications in recent years. The sensing mechanism is to detect the mechanical deflection of the cantilever induced by the sensing parameters' change. And various cantilever based EFPI sensors have been reported for different parameters sensing (e.g., temperature, pH, acoustic), thanks to the various micromachining techniques. More recently, a bi-material micro-cantilever based EFPI, proposed by Li et al. utilized the bi-metallic effect and was successfully applied to realize temperature measurement up to 300℃ with high sensitivity, owing to the large difference of CTE between aluminum and fused silica[72]. However, due to the low melting point of aluminum, high temperature sensing by this particular sensor was not achieved.

Ceramics and fused silica are the desired materials for applications in high temperature and highly corrosive environments[50], [54], [59]. Recently, with the rapid development of three-dimensional (3D) printing technique, 3D printing of ceramics and fused silica has been demonstrated, which offers great flexibility and simplicity to produce desired 3D structures with high thermal resistance. In this letter, we report a fused silica and ceramic bi-material strip based EFPI high temperature sensor, fabricated by the extrusion-based 3D printing of transparent glass assisted with CO_2 laser direct melting technique.

3.2.2 Proposed bi-material strip for high temperature sensing

Figure 3.9 schematically illustrates the structure of the proposed sensor. The sensor is composed of optical fiber inside a glass tube and three 3D printed fused silica walls, where two closely located parallel walls are applied as an optical fiber holder. And optical fiber is placed on top of the holding structure. The other fused silica wall is 3D printed in perpendicular to the other two glass strips, with a height slightly higher than the other two walls, performing as the temperature sensing wall. In addition, by bringing the fiber in close proximity to the glass wall, light from the optical fiber placed at the top of the two thin walls will be reflected from the sensing wall. To ensure the high reflectivity and the temperature sensing capability, gold coating is deposited on the side facing the optical fiber and ceramic layer is screen printed on the other side to form the bi-material sensing unit, respectively. When surrounding temperature changes, bi-material strip will bend. The bending of the bi-material strip will be monitored by the Fabry-Perot cavity formed by the end-face of the optical fiber and the sensing strip. The bending of one bi-material strip under temperature can be predicted by the following equations,

$$k = \frac{1}{r} = \frac{6t_1t_2E_1E_2(t_1+t_2)(\alpha_2-\alpha_1)\Delta T}{(E_1t_1^2)^2+(E_2t_2^2)^2+2E_1t_1E_2t_2(2t_1^2+3t_1t_2+2t_2^2)} \tag{3.6}$$

$$d = kL^2/2 \tag{3.7}$$

Where h is the bi-material strip' s height, t_1 and t_2 are the thickness of the 3D printed glass and screen-printed ceramics, k is the cantilever bending curvature, r is the bending radius, and α_1 and α_2 are the thermal expansion coefficient of the ceramics and 3D printed glass, and E_1 and E_2 are the Young's modulus of the 3D printed glass and ceramics, and

ΔT is the temperature change. Using equation (3.7), the cantilever tip deflection under temperature can be predicted.

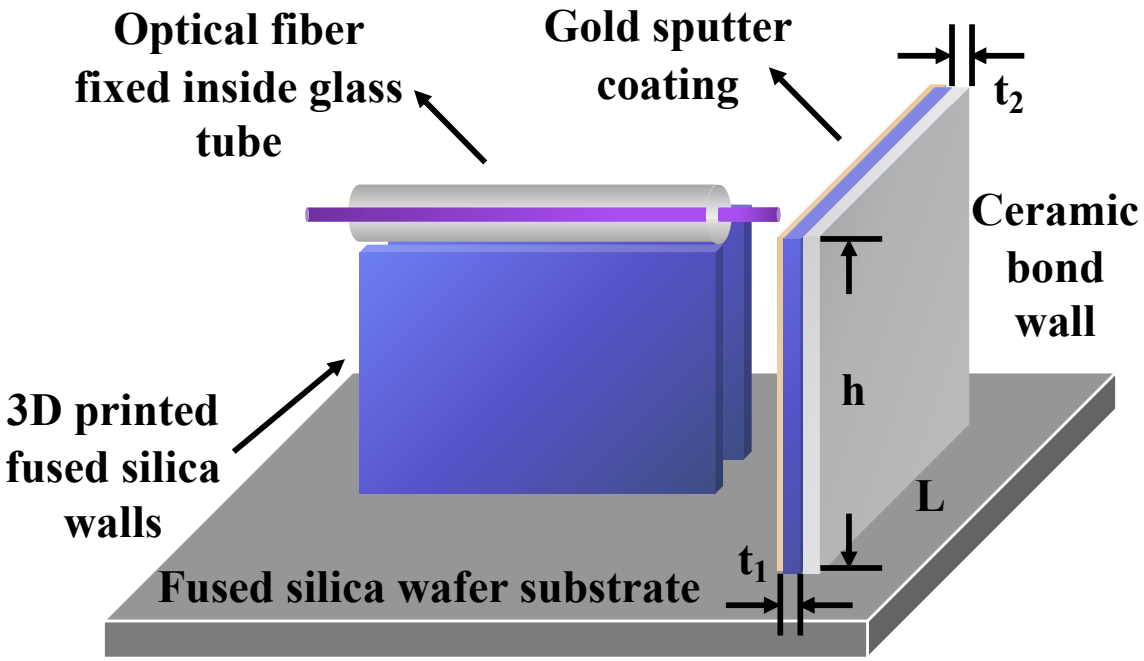

Figure. 3.8 Schematic of the bi-material strip-based temperature sensor.

3.2.3 Fabrication of bi-material strip

To fabricate the bi-material strip-based temperature sensor, 3D printing of glass process will be conducted on top of the glass substrate following the same processing procedures described in section 3.1.2. And the parameters t_1, h and L in Fig. 3.8 are 110, 2.5 mm and 10 mm. Fig. 3.9(a) shows the 3D printed glass strips. Most printed parts show transparent glass structures, while at the beginning of the sensing strip, in-transparent glass structures were printed. In addition, thanks to the unique advantage of glass 3D printing

assisted with direct laser heating method, various structures can be fabricated. As shown in Fig.3.9(b), spiral shape glass is fabricated. As such, using this glass 3D printing process, various 3D glass structures including but not limited to glass walls, glass cones can be fabricated.

To realize the bi-material strip fabrication, screen printing process will be conducted on the side wall of the 3D printed glass sensing wall. During this process, Dr. Blade was applied and ceramic adhesive (Ceramabond 503, Aremco Inc) was screen printed on the side wall. To realize good bonding between glass and ceramic adhesive, the ceramic coated structure was drying for 10 hours at lab environment with fixed room temperature. Then the structure was placed inside furnace at 100 °C for 2 hours. The other side of the glass wall was sputter coated with gold with the help of sputter coater. As such, the bi-material strip with high optical reflection was fabricated. To realize the Fabry-Perot interferometer, one optical fiber was placed inside a glass tube which was serving as a

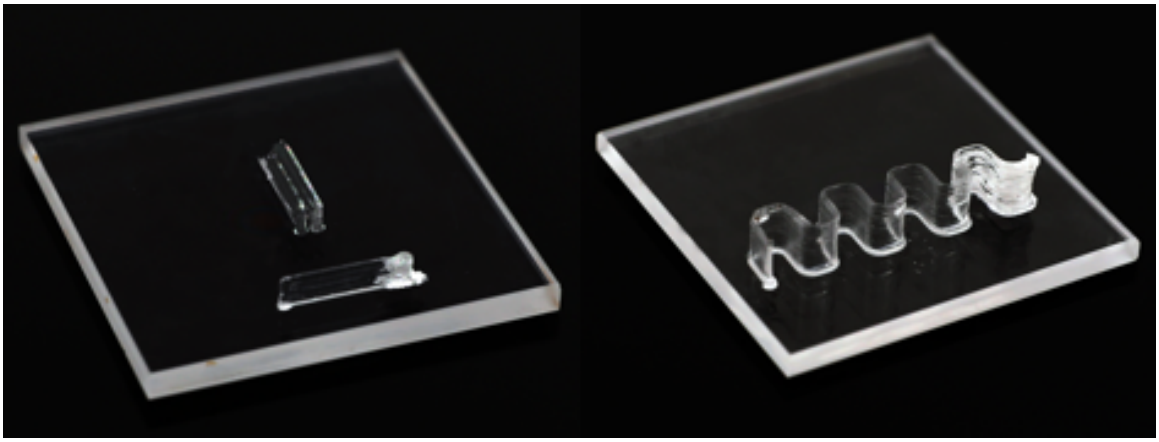

Figure. 3.9 Glass 3D printed parts with different configurations. (a) the three-wall structure (b) Spiral structure.

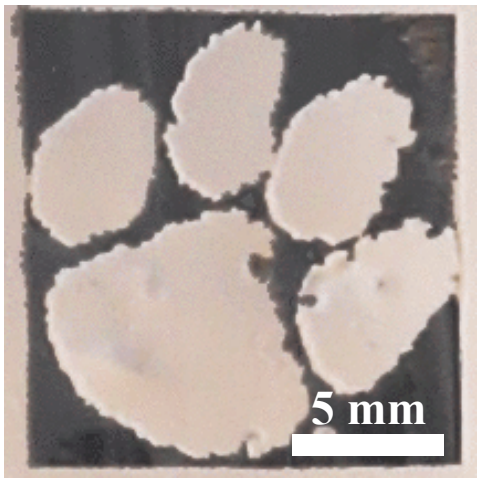

Figure. 3.10 ps laser micro-ablation for Clemson tiger paw shape structure fabrication.

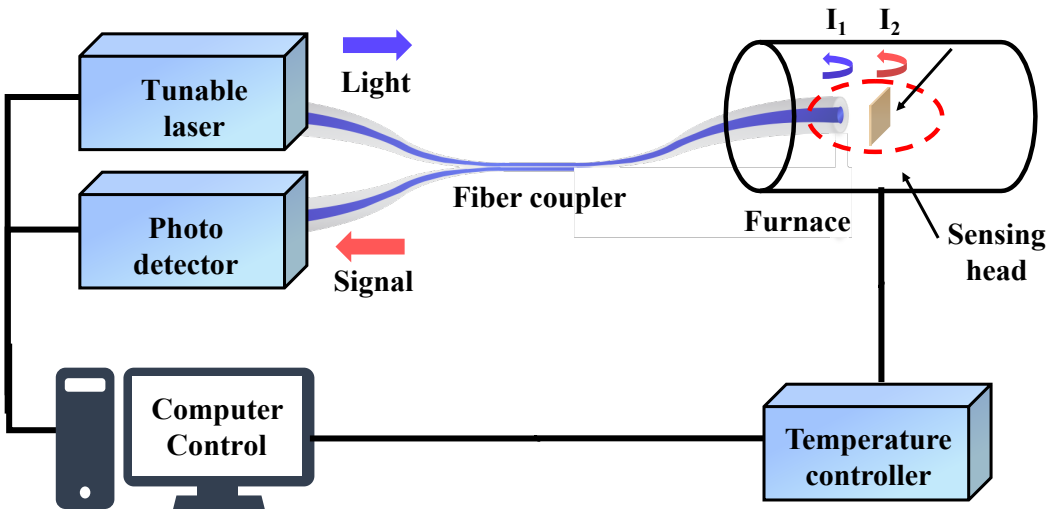

Figure. 3.11 Schematic of the high temperature test system setup, where tunable laser and photodetector was applied for optical signal insertion and receiving. And the 3D printed bi-material strip and the FPI sensor was inserted into the furnace for high temperature test up to 700°C.

protective layer and brought in close proximity to the gold coated glass wall. And the optical fiber was placed on top of the other two printed glass walls. The fixing of optical fiber was realized by the same ceramic adhesive. With the same curing procedure, the proposed sensor was fabricated. During this process, a monitoring system was used to acquire the spectra, which consisted of an optical spectrum analyzer (AQ6370D, Yokogawa), fiber coupler and broadband light source (Agilent 83437A). The fabrication parameters of h, L, t_1 and t_2 are 2.5 mm, 10 mm, 0.69 mm and 0.11 mm respectively. The Young's modulus values of printed glass and ceramic adhesive are 75 GPa, and 215 GPa. The CTE values of glass and ceramic adhesive are $5.5 \times 10^{-7}/℃$ and $7.7 \times 10^{-6}/℃$.

3.2.4 Experiments and discussions

To demonstrate the feasibility as a high temperature pressure sensor and study its temperature dependence, the fabricated sensor was measured in an electrical tubular furnace and the interference spectra were monitored as the temperature varied programmatically from room temperature 20℃ to 700℃. The spectra were monitored under every 100 ℃ change.

Figure 3.12(a) shows the spectra of the sensor when exposed to temperature of 20℃, 400℃ and 700℃, respectively, showing the spectra change under temperature. Figure 3.12(b) plots the FFT of the spectra in Fig. 3.12(a). Three main frequency components with different spatial position are located in Fig. 3.12(b). When temperature increased, the peak position shifted left, meaning that the cavity length decreased. And cavity length change of the sensor as a function of the external temperature was plotted in Fig. 3.13. A linear fit

was applied to the measured sensor data and sensitivities were calculated to be -23.5 nm/℃, with the coefficients of determination (or the R-squared values) of the curve fittings being 0.998. When taking the sensor parameters into equation 3.7), the simulated results show temperature sensitivity of -25.2 nm/℃. A small difference between the experimental results

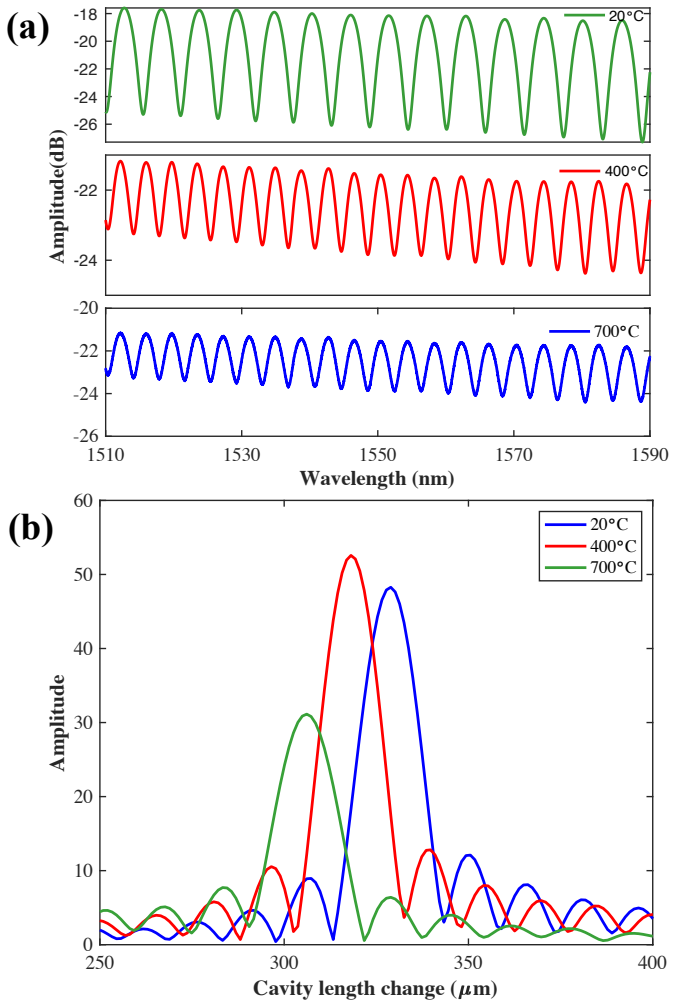

Figure. 3.12 (a) Spectra shift in response under temperature change. (b) FFT results of the sensor spectra at temperature of 20°C, 400°C and 700°C. When the surrounding temperature increased, the cavity length decreased.

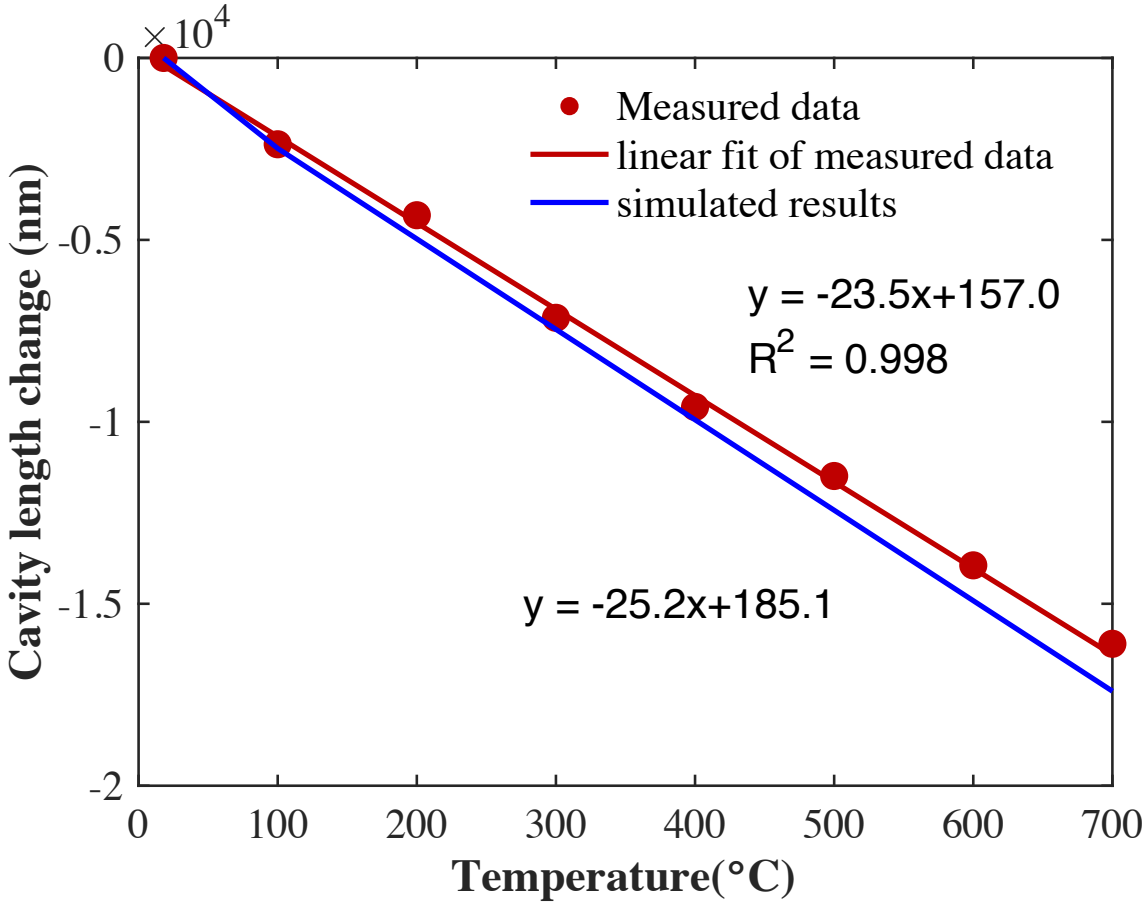

Figure. 3.13. Temperature-induced cavity length change of the temperature sensor. And the temperature response simulation of the fabricated bi-material strip was plotted.

and the simulation could be related to the small difference between the fabricated sensor dimension and model dimension, the difference of parameters (e.g., Young's modulus and CTE value) between printed glass and commercial glass.

3.2.5 Summary

In summary, a bi-material strip which is composed of ceramic and glass was fabricated by the novel Integrated Additive and Subtractive Manufacturing (IASM) method. Glass 3D printing assisted by CO_2 laser direct melting process was applied for flexible 3D structure fabrication. An integrated picosecond laser micromachining system was used for fabrication of ceramic coating layers with defined shapes. FPI sensor was realized between an optical fiber and the bi-material sensing wall. One application of this FPI sensor was for high temperature sensing. The fabricated sensor shows the enhanced temperature sensitivity thanks to the strip structure, good temperature response, all of which make it attractive for high temperature harsh environment applications.

CHAPTER FOUR

IASM for Microfluidic Sensor Fabrication

In this chapter, three microfluidic devices have been developed for different sensing applications. By utilizing fluidic' s different properties, e.g., fluidity of the liquid and refractive index of the liquid, the sensitivity of the fabricated sensors to the related parameters have been increased. Compared with the previously introduced all-glass sensors, fluidic devices will be another candidate for sensing applications and possess high sensitivities.

4.1 A microfiber half coupler for refractive index sensing

We report a reflection mode-based microfiber half coupler probe for refractive index (RI) sensing. The probe was made by cleaving a fused 2 x 2 optical fiber coupler at the center of the tapered region. When used for RI sensing, the reflection spectrum blue shifted as the surrounding RI increased. The sensing capability of the probe was tested using sucrose solutions with different concentrations. The relations between the RI sensitivity and the taper waist diameter as well as the RI range were investigated. The RI sensitivity increased quickly as the taper diameter decreased.

4.1.1 Liquid refractive index sensing introduction

In situ monitoring of liquid refractive index (RI) is of great interests in many chemical and biological applications where the RI of the liquid usually provides real time information to understand and control the processes [17], [73], [74]. Optical fiber sensors

have been widely investigated over the last several decades for RI sensing. Over the years, many optical fiber devices have been proposed and demonstrated for RI measurement such as fiber interferometers [75]–[77], fiber Bragg gratings [78], [79], long period fiber gratings [80], extraordinary optical transmission devices [38], whispering gallery mode optical resonators [27], surface plasmon resonance devices [81], single-mode-multimode-single-mode devices [82], photonic crystal fiber sensors [83] and fused optical fiber directional couplers [84]. In general, these optical fiber devices have a compact size, high sensitivity and fast response, promising broad applications for chemical and biological sensing, especially in label-free detection and monitoring of biological conditions [4,5, 7–16].

A 2x2 optical fiber directional coupler can be easily made by heating and stretching two twisted optical fibers so that their cores are close to each other in the tapered coupling region where power exchange happens. As a fundamental device, fused fiber directional couplers have been widely used in optical fiber communication and sensing, such as light branching and splitting, wavelength multiplexing/de-multiplexing and filtering. In addition, fiber directional couplers can also be used as sensors because the light coupling is dependent on the surrounding environment. For example, fiber couplers have been demonstrated for sensing force [86], temperature [87], electric current [88], magnetic field [89] and RI [84].

However, most of the reported fiber coupler sensors operate in transmission mode where the optical source and the detector are separated at two ends. Although a Sagnac loop was used to interrogate the fiber coupler sensor so that the input and output ports can be located at one single end [90], the taper waist area still needed to be fixed to prevent it

from bending, which could create large and sometimes unpredictable change in the coupling region that could make it difficult to interpret the sensor signal. In addition, due to the small size of the tapered region, the transmission mode-based sensor usually is weak and difficult to handle during applications. Hence, a reflection mode probe-type configuration is preferred for convenience, enhanced robustness and improved signal stability. Recently, a microfiber half coupler based sensor, proposed by Ding et al. [87], was successfully applied to mapping temperature (up to 1283˚C) distributions with high spatial resolution.

In this paper, we report a microfiber half coupler probe for RI sensing. The probe was fabricated by precisely cleaving a fused optical fiber coupler. Compared with the transmission mode-based coupler sensors, the reflection-based probe can access the sample through a small single point of insertion. The probes were tested for in situ measurement of RI variations of liquids. Considering the nonlinear response of the probe to refractive index, the probes were also studied for RI sensitivity dependence on the taper waist in different RI ranges.

4.1.2 Fabrication and Principle

Figure 4.7(a) is the schematic of a typical 2x2 fused optical fiber directional coupler. The coupler can be modeled by two touching cylindrical waveguides side by side in its tapered waist with four input/output ports (Port 1-4). Figure 4.7(c) shows the schematic of the cross section of the tapered region. The coupling coefficient can be described as [91]:

$$C_{WC} = \frac{2.405\lambda}{2\pi a^2 n_2 \sqrt{\pi D}} V^{-\frac{3}{2}} e^{-V(2D-2)} \quad (4.1)$$

where n_2 and n_3 refer the refractive indices of the optical fiber cladding and the surrounding environment, respectively; a denotes the diameter of the tapered fiber; $V = 2\pi a(n_2^2 - n_3^2)^{1/2}/\lambda$ is the normalized propagation constant of the tapered fiber; D is defined as D=d/2a to describe the fusion degree, where d is the inter-core distance, in our case.

If light enters Port 1, then the normalized power in Port 4 is given by:

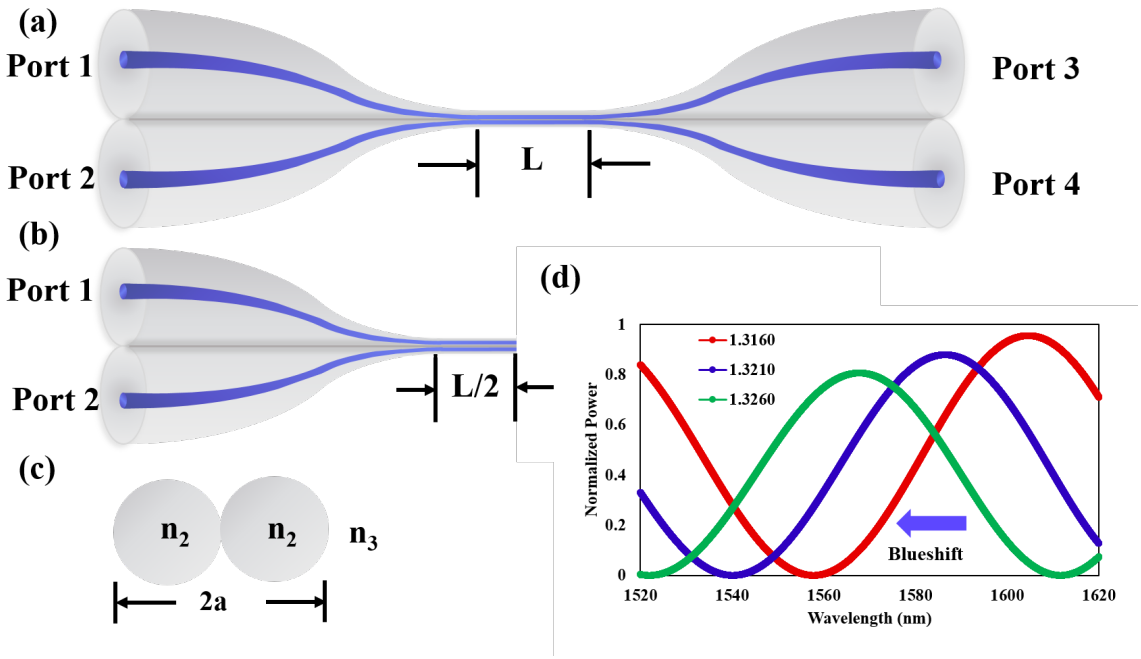

Figure 4.7. Schematics of (a) a 2x2 optical fiber directional coupler and (b) a fiber half coupler, (c) Cross-section of the tapered waist region, (d) simulated spectra of the half coupler immersed in different RI solutions.

$$P_4 = cos^2\varphi \tag{4.2}$$

where $\varphi = C_{WC}L$ and L is the length of the coupling region.

Fig. 4.7(b) shows the schematic of the proposed half coupler in half. The light enters Port 1 and is partially coupled to the other fiber while the rest continuously propagates in the original fiber. Then at the cleaved end of the fiber coupler, the split two beams are partially reflected, propagate backwards and go through the coupling region again. Based on the reciprocity of light propagation, the half coupler can be modeled as a full coupler with the coupling length of L given by Eq. (4.1) but adding the proportional term as a result of the Fresnel reflections. As such, the normalized power in Port 2 of the half coupler is:

$$P_2 = \left(\frac{n_2 - n_3}{n_2 + n_3}\right)^2 cos^2(\varphi) \tag{4.3}$$

According to Eq. (4.1) to (4.3), the output power in Port 2 depends on the refractive index n_3 of surrounding environment, wavelength λ, coupling length L, and taper waist diameter 2a.

The surrounding RI (n_3) change will alter the coupling coefficient and lead to the spectra shift. We then performed simulations to evaluate the RI dependence of the probe. The length, taper diameter, and refractive index of the fiber cladding were assumed to be L=2cm, a=3.3μm and n_2=1.4444, respectively and the surrounding refractive index (n_3) was taken three different values of 1.3160, 1.3210 and 1.3260. The results are shown in Fig. 4.7(d), where the output power drops due to the changes in the Fresnel reflection as the RI increases. In addition, as the RI increases the spectrum shifts to shorter wavelength (blue shift). The sensitivity (S) of the spectral shift with respect to the surrounding RI can be derived as:

$$S = \frac{\partial \lambda}{\partial n_3} = -\frac{\partial \varphi / \partial n_3}{\partial \varphi / \partial \lambda} \tag{4.4}$$

4.1.3 Experiments and Discussions

The half coupler was made by laterally fusing and tapering two twisted single mode optical fibers (Corning, SMF-28e) together using a home-made tapering and cleaving integrated system. An online monitoring system was used to monitor the transmission spectrum of the fiber coupler during the tapering process, which consists of an Erbium-

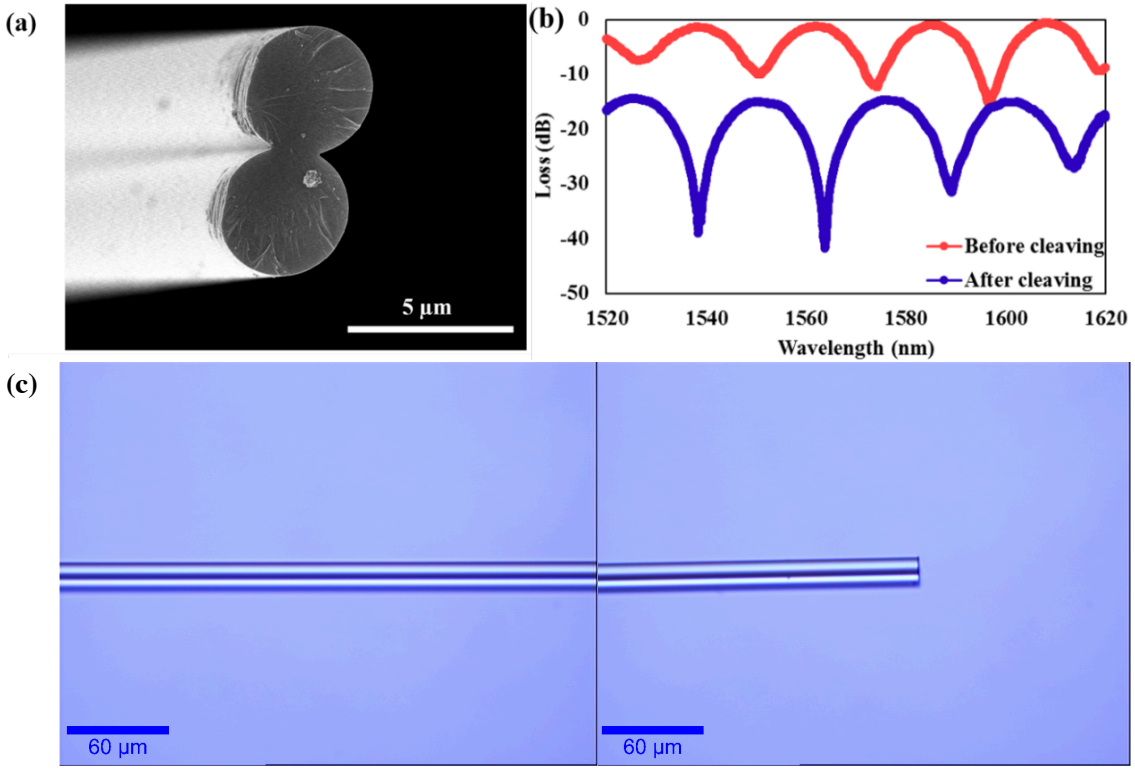

Figure 4.8. (a) SEM image of the endface of the half coupler. (b) The transmission spectrum (Port 4) of the fiber coupler (red, before cleaving) and the reflection spectrum (Port 2) of the half coupler (blue, after cleaving). (c) Microscope image of the taper waist.

doped fiber amplified spontaneous emission broadband light source connected to Port 1 and an optical spectrum analyzer (OSA, AQ6319) connected to Port 4 as illustrated in

Figure 4.7(a). After the tapering process, a fiber cleaver was moved to the center of the taper waist for cleaving the coupler to form two equal half-couplers [92]. The reflection spectrum was acquired by connecting Port 2 to the OSA.

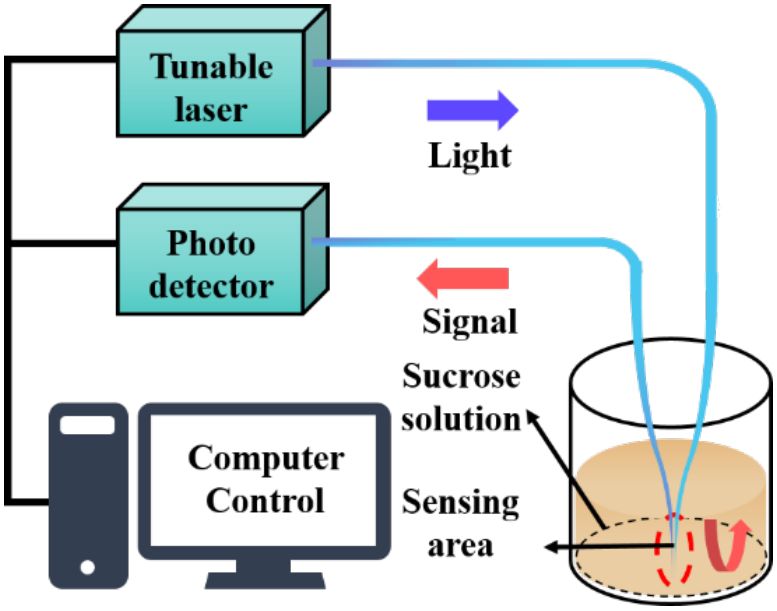

Figure 4.9. Schematic of the experiment setup to test the RI measurement capability of the half-coupler probe.

Fig. 4.8(a) shows the scanning electron microscope (SEM) image of a representative half coupler. The cleaved endfaces are flat and the cleaving mark can also be seen on the lateral side of the coupler. The two fibers were parallel and fused together and the taper waist (2a) was estimated to be 7.7 μm. The two fibers maintained their cylindrical shapes to form a weakly coupling condition. Fig. 4.8(b) shows the transmission spectrum of the full coupler (red, before cleaving) and the reflection spectrum of the half coupler (blue, after cleaving). The half coupler spectrum has the multi-peak patterns similar

to the full coupler, except that there is about 14 dB drop in intensity as a result of the Fresnel reflection at the

Table 4.1. Sucrose solution weight percent versus RI at 1550 nm

Weight percent	RI	Weight percent	RI	Weight percent	RI
0%	1.3166	6%	1.3253	31%	1.3659
1%	1.3180	16%	1.3406	32%	1.3677
2%	1.3195	17%	1.3422	33%	1.3695
3%	1.3209	18%	1.3438	45%	1.3926
4%	1.3223	19%	1.3454	46%	1.3946
5%	1.3238	20%	1.3470	47%	1.3967

glass-air interface and a phase difference of about π because the deviation of the cutting position from the middle point of tapering region. Unless the coupler is cut exactly in the middle, there will be a phase difference between the half-coupler and the full coupler.

The experimental setup for investigating RI measurement capability of the fabricated probes are schematically shown in Fig. 4.9. The light from a tunable laser (AQ8460L, ANDO) is injected into the half coupler from Port 1 and the reflected signal from the coupler is detected at Port 2 via a photodetector (AQ8461, ANDO).

The half coupler-based probe was immersed in a sucrose solution at room temperature to study its response to the surrounding RI change. The RI of the sucrose solution was changed by increasing the sucrose concentrations, which were adjusted to

four regions and shown in Table 4.1 [93]. In each measurement cycle, acetone was used to rinse the probe carefully after each measurement to ensure that there were no solution residues attached on the surface of probe surface, indicated by the interference spectra

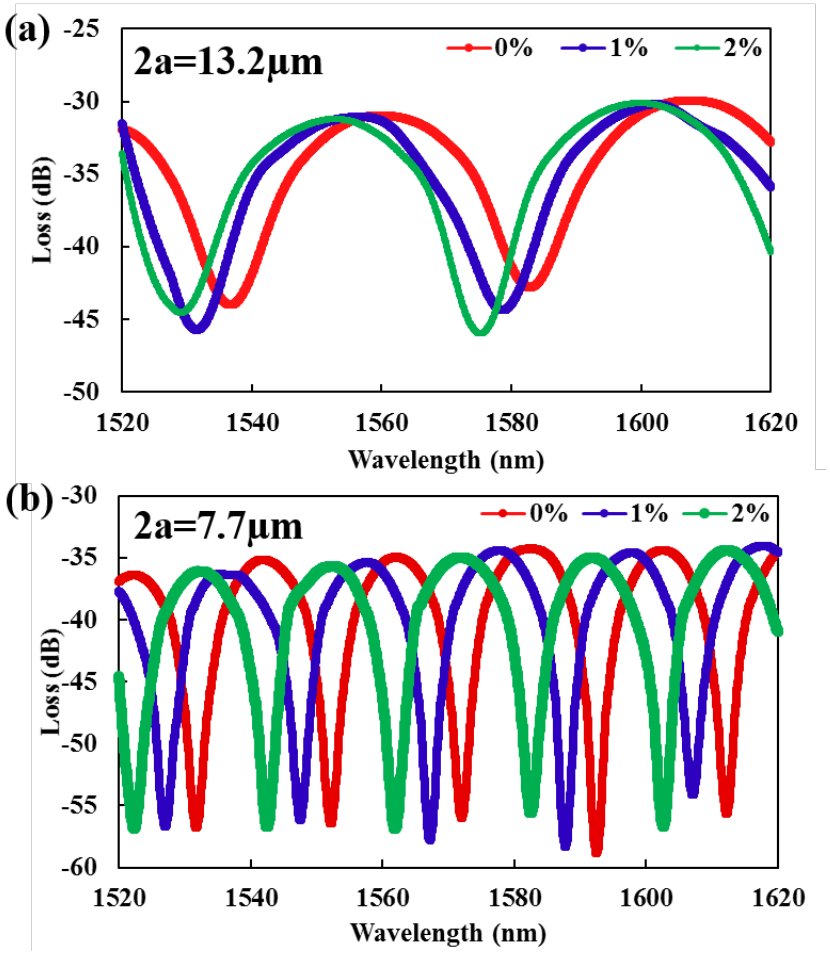

Fig. 4.10. Spectra of half coupler probes with taper waist diameters of (a) 13.2 μm and (b) 7.7 μm in sucrose solutions of different concentrations.

returned to its original one in air.

To study the relation between the RI sensitivity and the taper waist, four half-coupler probes with taper waist (2a) of 13.2 μm, 9.6 μm, 7.7 μm and 4.2 μm were selected and tested in the concentration range of 0%-6%. The diameters of the taper waists were measured by a high-resolution optical microscope (Alpha 300s, Witec). Fig. 4.10 shows the spectra of half coupler with taper waist of 13.2 μm (Fig. 4.10(a)) and 7.7 μm (Fig. 4.10(b)) in sucrose solutions at the concentrations of 0%, 1% and 2%. In general, the spectra maintained good contrast and the spectra blue-shifted monotonically as the RI increased.

The wavelength shifts as a function of the ambient RIs were plotted in Fig. 4.11(a). Linear regressions were used to fit each response curve and the slopes of the fitted lines were calculated as their RI sensitivities, which were estimated to be 2248.5 nm/RIU, 2362.6 nm/RIU, 2661.6 nm/RIU and 3054.0 nm/RIU, respectively, with the correlation coefficients (or the R-squared values) of the curve fittings being 0.984, 0.999, 0.999 and 0.981, respectively. The sensitivity shows the trend of improvement with a smaller taper waist diameter. The RI sensitivity as the function of the taper waist diameter was calculated based on Eq. (4.4) and is plotted as the blue curve shown in Fig. 4.11(b). In general, the measured sensitivity agreed with the simulation results in general trend. The difference between the measured values and calculated results may be caused by the inaccurate measurement of the taper diameters and the temperature cross-sensitivity induced by the thermo-optic effects and thermal expansion of optical fiber under temperature variations [94].

It is expected that the RI sensitivity can be further enhanced by reducing the taper waist diameter. However, a probe with a smaller taper waist diameter is more fragile compared with the ones with larger diameters. The smaller of the microfiber is, the longer the probe becomes, which increases the chance of bending induced errors. In addition, to

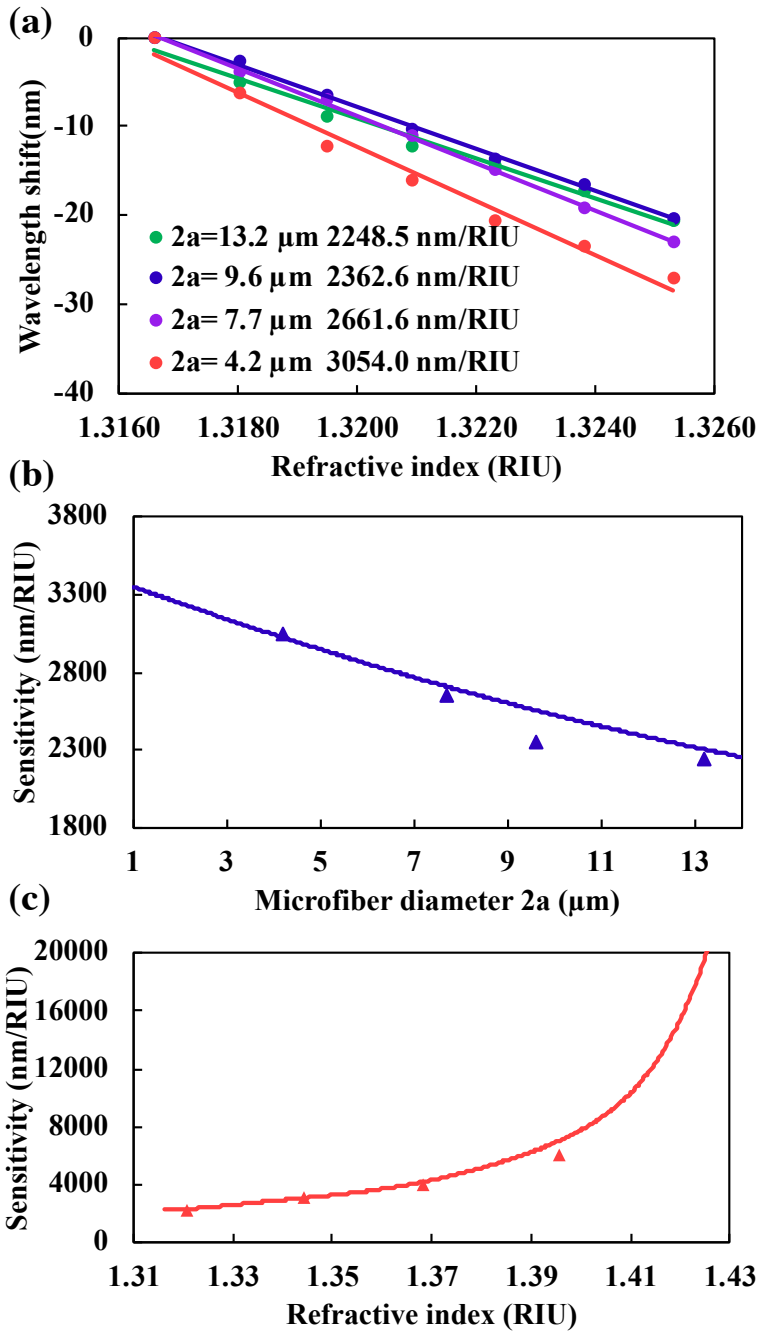

Fig. 4.11. (a) Spectral shifts of the four probes with different diameters in response to RI changes. Sensitivities as a function of (b) taper waist diameter 2a and (c) the RI range, respectively.

avoid ambiguity, the dynamic range of the probe is preferred within the FSR of the spectrum. A small waist diameter would also reduce the FSR and thus limit the RI measurement range. Therefore, there are trade-offs among the RI sensitivity, RI measurement range and mechanical robustness. Probes with small taper diameters can be applied to measuring RI changes within a small range but with high sensitivity. For RI measurement in a large range, probes with large waist diameters are good alternatives.

The probe with the waist diameter of 13.2μm was selected to study the probe performance in different RI regions. Fig. 4.11(c) plots the RI sensitivity S in the four different RI regions listed in Table 4.1. The median value of each RI region was used to represent the RI sensitivity of each region. The calculated sensitivity as a function of surrounding RI is also shown in Fig. 4.11(c), which agreed well with the experimental results.

The sensitivity of the probe increases as the surrounding RI increases. This is because the evanescent wave has a larger penetration depth into the surrounding media when the RI becomes larger. The experimental results agreed well with the simulation results in trends though the exact sensitivity values because of the fiber parameters, the uniformity of the taper region as well as the measured taper diameters may not exactly match those used in simulations.

4.1.4 Summary

In summary, a microfiber half coupler was investigated for RI sensing. The probe was made by cleaving a fused fiber directional coupler at the center of its taper region. When used for RI sensing, the reflection spectrum blueshifted as the surrounding RI

increased. The RI sensitivity was tested to be 6142.0 nm/RIU within the RI range of 1.39-1.40, which is similar to other types of fiber sensors. The RI sensitivity increased as the taper diameter decreased or the surrounding RI increased. The half coupler-based RI probe has the advantages of reflection mode operation and small size for in situ chemical and biological sensing.

4.2 Glass 3D printing of microfluidic pressure sensor interrogated by fiber-optic refractometry

This part reports a novel fused silica microfluidic device with pressure sensing capability that is fabricated by integrated additive and subtractive manufacturing (IASM) method. The sensor consists of a capillary and a 3D printed glass reservoir, where the reservoir volume change under pressure manifests liquid level deviation inside the capillary, thus realizing the conversion between small pressure change into large liquid level variation. Thanks to the design flexibility of this unique IASM method, the proposed microfluidic device is fabricated with liquid-in-glass thermometer configuration, where the reservoir is sealed following a novel 3D printing assisted glass bonding process. And liquid level is interrogated by a fiber-optic sensor based on multimode interference (MMI) effect. This proposed microfluidic device is attractive for chemical and biomedical sensing because it is flexible in design, and maintains good chemical and mechanical stability, and adjustable sensitivity and range.

4.2.1 Review of state-of-art microfluidic pressure sensing device

Accurate and in-situ pressure monitoring is of great importance in many chemical and biomedical applications, especially in microfluidic systems [1-4]. Thanks to the advancement of microfluidic technology, which has realized the reduction of sample volume as well as the integration of multi-functions, lab on chip (LOC) progress has accelerated and complex microfluidic systems have been developed and widely applied for chemical and biomedical applications [33], [95]–[100]. Having the ability to measure the pressure at desired position inside the microfluidic system can provide invaluable information for better process understanding. The continuous pressure monitoring will also enable data analytics to inform decision making and determine process control procedures. A typical microfluidic pressure sensor utilizes the fluidic pressure induced diaphragm deflection, liquid-air interface change as the sensing unit, amplifies the variation with the help of fluid and further transduces the signals to visual, electrical and optical readouts [1-4]. In general, these devices are small in size, with adjustable sensitivity and range, and easy to be integrated with microfluidic systems.

Most of these aforementioned sensors are carried out in polymer materials, like Polydimethylsiloxane (PDMS), benefiting from its good optical transparency, biocompatibility and easy to be fabricated by well-developed soft lithography technique. However, PDMS and other polymer-based materials also have some limitations, in particular when considering long-time thermal and chemical stability [101]. As one of the high-performance materials, fused silica is the desired material for specialized systems which require chemical and mechanical stability, and great optical transparency [101]. In

addition to the well-demonstrated femtosecond laser irradiation followed by chemical etching (FLICE) for microfluidic system fabrication method, the emerging three-dimensional (3D) printing of glass method shows a great potential as a candidate for microfluidic network built-up [46], [102], [103]. Recently, Kotz et al has proposed a technique by combination of 3D printing of glass method and sacrificial template technique for 3D suspended hollow structures in fused silica glass [103]. And in our previous work, 3D printing of glass using direct laser melting method has been reported, which accelerates the glass 3D printing procedure by eliminating time-consuming post-treatment process[54], [102]. These techniques could be potentially applied to fabricate complex microfluidic systems. More importantly, optics and microfluidic systems can work synergistically in 3D printed glass structures to realize optofluidic-based systems.

As one of commonly applied waveguides, optical fibers have been widely exploited in chemical and biomedical sensing applications, with advantages such as immunity to electromagnetic interference (EMI), compact size, high sensitivity and multiplexing capability[11], [21], [22], [28], [66], [70], [102], [104]–[106]. In particular, optical fibers are good candidates for pressure sensing. The most popular configurations of fiber-optic pressure sensors involve the detection of mechanical deflection as well as the light and matter interaction[25], [65], [66], [102]. Optical fiber pressure sensors have been successfully demonstrated to be integrated into PDMS based microfluidic systems and glass based optofluidic systems fabricated by FLICE process[33], [105], [106]. Additionally, glass 3D printing has been demonstrated for optical fiber pressure senor fabrication. Composed of the same material, the demonstrated all-glass sensor shows the

potential for pressure measurement in harsh environments [102]. However, the sensing capability is highly dependent on the diaphragm's dimension, which is limited by the size of optofluidic systems.

In this paper, we combine 3D printed glass structure and microfluidic sensing mechanism, report a prototype pressure sensing device with adjustable sensitivity and range, and with mechanical and chemical stability[107]. In this unique Integrated Additive and Subtractive Manufacturing (IASM) system, glass 3D printing assisted with direct laser melting allows rapid fabrication of all-glass reservoir with flexible dimensions. Integrated picosecond laser micromachining system can be applied for precise dimension tuning and

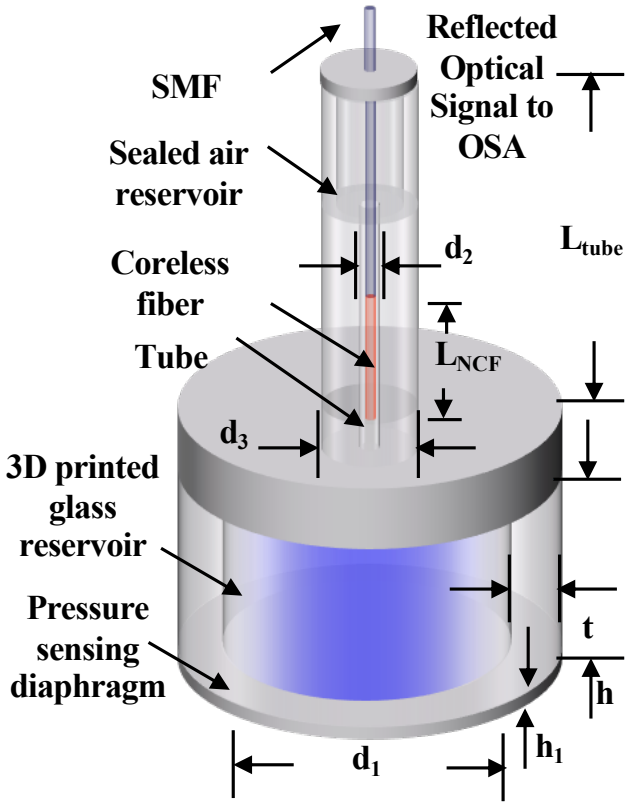

Figure 4.12. Schematic of the microfluidic pressure sensing device that is interrogated by optical fiber sensing structure.

glass refractive index change, for further waveguide inscription. To demonstrate the pressure sensitivity enhancement and tuning capability, one prototype microfluidic structures are fabricated by IASM method, with liquid-in-glass thermometer. Then a fiber optic sensor utilizing multi-mode interference (MMI) effect is inserted into one capillary for pressure induced liquid level change. Simulation and pressure test of the sensor with liquid-in-glass configuration are presented.

4.2.2 Working principle of microfluidic pressure sensor

The schematic and design of the proposed sensor structure is shown in Fig. 4.12. The sensor is composed of a liquid reservoir, capillary, a sealed air reservoir and an MMI fiber sensor. The liquid reservoir is connected to the capillary and a fiber optic sensor is placed inside tube, which serves as the sensing channel. When the external pressure changes, the diaphragm deflection induces liquid reservoir volume change, forcing the liquid into capillary and rising the liquid level. In theory, pressure change will induce deflection of the whole structure. However, since the other parts of the sensor have a much smaller size to thickness ratio compared to the one of sensing diaphragm, pressure change induced deflection in other parts is negligible. Considering the volume of liquid inside the sensor is the same before and after pressure, the liquid-air interface change inside the capillary can be expressed as [108]:

$$\Delta l = \frac{\Delta V_r}{S_c} \tag{4.5}$$

where S_C denotes the empty cross-sectional area of the capillary, which is calculated by the subtraction between capillary cross-section and optical fiber cross-sectional area. And ΔV_r

refers to volume change of the reservoir. When under pressure change P, center deflection of the diaphragm can be given by [102]

$$\Delta d = \frac{3(1-\mu^2)(d_1/2)^4}{16E{h_1}^3} P \tag{4.6}$$

where d_1 and h_1 are the diameter and thickness of the pressure sensing diaphragm as shown in Fig. 4.12. E and μ are the Young' s modulus and Poisson' s ratio of the diaphragm. When pressure increases, decreased air area in sealed tube should create a counter-pressure to the liquid, considering the large air reservoir in Fig.4.12, counter pressure will be limited and neglected in simulation. And the volume change induced by deflection of diaphragm can be described as [109]

$$\Delta V_r = \frac{\pi(d_1/2)^2}{3} \Delta d \tag{4.7}$$

By combining Equation (4.5) to (4.7), the length change as a function of the applied pressure (P) is given by

$$\Delta l = \frac{d_1^2}{3(d_2^2 - d_{fiber}^2)} \cdot \frac{3(1-\mu^2)(d_1/2)^4}{16Eh_1^3} P \tag{4.8}$$

where d_2 and d_{fiber} are the inner diameter of the tube and the outer diameter of optical fiber, respectively. Eq. (4.8) indicates that the liquid level change is amplified from the deflection of the diaphragm by the ratio between cross-sectional areas of reservoir and capillary. As such, the dimensions of the reservoir and capillary play a critical role on the tuning of pressure sensitivity. It is also observed that the liquid level change is linearly proportional to pressure.

The liquid level change can be interrogated by fiber-optic sensors. As shown in Fig. 4.12, a fiber-optic sensing structure is placed inside capillary. This sensing unit is

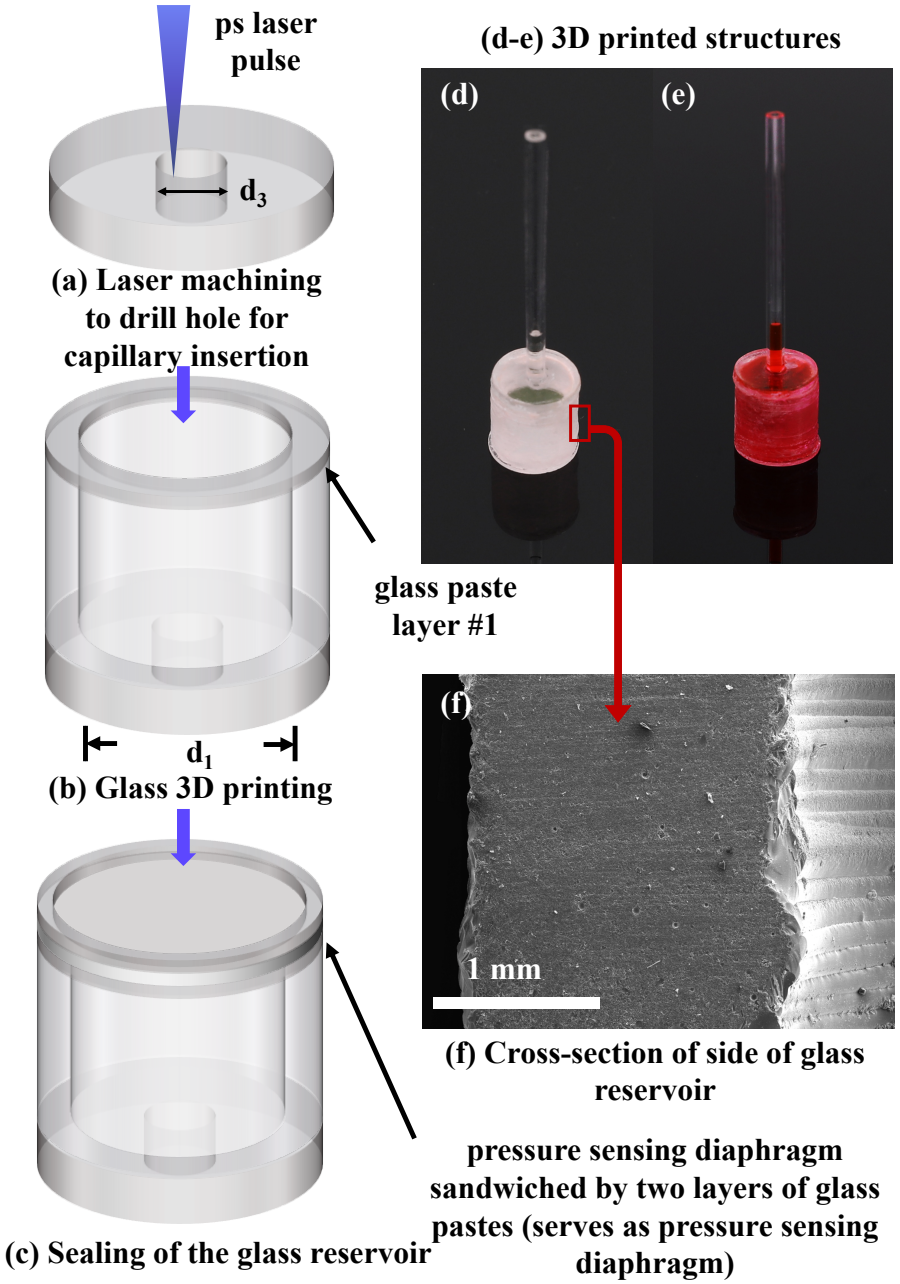

Figure 4.13. Schematic of the IASM fabrication process. (a) ps laser micromachining for hole drilling. (b) glass 3D printing for reservoir fabrication. (c) glass 3D printing assisted reservoir sealing process. (d) Image of 3D printed structure and (e) red liquid filled the liquid reservoir. (f) SEM image of cross-section of liquid reservoir' s side wall.

composed of a single mode fiber and a section of coreless fiber, thanks to the multi-mode interference (MMI) effect [110]. Similar to the transmission mode single-mode multi-mode single-mode (SMS) structure, input light propagates through the multi-mode fiber, reflects at fiber and surrounding environment interface due to Fresnel Reflection, propagates back and generates interference maxima or minima in reflection spectrum. Because of evanescent field coupling, when coreless fiber is surrounded by liquid, surrounding liquid in the MMF region will result in a spectral shift in reflection spectrum of sensor. And liquid level variation can be correlated to spectral shift.

4.2.3 IASM for microfluidic device fabrication

Fig.4.13 schematically illustrates the microfluidic device fabrication process with the help of IASM system. In this unique IASM system, glass 3D printing by direct CO_2 laser helps to fabricate flexible structures, with a dimension accuracy melting on the order of hundreds of microns [54], [102]. The integrated ultrafast laser micromachining presents a high dimensional accuracy (micron or even submicron fabrication accuracy) [50]. As such, this IASM method shows the high dimensional fabrication accuracy. To fabricate the proposed microfluidic device, a hole with diameter of d_3=2.1mm will be drilled for capillary inlet, at the center of a fused silica substrate (Corning 7980, with thickness of 500μm), by picosecond laser (Olive-1064-10; Attodyne, Inc. Toronto, ON, Canada, 1064 nm). Then glass 3D printing assisted with CO_2 laser melting (10.6 μm, ti100W, Synrad) will be conducted on its top with the same process flow as described in our previous paper [102], with inner diameter d_1=8.7mm and wall thickness t=2mm. After reaching the desired reservoir height (h=7.8mm), glass 3D printing will be stopped after paste extrusion process,

as shown in Fig. 4.13(b). Then a glass substrate (Corning 7980, with thickness of h_1=100μm), which serves as pressure sensing diaphragm, will be placed on top of the paste layer. Afterwards, another glass paste layer will be extruded (eco-Pen300, Preeflow) on top of the glass substrate. As such, the pressure sensing diaphragm is sandwiched between two layers of glass paste, as shown in Fig.4.13(c). After 60 seconds time delay, CO_2 laser irradiation will be processed for quick melting and fusing both inside the sandwiched structure and between the adjacent layers with optimized output parameters[54], [60], [61], [102]. As such, a sealed reservoir is printed.

During the 3D printing assisted glass sealing step, after the first glass paste layer has been extruded, pressure sensing diaphragm was placed on its top immediately. one-minute delay time was processed to ensure drying of the paste and thus the fixing in position between the paste and cover glass. Then another glass paste layer was extruded on its top. After the same time delay, CO_2 laser beam was focused onto the top glass paste layer for paste melting, with the same scanning settings as the ones during glass reservoir printing process. Additionally, the cover glass thickness could be flexibly varied. CO_2 laser output power will be adjusted correspondingly to realize melting both inside the sandwiched structure and between the adjacent layers, to achieve the sealing process. In this case, the thickness of each glass paste layer, which is roughly 100 μm, is very similar to the one of cover glass substrate. As such, CO_2 laser scanning parameters were unchanged in sealing process.

Fig.4.13(d)-(e) show the photos of the 3D printed structures. As shown in Fig.4.13(d), the 3D printed glass reservoir was sealed with two glass substrates. The bottom

thin glass substrate serves as the pressure sensing diaphragm. On the top glass substrate, a capillary (with inner diameter (ID) of 0.6 mm and outer diameter of 2 mm) is inserted through the hole drilled by ps laser and works as the sensing channel. Additionally, it is noticed that the 3D printed reservoir in Fig.4.13(d) is not very transparent, which should be related to the porous glass structure resulting from the CO_2 laser irradiation process. Fig.4.13(f) shows the SEM images of the cross-section of liquid reservoir' s side wall, thickness of which is roughly 2 mm. It is observed that micro pores exist, which resulted in in-transparent printed structure. Nevertheless, confined red liquid in Fig.4.13(e) indicates good sealing realized in the IASM sealing process in Fig.4.13(c). By adjusting the output laser parameters, porosity of 3D printed glass can be tuned.

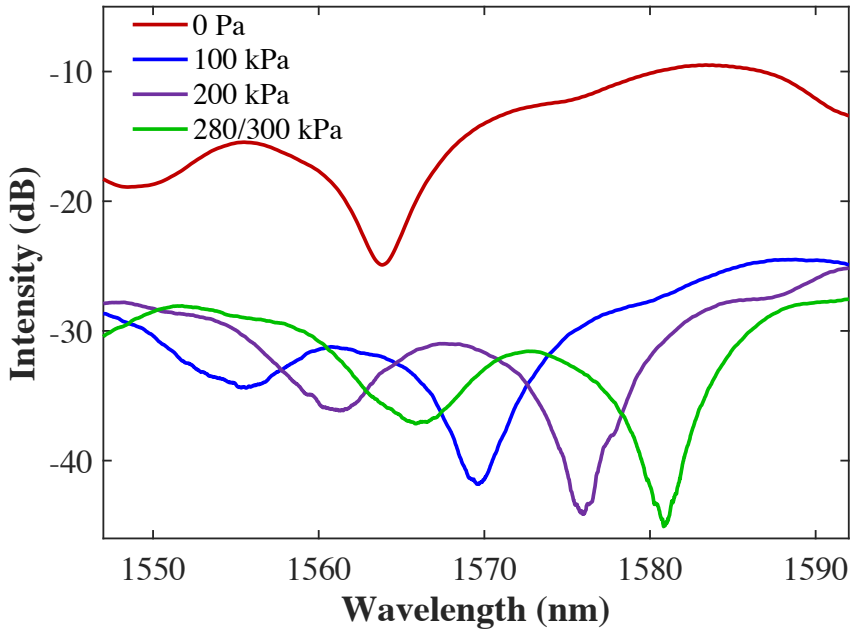

Figure 4.14. Reflection spectra of packaged optical fiber sensor, which was inside the capillary of microfluidic device, under hydrostatic pressure change.

4.2.4 Sensor's pressure response test

To interrogate pressure induced liquid level change, optical fiber sensing structure is applied and inserted into the capillary channel. As shown in Fig.4.12, a section of coreless fiber (with a diameter of 125 μm) is spliced to a single mode fiber and cleaved roughly 20.3 mm away from the splicing position, forming a reflection-mode MMI device. A broadband light source (Agilent 83437A), an optical spectrum analyzer (AQ6370D, Yokogawa) and fiber circulator were used to monitor reflection spectra of the fiber optic sensor. As shown in Fig.4.14, the valleys in the spectrum were formed due to destructive interferences among different optical modes.

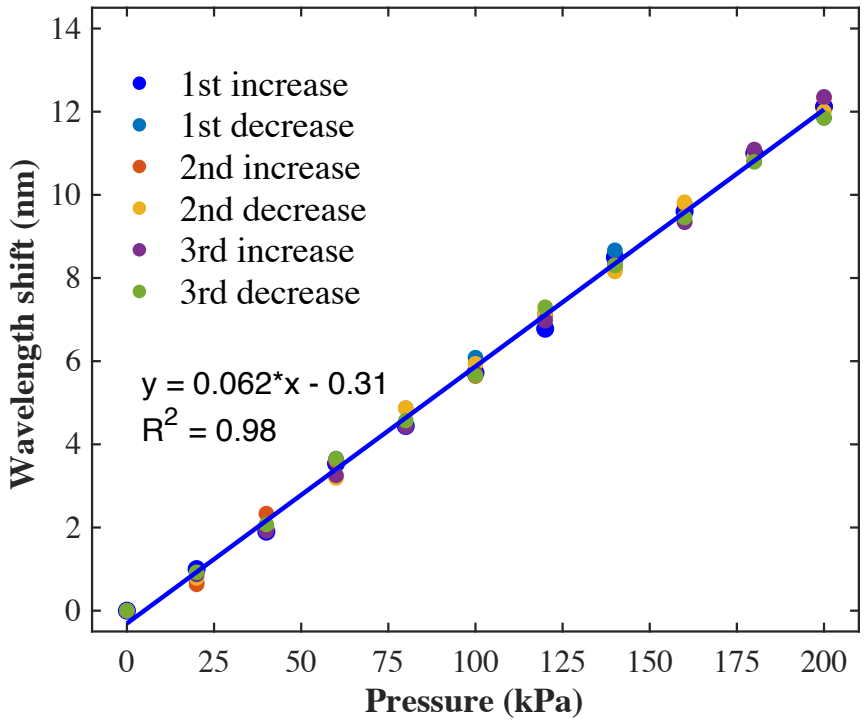

Figure 4.15. Wavelength shift of the packaged fiber optic sensor when the microfluidic sensor was under pressure.

To demonstrate pressure sensing capability of the proposed microfluidic device, fiber-optic sensor was assembled together with the 3D printed structure as shown in Fig.4.13(d). Air reservoir was realized by horn shape inner air cavity at top of tube in Fig.4.13(d). First, the connected region of the reservoir and capillary was sealed with adhesive (Loctite, E-20HP). Then, alcohol (Reagent Alcohol, 95%, VWR analytical) was pumped inside reservoir with help of syringe pump through a capillary that was inserted to the bottom of reservoir, ensuring that no air bubbles were trapped inside. Liquid pumping was stopped when liquid level reached top of the reservoir. Then fiber-optic sensing region was inserted into the tube and brought into proximity to the liquid-air interface. As the final step, the outlet was sealed with adhesive. In our experiment, an elongated capillary tube (L_{tube}=~6cm) was applied for sensing channel.

The pressure sensitivity of assembled microfluidic device was characterized inside a sealed hydrostatic pressure chamber in a controlled temperature environment [102]. Pressure was applied through a hydrostatic test pump and monitored through a commercial pressure gauge (0.5% measurement accuracy). The reflection spectra were detected via OSA and recorded every 20kPa increasement from 0 to 200kPa. During each pressure change process, 30-min waiting time was set to ensure that the device's response was stabilized. Fig.4.14 shows the reflection spectra of the sensor under hydrostatic pressures of 0, 100, 200 and 280/300kPa. When pressure increased, it can be observed that the valley corresponding to MMI shifted towards longer wavelength resulting from the longer liquid immersion region. Additionally, when continuing to increase pressure to 280 and 300kPa, spectra showed no shift, indicating liquid level change already covering the whole no-core

fiber at 280kPa. Liquid level sensitivity was calculated as ~0.073mm/kPa, showing a small difference from simulated one obtained from Eq. (4.8) as 0.064mm/kPa. It should be related to small area deviation of pressure sensing diaphragm from model size [102], ID deviation of tube and neglected counter pressure provided by sealed air. When compared with pressure sensors based on diaphragm deflection[95], [97], [102] liquid level change under pressure was 74 times as high as the diaphragm deflection. Additionally, microfluidic sensors with higher pressure sensitivities like ~0.6 [96] and 5.3 [98] mm/kPa were reported for intraocular pressure monitoring applications.

Intensity of the spectra decreased when pressure increased, which was related to longer coreless fiber inside liquid, introducing evanescent wave penetrating into liquid. In addition, the power drop was related to the changes in Fresnel reflection as surrounding medium of end-face changed from air to liquid. Fig.4.15 shows linear spectral shift under pressure. A linear fit was applied to the valley of MMI to correlate the relation between wavelength shift and pressure change, and the sensitivity was calculated as 0.062nm/kPa. And good repeatability can be found during three cycles of pressure test.

4.2.5 Temperature crosstalk discussion

Considering the large difference between the coefficient of thermal expansion of the liquid and glass reservoir, the temperature sensitivity may be much higher compared with its pressure sensitivity. And we believe that for this specific device, considering its relatively big size, especially the large reservoir (with height of 1 cm, and inner diameter of 8.7mm), it will be a more temperature sensitive sensor rather than a pressure sensor. To

simulate or estimate the temperature response, the theoretical liquid level change under temperature deviation can be conducted by the following equation:

$$\Delta L_{liquid_{level_{temp}}} = ((CTE * \Delta T + 1)^3 - 1) * V_{reservoir}/(S_{tube} - S_{fiber})$$

$$\approx (3 * CTE * \Delta T) * V_{reservoir}/(S_{tube} - S_{fiber}) \quad (4.9)$$

Taking the parameters of tube and reservoir, CTE value of alcohol into equation (4.9), it is found that in under ~4°C change, the liquid level deviation in tube will be roughly

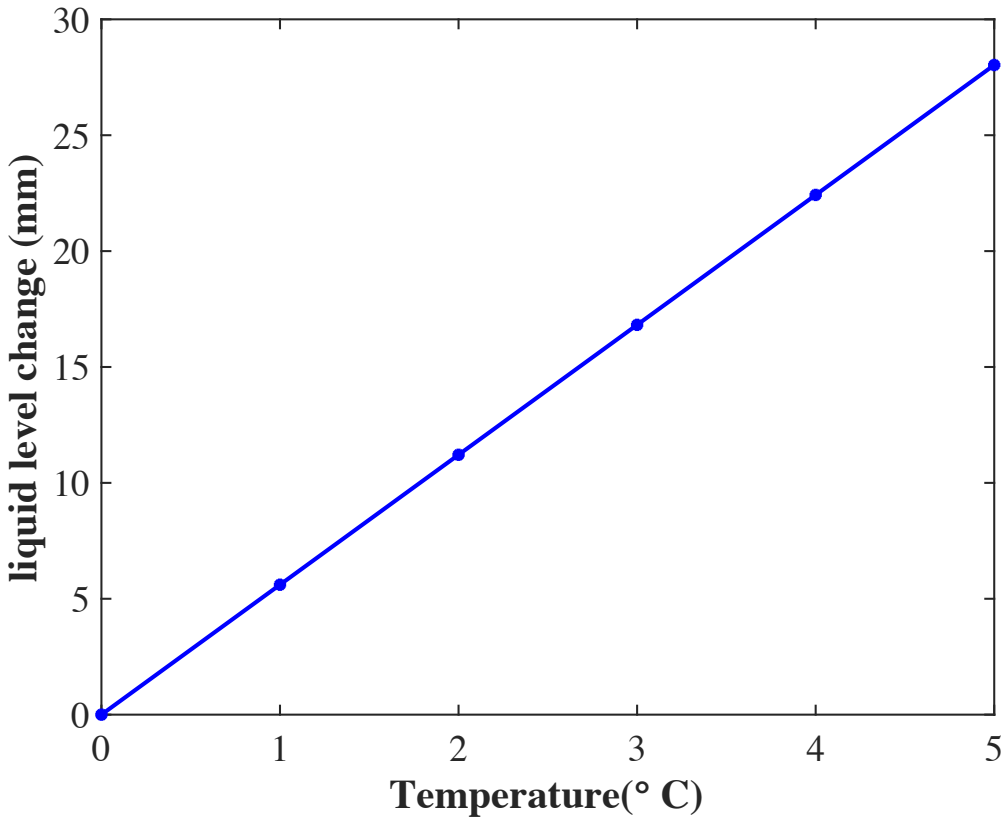

Figure 4.16. Simulation of the liquid level change under temperature deviation of the fabricated microfluidic device.

out of the MMI fiber sensor sensing range (which is equal to the length of coreless fiber), as shown in Fig.4.16. It is also observed that under temperature deviation, liquid level changed linearly. As such, this microfluidic device can be used independently for temperature sensing when pressure is fixed and for pressure sensing when temperature is fixed. In addition, three approaches could be applied to minimize the temperature crosstalk:

1) minimizing the size of reservoir, especially the height, and the low CTE material filling inside reservoir method. And the height of the reservoir should be larger than the maximum deflection of the pressure sensing diaphragm.

2) Reduce the cross-section of the reservoir, and at the same time, apply a thinner pressure sensing diaphragm. From the bottom pressure response equation, by simultaneously reducing reservoir diameter and thickness of diaphragm, the pressure response could be maintained the same (same pressure range and sensitivity), as shown in equation (2). In addition, according to equation (5), the temperature sensitivity could be reduced.

3) Longer coreless fiber is applied for liquid level interrogation.

4.2.6 IASM for pressure sensor with microfluidic-chip configuration

The proposed microfluidic device can also be fabricated based on a planar configuration to form a microfluidic chip, thanks to the design flexibility of glass 3D printing technique. To realize a microfluidic chip configuration, the printing model is composed of a channel and a connected reservoir as shown in Fig. 4.17(a). The sealing of the 3D printed structure is conducted by the same procedure as shown in Fig. 4.13(b) and Fig. 4.13(c). Similar to the liquid-in-glass thermometer configuration, the same glass

substrate (Corning 7980, with thickness of 100 μm) is placed between two glass pastes to cover the microfluidic chip structure. As such, it is the glass cover area in reservoir region that will dominate the inner volume change of the structure, performing the same functionality as the top diaphragm in Fig. 4.13(c). Fiber-optic sensors can be inserted at either side of the channel. And the liquid will be pumped from the other side to fill the reservoir area. Sealing will be conducted at both ends of the channel as the final step. Although two microfluidic devices are with two different configurations, the pressure sensing both rely on the deflection of the pressure sensing diaphragm. In addition, the liquid level amplification is realized by the cross-sectional ratio between the reservoir and channel. As such, it is anticipated that the pressure sensing performance should be similar.

Fig. 4.17(b) and Fig. 4.17(c) shows the 3D printed microfluidic chip structure. To further verify the sealing effect conducted by the 3D printing assisted sealing process as shown in Fig. 4.13(c), red liquid was inserted to fill the reservoir and the right side of the channel. As illustrated in Fig. 4.17 (b)-(c), liquid was confined inside the channel and reservoir, showing the good performance of the proposed sealing process. Additionally, SEM imaging was conducted to examine the bonding conditions realized by the proposed glass 3D printing assisted sealing process in Fig. 4.17(c). Fig. 4.17(d) and Fig. 4.17(e) shows SEM images of the microfluidic chip channel' s cross-sections. As indicated in Fig.4.17(d), the microfluidic channel maintains its shape and no cracks are observed on the glass cover. Additionally, Fig. 4.17(e) shows the zoomed-in image of the rectangular region in Fig. 4.17(d), where good bonding was realized, and integrated glass region was formed, showing the feasibility of this glass 3D printing assisted sealing process proposed

in Fig. 4.13(c). It is also observed that the shape of the cover glass changes. This phenomenon should be related to glass paste extrusion process, where glass cover was placed between two paste layers. And glass pastes would be extended to the glass cover area. After the laser melting process, glass pastes would be melted together with the cover glass. Nevertheless, the extension of glass pastes onto the glass cover contributes little to the inner channel volume change as shown in Fig. 4.17(d). The pressure response should be similar to the results expected in Equation (4.8), just like the pressure responses provided by the sensor with liquid-in-glass-thermometer shape in Figure 4.13.

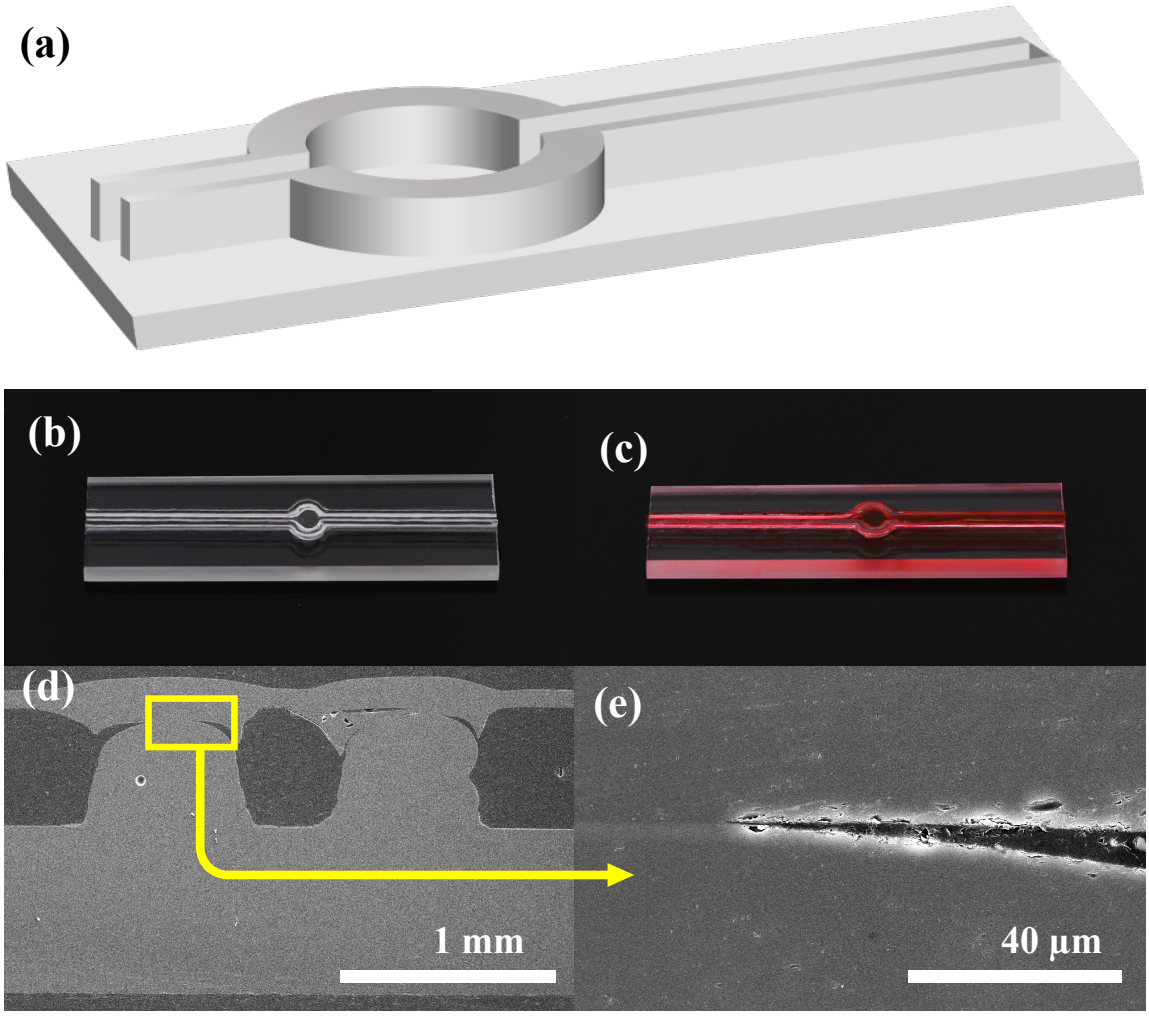

Figure 4.17. Schematic and images of the fabricated devices with microfluidic chip configuration. (a) 3D printing model. (b) Image of 3D printed structure and (c) microfluidic chip filled with red liquid. (d) and (e) SEM images of cross-sections of microfluidic chip's channels areas. (d) images showing that the microfluidic channel maintains its shape. (e) zoomed-in pictures of the rectangular area in (d) showing the good bonding between glass substrate and 3D printed glass.

4.2.7 Summary

In summary, a novel microfluidic device was fabricated by Integrated Additive and Subtractive Manufacturing (IASM). The microfluidic device consists of one capillary and a liquid reservoir. A reflection-mode multi-mode interference (MMI) structure is inserted into capillary for pressure sensing. Pressure response is investigated by testing it at a controlled temperature environment. And test results show that the pressure sensitivity was 0.062nm/kPa at fixed temperature environment.

Considering large coefficient of thermo expansion (CTE) difference between liquid and fused silica and relatively large size of the fabricated device, temperature sensitivity will be significant [96], [108], [110]. For this fabricated sensor, temperature change less than 10°C should introduce liquid level change covering the whole no-core fiber area and make it unstable for pressure measurement. Therefore, this microfluidic device can be used independently for temperature sensing when pressure is fixed and for pressure sensing when temperature is fixed. And temperature compensation units can be added, like a fiber Bragg grating in series with MMI region. Based on this novel IASM fabrication method, the pressure sensitivity of this device can be flexibly adjusted by tuning cross-section ratio between reservoir and tube. With this all-glass interface, good mechanical robustness and chemical resistance, it is believed that this microfluidic device is potentially useful for pressure measurement for biological and chemical applications, especially for specialized microfluidic systems.

CHAPTER FIVE

IASM for Information Integrated Module Fabrication

In this chapter, 3D printed fused silica glass have been applied to embed fiber-optic sensors for information integrated module fabrication. Thanks to the design flexibility of additive manufacturing process and the fabrication accuracy of subtractive manufacturing process, IASM of fused silica has been applied for in-situ embedding optical fiber sensors, providing a potential solution to solve the deficiency in sensor packaging and installation techniques in harsh condition applications.

5.1 Information integrated glass module fabricated by integrated additive and subtractive manufacturing

In this section, we report a novel integrated additive and subtractive manufacturing (IASM) method to fabricate information integrated glass module. After a certain number of glass layers are 3D printed and sintered by direct CO_2 laser irradiation, a microchannel will be fabricated on top of the printed glass by integrated picosecond laser, for intrinsic Fabry-Perot interferometer (IFPI) optical fiber sensor embedment. Then glass 3D printing process continues for the realization of bonding between optical fiber and printed glass. Temperature sensing up to 1000°C was demonstrated using the fabricated information integrated module. In addition, the long-term stability of the glass module at 1000°C was conducted. Enhanced sensor structure robustness and harsh temperature sensing capability makes this glass module attractive for harsh environment structural health monitoring.

5.1.1 Review of Sensor embedding technique

Compact, robust temperature sensors are increasingly necessary in industrial applications, such as engine turbines, downhole and boiler tubes, for temperature measurement to ensure consistent processes[24], [111]. Precise and in situ temperature monitoring is of great importance in these fields. With compact size and accurate reading capability, electrical thermometers like thermocouples and resistance temperature devices (RTD) have been widely applied in various applications. However, electrical thermometers cannot survive under harsh conditions (e.g., high temperature >600°C, high pressure and chemical corrosions). In addition, for temperature sensing in harsh conditions, extreme condition survivability and stability of sensors should be critical. As such, the entire sensing module should be built using high temperature materials for stable and reliable performance in harsh conditions.

Fiber-optic sensors have been widely demonstrated and applied for harsh environment applications. Compared with electronic sensors, fiber-optic sensors have the unique advantages of light weight, chemical resistance, high temperature resistance and distributed sensing capability[22], [24], [102], [104], [111]. Additionally, because of their immunity to electromagnetic interference (EMI), fiber optic sensors can be applied in strong EMI harsh environments [22]–[25], [28], [102], [104], [112], [113]. Over the past years various optical fiber sensors have been proposed and demonstrated for temperature sensing, such as fiber interferometers, long period fiber gratings, fiber Bragg gratings and optical fiber directional couplers [22], [23], [25], [36], [113], [114]. These sensors

generally operate by detecting the temperature-induced optical parameter changes such as intensity, wavelength and phase.

Phase/Wavelength-modulated fiber optic temperature sensors are more stable, easy to fabricate and interrogate[23], [25], [102]. Compared with the phase/wavelength-based temperature sensors, intensity-based fiber-optic sensors often have limitations due to their sensitivity to environmental changes such as the bending of optical fiber induced intensity change and source power vibrations[70]. Typically, a reflection mode probe-type configuration is preferred for temperature sensing with the advantage of easy installation during applications, enhanced robustness and improved signal stability. Among the many demonstrated reflection-mode based probes, the interferometer and grating based structures are among the most popular choices for temperature sensing and have been successfully developed and proven to be capable of operating in extreme conditions[11], [25], [70], [102].

Although fiber-optic sensors have shown quite effective temperature measurements, it is observed that the implementation is difficult due to the fragile nature of optical fiber, and the difficulty of mounting optical fibers into harsh environments like turbines and downhole. Compared with the conventional sensor packaging method, which is realized by attaching or mounting sensors on structures after being fabricated, additive manufacturing approach in sensor development has been initiated recently by directly embedding sensors into functional parts or smart structures to realize in situ measurement of parameters of interests. Optical fiber sensors have been demonstrated to be embedded in 3D printed ceramic and metal composites and shown the potential for high temperature

sensing applications[44], [114]–[116]. However, considering different material properties, especially the large difference of thermal expansion coefficient (CTE) between embedded structure and optical fiber, extra protective coating layers on fiber or external protectors may be necessary to avoid embedded fiber damage[44], [114], [115], [117].

Sharing the same material properties (e.g., CTE) as optical fiber, fused silica is the natural choice of material for fabricating fiber-optic sensor embedded structures. Recently, glass 3D printing utilizing CO_2 laser direct melting method has been demonstrated. It offers great flexibility and simplicity to produce desired 3D structures with no post-treatment and high temperature resistance[54]. And an all-glass pressure sensor has been reported utilizing this glass 3D printing method for high temperature application[102]. In this letter, an integrated additive and subtractive manufacturing (IASM) process is employed to embed intrinsic Fabry-Perot interferometer (IFPI) optical fiber sensor into 3D printed glass components for harsh environment application. The glass 3D printing technique allows rapid fabrication of desired glass structures. The integrated picosecond laser subtractive machining process, which presents higher fabrication accuracy, helps to create channel to place optical fiber sensor at desired position. And 3D printing process continues to seal optical fiber inside the channel and realize fabrication of the information integrated glass module. IFPI in-situ monitoring of glass 3D printing during embedding sensor process is presented. High temperature response and long-term stability at high temperature of this glass module is studied.

5.1.2 Design and fabrication process information integrated glass module

Figure 5.1 schematically illustrates the IASM fabrication process. Several glass layers are 3D printed on a fused silica substrate first, as shown in Fig.5.1(a). During each printing layer, glass pastes [54] are extruded following a line trace through an extruder

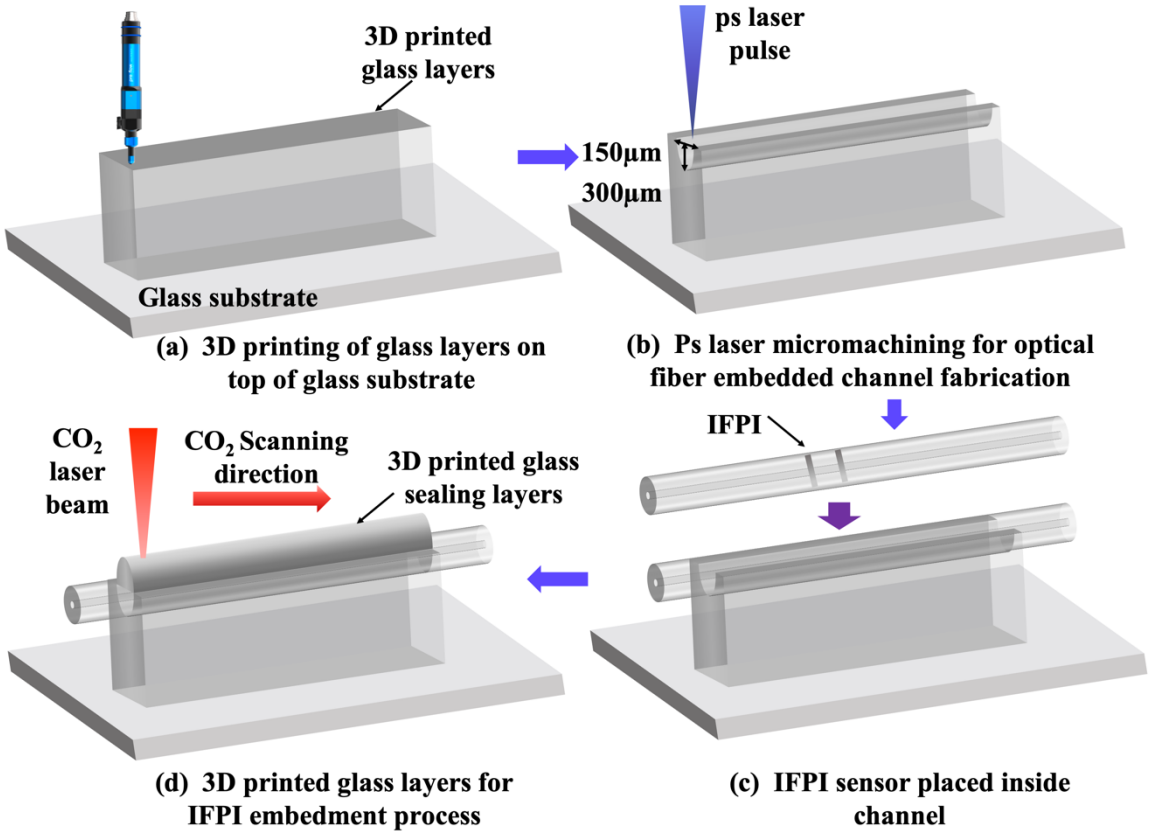

Figure 5.1 IASM for information integrated glass structure fabrication process. (a) Glass 3D printing on top of glass substrate. (b) integrated ps laser subtractive micromachining for micro-channel fabrication. (c) fiber-optic sensor placed and fixed inside the channel. (d) glass 3D printing conducted on top of the channel with optical fiber inside.

(eco-Pen300, Preeflow). And CO_2 laser irradiation (with wavelength of 10.6 μm, ti100W, Synrad) is conducted with optimized output power, scanning speed and spot size, for paste melting both in printing layer and between adjacent layers [54], [60], [61], [102], [118]. The glass 3D printing assisted with CO_2 laser direct melting procedure was described in details in our previous publications[54], [102]. After several layers of glass have been printed, an integrated picosecond laser subtractive micromachining system (Olive-1064-10; Attodyne, Inc. Toronto, ON, Canada, with wavelength of 1064nm) is applied for fabrication of the channel to place optical fiber. In this IASM system, glass 3D printing process presents the dimension accuracy on the order of tens or hundreds of microns. The addition of laser micromachining allows the fabrication of structures with micron dimension accuracy, showing the unique advantage of IASM system in high dimensional accuracy compared with traditional 3D printing process. More importantly, the high dimensional accuracy is necessary in embedding sensor process for sensors with micron size features. After the channel is fabricated, optical fiber IFPI sensor fabricated by femtosecond (fs) laser is placed and fixed inside the channel [21], as shown in Fig.5.1(c). Fig.5.1(d) shows the glass 3D printing for embedding optical fiber process. To ensure the fiber sensor is not damaged during the CO_2 laser melting process, multi-layers of glass pastes will be extruded on top of the embedded fiber sensor first. Then CO_2 laser irradiation with the same scanning parameters in previous glass 3D printing process [54], [102] will be applied to melt paste layers and bond the optical fiber with the surrounding glass, to ensure optical fiber being fixed and embedded.

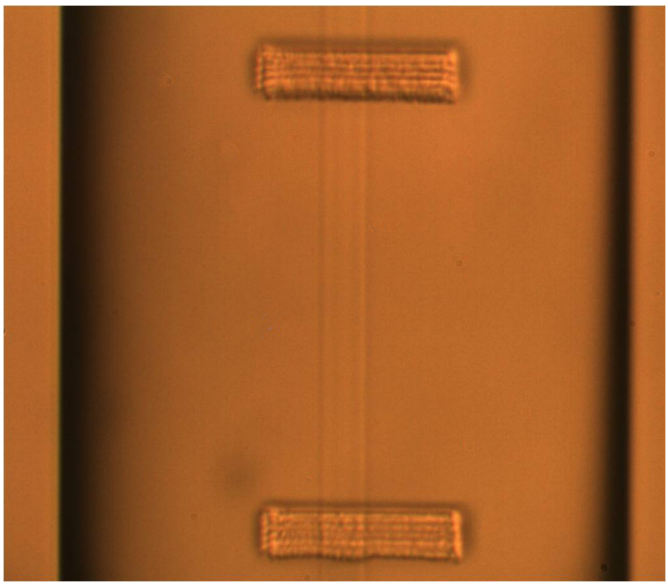

Figure 5.2. Microscope image of the fs laser inscribed IFPI.

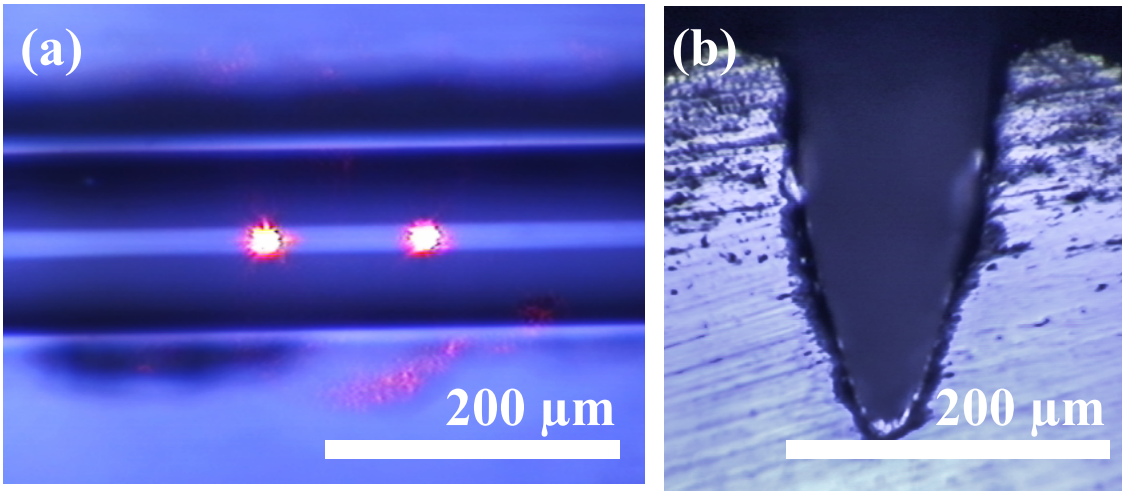

Figure 5.3 (a) IFPI sensor fixed inside the (b) ps laser micromachined channel on 3D printed glass structure, where two red dots indicate the IFPI location.

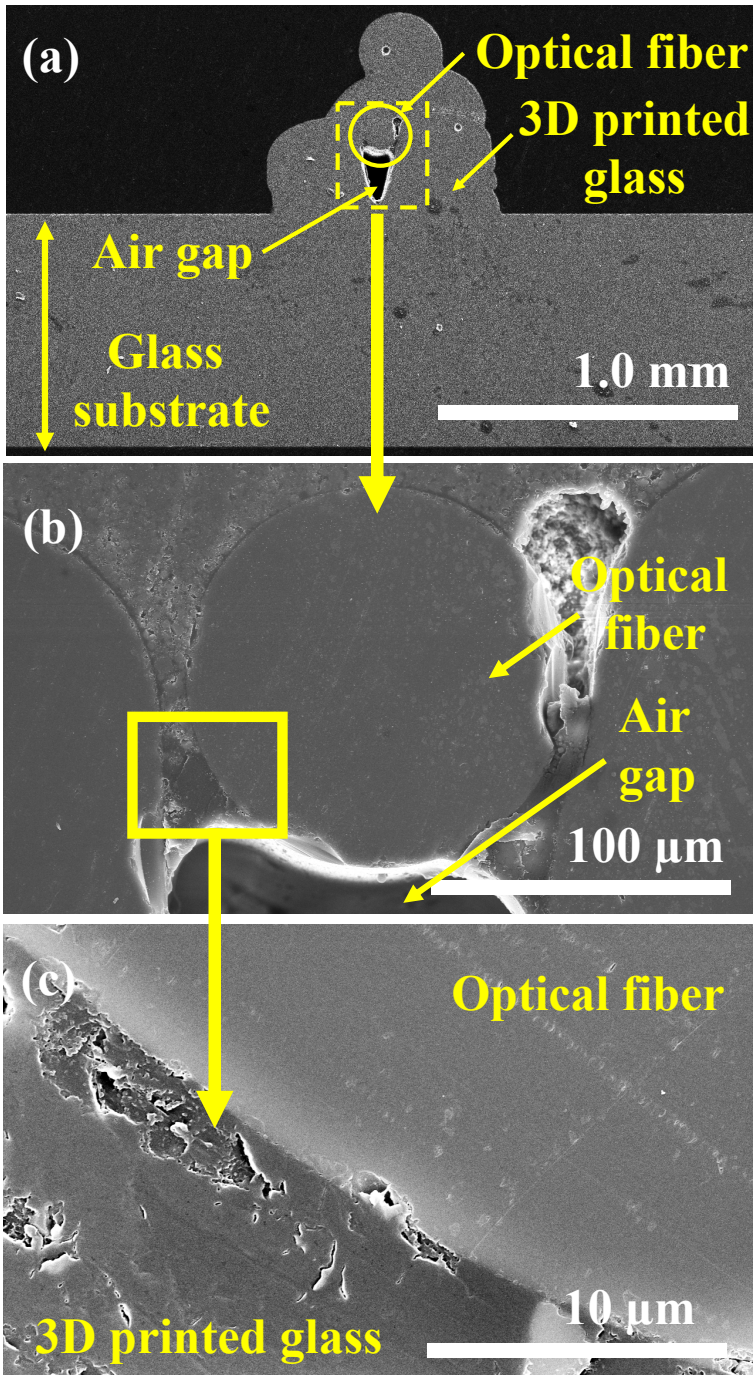

Figure 5.4 SEM image of (a) the cross-section of information integrated glass module (b) the embedded optical fiber region and (c) zoomed-in image of the rectangular area in (a) showing no gap and interface between the optical fiber and 3D printed glass.

5.1.3 Information integrated glass module experimental setup

The embedded IFPI was fabricated by inscribing two parallel lines in the fiber core with the Ti:sapphire fs laser (Coherent, Inc). The center wavelength, pulse width and repetition rate of the laser were 800 nm, 200 fs, and 250 kHz, respectively. The maximum output power was 1 W. The actual power used for fabrication was controlled by adjusting the laser beam optics, including a half-wave plate, a polarizer and several neutral density (ND) filters. The laser was switched on or off by electrically gating the internal clock. The actual laser energy used for fabrication was approximately 0.32 μJ per pulse. A water immersion lens (Olympus UMPlanFL 20x) was used to focus the fs laser beam into the fiber core. The entire cross section of the fiber core was covered by a cuboid region of 15x1x15, which was inscribed in the center of the fiber from bottom up. The scanning speed was 20. Fig. 5.2 shows the microscope image of an IFPI. The two parallel lines in the fiber core are clearly observed.

Fig. 5.3 and Fig. 5.4 illustrate the fabricated information integrated glass structure. After five glass layers (with a thickness of ~500 μm, and length of 2 cm) have been printed and melted on top of glass substrate, ps laser micromachining was applied to fabricate sensor placement channel with a dimension of 150 μm x 300 μm. Fig.5.3(a) shows the IFPI sensor, which was fabricated by femtosecond laser micromachining, was placed and fixed inside the ps laser fabricated V-groove channel, as shown in Fig.5.3(b), where the width at top was ~150 μm. To ensure IFPI region was placed inside the channel, a red laser pointer connecting to the sensor was used for IFPI location visualization. As shown in Fig.5.3(a), two red light spots are observed to indicate the locations of two IFPI reflection mirrors.

Then two layers of glass paste were extruded on top of channel with fixed sensor. Finally, CO_2 laser irradiation process was conducted following the channel direction for the top paste melting, the melting between top paste and adjacent layers, and the bonding between paste and fiber sensor.

Fig.5.4(a) shows the SEM image of cross-section of the glass module, where optical fiber is surrounded by 3D printed glass. Additionally, the large void underneath fiber was the unfilled region of the channel, which can be avoided through optimized ps laser ablation parameters. As shown in Fig.5.4(b)-(c), the interface between the optical fiber and 3D printed glass and no gap between them are clearly observed, indicating that the optical fiber was undamaged and maintained its integrity. Additionally, porous glass structure surrounding optical fiber was observed.

During the CO_2 laser melting process, the embedded optical fiber was connected to one optical sensing interrogator (SM125, Micron Optics) for in-situ spectra measurement. SM125 was controlled by a LabVIEW program to record spectra and calculate the IFPI cavity length in every 1.2 seconds. Fig.5.5(a) shows the cavity length change during CO_2 laser sintering process, where the output power of CO_2 laser was set to 11 W, and the scanning speed for sintering process was 1 mm/s. It is observed that IFPI cavity length was varying rapidly during sintering process, indicating the interaction between the pastes and laser irradiation (e.g., volume shrinkage of the glass pastes and melting of polymers of the glass paste), as well as the interaction between the paste under laser irradiation and optical

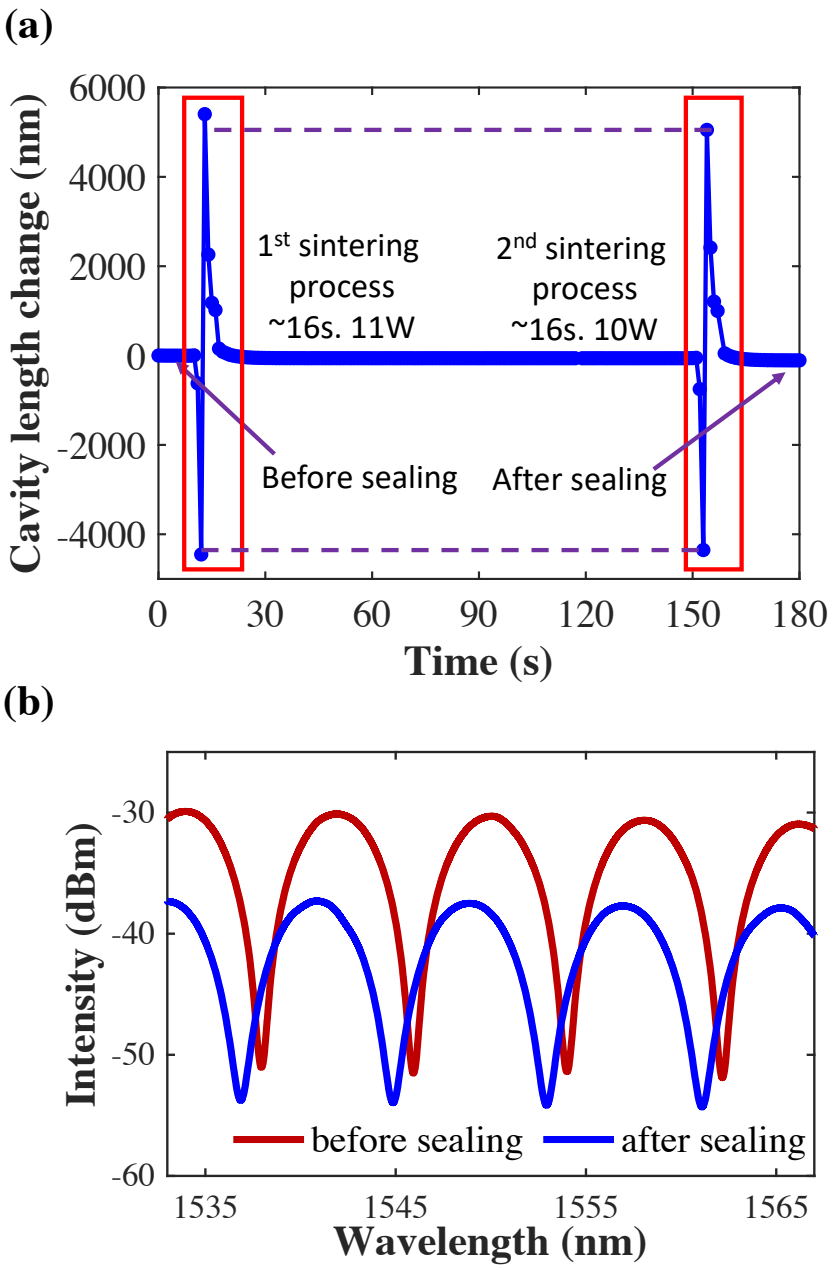

Figure 5.5 (a) In situ monitoring of the cavity length variation of embedded IFPI sensor during CO_2 laser melting process. (b) Interference spectra of the IFPI sensor before (red) and after (blue) sensor fabrication process, acceptable optical loss but no distortion of optical signal is observed.

fiber. After CO_2 laser sintering process and allowing the glass module to return to room temperature, cavity length was almost the same as the one before sintering process, showing that the IFPI was not damaged after the CO_2 irradiation process.

After the first CO_2 laser irradiation process, to make sure that the glass pastes were melted and good bonding was realized between optical fiber and melted fused silica, the second laser sintering process was conducted, with a lower laser output power (10 W) but the same scanning speed and spot size. Similar to the phenomena existing in the first sintering process, cavity length decreased first, then increased above the initial cavity length, and finally returned to almost same cavity length as the one before first sintering. Additionally, Fig.5.5(a) shows that the largest cavity length deviation during second sintering process was smaller compared to the one during the first sintering process. This observation should be related to a lower laser output power, smaller printed glass volume change in the second laser irradiation process after the formation of denser fused silica glass and the accomplished bonding between glass and optical fiber realized in the first one.

Fig.5.5(b) shows the spectra of embedded IFPI before and after laser sintering processes. After the glass module fabrication procedure, acceptable optical loss and no distortion of the optical signal were observed. The loss should be related to optical fiber micro-bending that may exist during the laser irradiation process. Considering the constant laser output during laser irradiation process, optical fiber would be under abrupt temperature change at the laser scanning starting and ending points, where optical fiber micro-bending may be easily formed. And scanning areas except starting and ending points were under same CO_2 laser irradiation profiles and were without sudden temperature

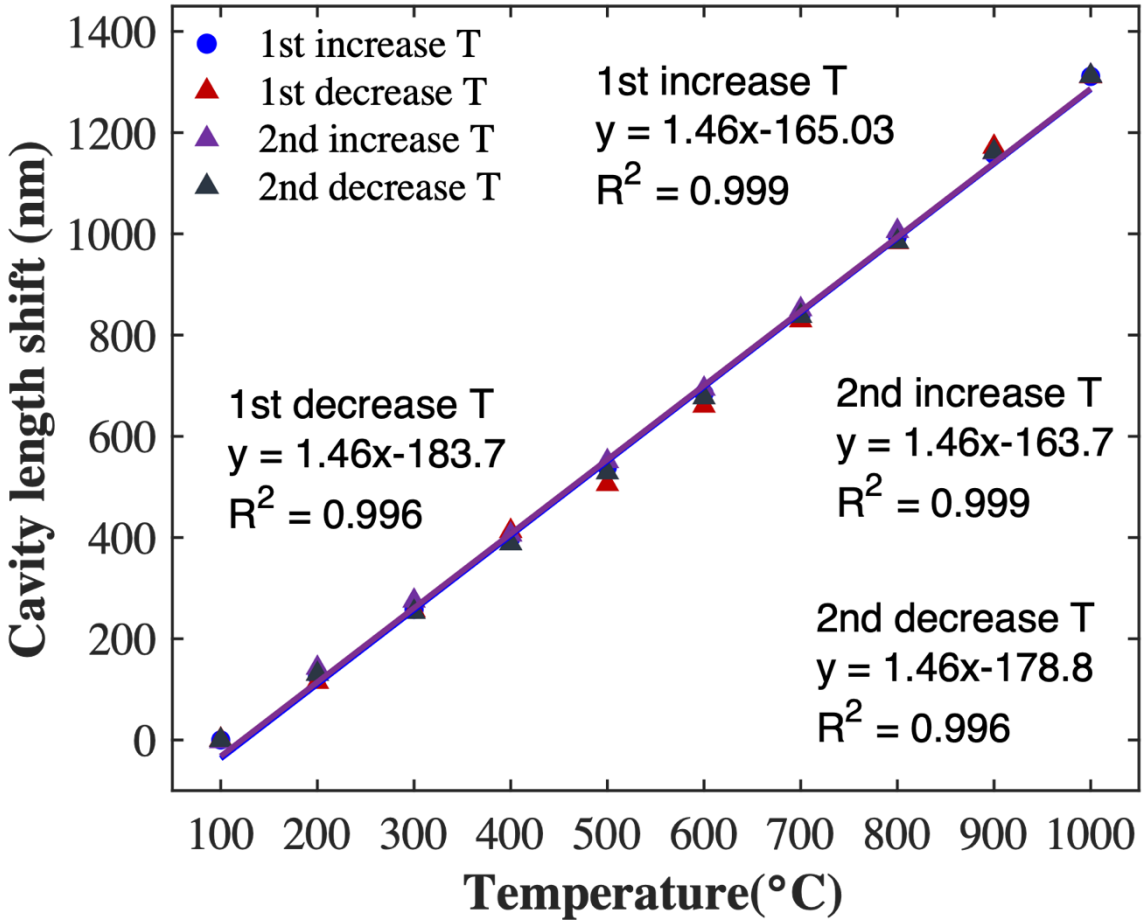

Figure 5.6 Temperature response of the information integrated glass module during two temperature cycles.

change. As such, IFPI region located in the center of scanning path was not damaged and IFPI patterns were not destructed, as shown in Fig.5.5(b). In addition, rough surface of printed porous glass surrounding optical fiber may contribute to optical fiber micro-bending and thus the optical loss.

The optical losses could be further decreased by optimizing the CO_2 laser scanning parameters and processes. For example, two-step laser irradiation processes can be

conducted, that is, preheating the pastes with a low laser output power first and repeating the process with increased laser power. Nevertheless, the clean interference pattern with a fringe visibility of about 16 dB shown in Fig.5.5(b) is adequate for most sensing applications.

5.1.4 Experiments and discussions

To demonstrate the feasibility for high temperature sensing applications, the fabricated information integrated glass module was placed into an electrical tubular furnace and the interference spectra were monitored when temperature varied from room temperature to 1000°C, at a step of 100°C. At each step, 10 min waiting time was set to ensure that furnace's temperature was stabilized. As the temperature increased, the cavity length increased, and the spectra were recorded by SM125. Cavity length shift as a function of temperature change was plotted in Fig.5.6. Fig.5.6 also presents the cavity length change during two temperature test cycles. Linear regression was applied to fit each response curve and the slopes were calculated as the temperature sensitivity, to be 1.46 nm/°C during the two temperature cycles. Experimental results show good repeatability of the fabricated glass module for high temperature measurement.

When information integrated glass module is under temperature variations, both the refractive index of the core (n_{core}) and length (L) of embedded IFPI will change due to the thermo-optic effect and thermo-expansion effect, respectively. The change in optical path difference (OPD) of the IFPI can be expressed as[25]:

$$\Delta OPD = OPD(\alpha_{CTO} + \alpha_{CTE})\Delta T \tag{5.1}$$

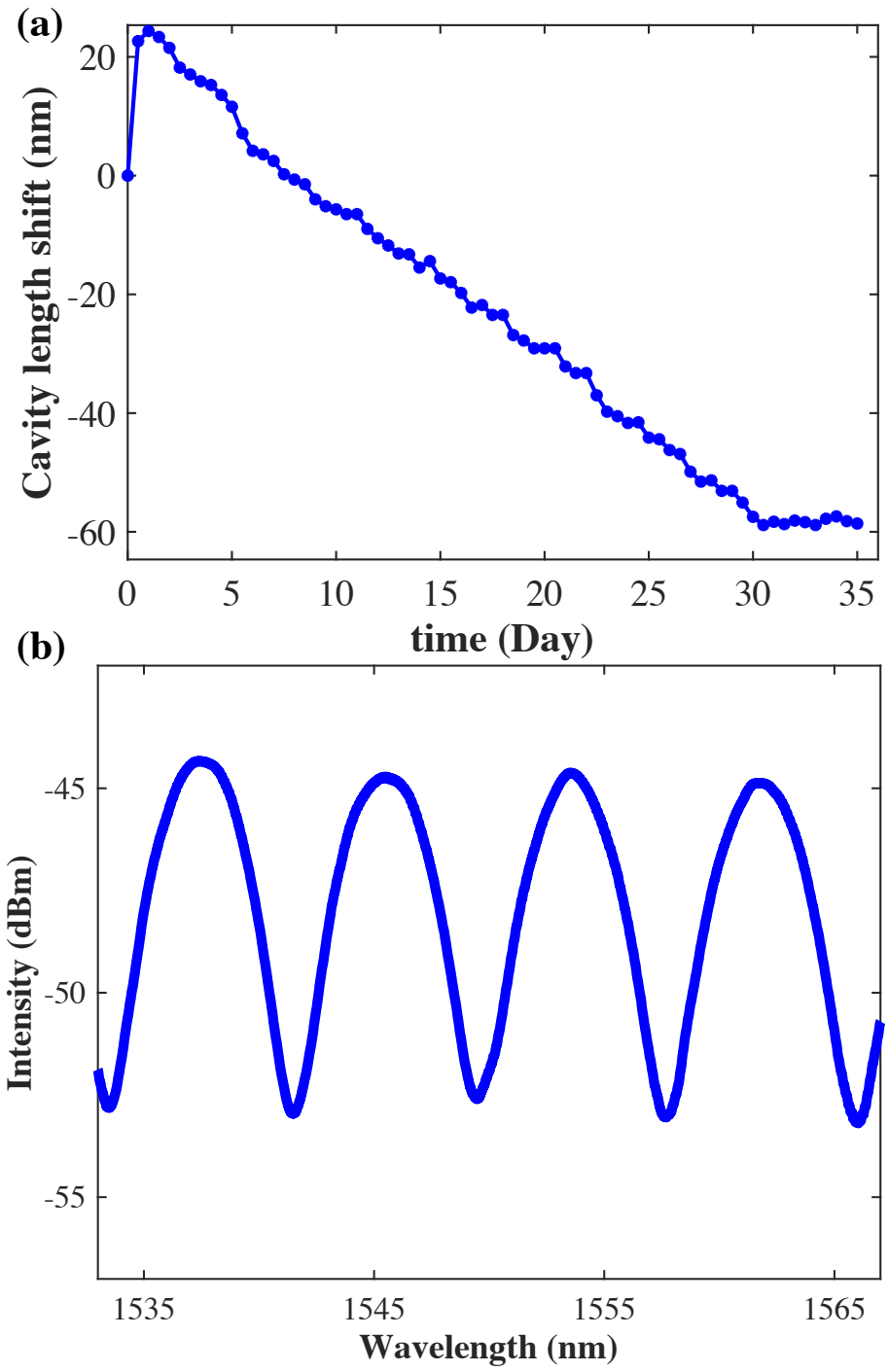

Figure 5.7. (a) 35-day stability test of glass module under 1000°C. (b) IFPI waveform after 35 days at 1000°C.

where α_{CTO} and α_{CTE} are the coefficient of thermo-optic (CTO) and coefficient of the thermo-expansion (CTE) of the optical fiber with typical values of $\alpha_{CTO}=8.3\times10^{-6}°C^{-1}$ and $\alpha_{CTE}=0.55\times10^{-6}°C^{-1}$, separately. Taking the IFPI' s cavity length of 148123.5 nm at 100°C into consideration, the bare IFPI temperature sensitivity is calculated according to Eq. (5.1) as 1.31 nm/°C, showing a small difference from the measurement sensitivity of 1.46 nm/°C. This difference should be related to thermal properties variation between the bare IFPI and embedded IFPI. Considering α_{CTO} of silica fiber should not change during the embedment process, the difference between measured and calculated temperature sensitivity corresponds to α_{CTE} difference between the commercial silica fiber and 3D printed glass.

Considering the forming of an integrated part realized by the good bonding between printed glass and optical fiber as shown in Fig.5.4(b) and (c), CTE of the embedded fiber and printed glass should be the same. And the dominated CTE during tests is the CTE of printed glass that surrounds fiber, which is $1.01\times10^{-6}°C^{-1}$. The comparatively larger α_{CTE} of 3D printed glass should be related to the porous structure due to the smaller laser irradiation power and the possible composite difference between the commercial glass/glass fiber and 3D printed glass[54]. The porosity of glass can be flexibly tuned by controlling thickness of top covering paste layers and precise laser processing parameter settings[60], [61]. The linear and repeatable temperature responses indicate good bonding between 3D printed glass and silica fiber was realized and the information integrated all-glass module is functional and suitable for high temperature measurements.

To evaluate long-term stability, temperature response of this module has been continuously monitored for 35 days at 1000°C. As shown in Fig.7(a), after quick settlement,

cavity length deviation continued to drift to -60nm (corresponding to ~40°C deviation) in 35-day period. About 8dB optical loss was observed after 35-day test. The interference fringes were still in good qualify as shown Fig.5.7(b). This phenomenon could be related to combined effects including property change of 3D printed fused silica at high temperature (e.g., annealing), thermal stability of IFPI fabricated by fs laser[119]. Detailed mechanism deserves future investigation.

5.1.5 Summary

In summary, an information integrated structure with an embedded IFPI sensor was fabricated by the novel Integrated Additive and Subtractive Manufacturing (IASM) method. Glass 3D printing assisted by CO_2 laser direct melting process was applied for flexible 3D structure fabrication. An integrated picosecond laser micromachining system was used for sensor embedded microchannel fabrication with high dimension accuracy. IFPI sensor was embedded in the glass module during fabrication process for in situ temperature monitoring. SEM images and repeatable high temperature responses indicate the bonding between the printed glass and optical fiber, and the feasibility of sensor embedment utilizing IASM method. The proposed information integrated glass module shows the enhanced mechanical robustness, good high temperature response, long term survivability at high temperature and is miniature in size, all of which make it attractive for high temperature harsh environment applications.

CHAPTER SIX

Conclusion

In summary, this dissertation focuses on the research of advanced glass additive and subtractive manufacturing for application in optical fiber sensors and devices fabrication. Five sensors with different working principles have been introduced in this dissertation.

Following are the specific achievements accomplished in this dissertation:

(1) Based on the unique, home-made and innovative integrated additive and subtractive manufacturing system, sensor and device fabrication process flows have been designed and developed. The system enables additive manufacturing for 3D printing and precise materials deposition at a specific location. For in-situ heating process, the system allows in-situ material processing. In addition, the system is capable of high-resolution laser machining. In this way, the additive and subtractive tools have been integrated into one system and applied for information integrated manufacturing process and information integrated device and sensor fabrication.

(2) An all-glass fiber-optic pressure sensor was fabricated by the three-dimensional printing based on direct laser melting method. The pressure sensor was made of all fused silica material, and its fiber housing structure was fabricated by direct three-dimensional (3D) printing of glass on top of a fused silica substrate, which also served as the pressure sensing diaphragm. A cleaved single-mode fiber (SMF) fixed inside a glass tube was inserted into the fiber housing structure and brought in close

proximity to the diaphragm, to form the FPI. And CO_2 laser irradiation was applied in thermal bonding process. Based on this 3D printing of glass method, the diaphragm thickness and diameter can be designed to adjust the sensitivity and measurement range. Besides, the sensor can work in high temperature environments. It is believed that this all-glass fiber-optic pressure sensor is potentially useful for pressure measurement in high temperature harsh environments.

(3) We propose an innovative method for fabricating glass and ceramic bi-layer structures, with the help of integrated laser machining method. Glass walls of different geometries can be fabricated using the extrusion-based 3D printing method. After each extrusion layer, CO_2 laser heat treatment will be processed for fused silica paste quick melting and fusing both in the printing layer and between the adjacent layers. After 3D printing of glass, ceramic layer is screen printed on side of the glass wall. And ceramic pattern can be flexibly designed and fabricated with picosecond laser ablation followed by CO_2 laser melting to satisfy different application requirements. To demonstrate the stability and functionality of the bi-layer ceramic and glass structure, a straight wall bi-layer strip was assembled together with an optical fiber to form a Fabry-Perot interferometer. And the FPI was demonstrated for high temperature measurement.

(4) By utilizing fluidic' s different properties, e.g., refractive index of the liquid and fluidity of liquid, the sensitivity of the fabricated sensors to the related parameters have been increased. Compared with the previously introduced all-glass sensors,

fluidic devices will be another candidate for sensing applications and possess high sensitivities. Specifically, a microfiber half coupler was investigated for RI sensing. The probe was made by cleaving a fused fiber directional coupler at the center of its taper region. When used for RI sensing, the reflection spectrum blue shifted as the surrounding RI increased.

(5) A novel fused silica microfluidic device with pressure sensing capability with high chemical and mechanical resistance that is fabricated by integrated additive and subtractive manufacturing (IASM) method. The sensor consists of a capillary and a 3D printed glass reservoir, where the reservoir volume change under pressure manifests liquid level deviation inside the capillary, thus realizing the conversion between small pressure change into large liquid level variation. Thanks to the design flexibility of this unique IASM method, the proposed microfluidic device is fabricated with liquid-in-glass thermometer configuration, where the reservoir is sealed following a novel 3D printing assisted glass bonding process. Liquid level is interrogated by a fiber-optic sensor based on multimode interference (MMI) effect.

(6) An information integrated structure with an embedded IFPI sensor was fabricated by the novel Integrated Additive and Subtractive Manufacturing (IASM) method. Glass 3D printing assisted by CO_2 laser direct melting process was applied for flexible 3D structure fabrication. An integrated picosecond laser micromachining system was used for sensor embedded microchannel fabrication with high dimension accuracy. IFPI sensor was embedded in the glass module during

fabrication process for in situ temperature monitoring. SEM images and repeatable high temperature responses indicate the bonding between the printed glass and optical fiber, and the feasibility of sensor embedment utilizing IASM method. The proposed information integrated glass module shows the enhanced mechanical robustness, good high temperature response, long term survivability at high temperature and is miniature in size, all of which make it attractive for high temperature harsh environment applications.

REFERENCE

[1] C. Pasten and J. C. Santamarina, "Energy and quality of life," *Energy Policy*, vol. 49, pp. 468–476, 2012.

[2] L. Nader and S. Beckerman, "Energy as it relates to the quality and stype of life," *Ann. Rev. Energy*, no. 3, pp. 1–28, 1978.

[3] J. G. Lambert, C. A. S. Hall, S. Balogh, A. Gupta, and M. Arnold, "Energy , EROI and quality of life," *Energy Policy*, vol. 64, pp. 153–167, 2014.

[4] H. Lund and B. V Mathiesen, "Energy system analysis of 100% renewable energy systems — The case of Denmark in years 2030 and 2050," *Energy*, vol. 34, pp. 524–531, 2009.

[5] A. Datta, R. Ganguly, and L. Sarkar, "Energy and exergy analyses of an externally fired gas turbine (EFGT) cycle integrated with biomass gasifier for distributed power generation," *Energy*, vol. 35, no. 1, pp. 341–350, 2010.

[6] S. J. Mihailov, "Fiber Bragg Grating Sensors for Harsh Environments," *Sensors*, vol. 12, pp. 1898–1918, 2012.

[7] I. García, J. Zubia, G. Durana, G. Aldabaldetreku, M. A. Illarramendi, and J. Villatoro, "Optical fiber sensors for aircraft structural health monitoring," *Sensors*, vol. 15, no. 7, pp. 15494–15519, 2015.

[8] J. Deng *et al.*, "Optical fiber sensor-based detection of partial discharges in power transformers," *Opt. Laser Technol.*, vol. 33, pp. 305–311, 2001.

[9] K. T. V Grattan and T. Sun, "Fiber optic sensor technology : an overview," *Sensors & Actuators*, vol. 82, pp. 40–61, 2000.

[10] A. Wang *et al.*, "Self-Calibrated Interferometric – Intensity-Based Optical Fiber Sensors," *J. Light. Technol.*, vol. 19, no. 10, pp. 1495–1501, 2001.

[11] L. Yuan *et al.*, "Femtosecond laser processing of transparent materials for assembly-free fabrication of photonic microsensors," in *Proc. SPIE 9735, Laser Applications in Microelectronic and Optoelectronic Manufacturing (LAMOM) XXI*, 2016.

[12] Y. Zhang, L. Yuan, X. Lan, A. Kaur, J. Huang, and H. Xiao, "High-temperature fiber-optic Fabry–Perot interferometric pressure sensor fabricated by femtosecond laser," *Opt. Lett.*, vol. 39, no. 1, p. 17, 2013.

[13] H. Li, D. Li, and G. Song, "Recent applications of fiber optic sensors to health monitoring in civil engineering," *Eng. Struct.*, vol. 26, pp. 1647–1657, 2004.

[14] M. Ramakrishnan, G. Rajan, Y. Semenova, and G. Farrell, "Overview of Fiber Optic Sensor Technologies for Strain / Temperature Sensing Applications in composite materials," *Sensors*, vol. 16, no. 99, 2016.

[15] T. L. Yeo, T. Sun, and K. T. . Grattan, "Fibre-optic sensor technologies for humidity and moisture measurement," *Sensors Actuators A. Phys.*, vol. 144, pp. 280–295, 2008.

[16] G. Priest, J. A. Bucaro, and S. C. Rashleigh, "Optical Fiber Sensor Technology," *IEEE tramsactions Microw. theory Tech.*, pp. 472–511, 1982.

[17] A. Leung, P. M. Shankar, and R. Mutharasan, "A review of fiber-optic biosensors," *Sensors Actuators, B Chem.*, vol. 125, no. 2, pp. 688–703, 2007.

[18] "Stimulated Optical Radiation in Ruby," *Nature*, 1960.

[19] J. C. Palais, *Fiber optic communications*. .

[20] V. Bhatia, “Optical fiber long-period grating sensors,” *Opt. Lett.*, vol. 21, no. 9, pp. 692–694, 1996.

[21] Y. Song *et al.*, “An IFPI Temperature Sensor Fabricated in an Unstriped Optical Fiber with Self-Strain-Compensation Function,” *J. Sensors*, vol. 6419623, 2016.

[22] Q. Zhang, J. Lei, B. Cheng, Y. Song, L. Hua, and H. Xiao, “A Microfiber Half Coupler for Refractive Index Sensing,” *IEEE Photonics Technol. Lett.*, vol. 29, no. 18, pp. 1525–1528, 2017.

[23] L. Yuan *et al.*, “Fiber inline Michelson interferometer fabricated by a femtosecond laser.,” *Opt. Lett.*, vol. 37, no. 21, pp. 4489–91, 2012.

[24] X. Wang, J. Xu, Y. Zhu, K. L. Cooper, and A. Wang, “All-fused-silica miniature optical fiber tip pressure sensor.,” *Opt. Lett.*, vol. 31, no. 7, pp. 885–7, 2006.

[25] Y. Zhang, J. Huang, X. Lan, L. Yuan, and H. Xiao, “Simultaneous measurement of temperature and pressure with cascaded extrinsic Fabry–Perot interferometer and intrinsic Fabry–Perot interferometer sensors,” *Opt. Eng.*, vol. 53, no. 6, p. 067101, 2014.

[26] B. Cheng, L. Hua, Q. Zhang, J. Lei, and H. Xiao, “Microwave-assisted frequency domain measurement of fiber-loop ring-down system,” *Opt. Lett.*, vol. 42, no. 7, 2017.

[27] H. Wang, L. Yuan, C.-W. Kim, J. Huang, X. Lan, and H. Xiao, “Integrated microsphere whispering gallery mode probe for highly sensitive refractive index measurement,” *Opt. Eng.*, vol. 55, no. 6, p. 067105, 2016.

[28] L. Hua *et al.*, “Phase Demodulation by Frequency Chirping in Coherence

Microwave Photonic Interferometry," *IEEE J. Sel. Top. quantum Electron.*, 2020.

[29] Q. Zhang *et al.*, "Application of glass 3D printing using direct laser melting for fabrication of photonic sensors," *Appl. Glas. 3D Print. using direct laser melting Fabr. photonic sensors," Proc. SPIE 11271, Laser 3D Manuf. VII, 112710S (2 March 2020)*, no. March, 2020.

[30] Q. Zhang *et al.*, "Reflection-mode fiber-optic temperature sensing probe based on quantum dots filled micro-cavity," *Proc. SPIE 11233, Opt. Fibers Sensors Med. Diagnostics Treat. Appl. XX, 112331F (20 Febr. 2020)*, no. February, 2020.

[31] X. Fan and I. M. White, "Optofluidic microsystems for chemical and biological analysis," *Nat. Publ. Gr.*, vol. 5, no. 10, pp. 591–597, 2011.

[32] X. Fang, C. R. Liao, and D. N. Wang, "Femtosecond laser fabricated fiber Bragg grating in microfiber for refractive index sensing.," *Opt. Lett.*, vol. 35, no. 7, pp. 1007–1009, 2010.

[33] M. Haque, K. K. C. Lee, S. Ho, L. A. Fernandes, and P. R. Herman, "Chemical-assisted femtosecond laser writing of lab-in-fibers," *Lab Chip*, vol. 14, pp. 3817–3829, 2014.

[34] Y. Yang, S. Saurabh, J. M. Ward, and S. Nic Chormaic, "High-Q, ultrathin-walled microbubble resonator for aerostatic pressure sensing," *Opt. Express*, vol. 24, no. 1, p. 294, 2016.

[35] Q. Yang *et al.*, "Fiber-Optic-Based Micro-Probe Using Hexagonal 1-in-6 Fiber Configuration for Intracellular Single-Cell pH Measurement," *Anal. Chem.*, vol. 87, no. 14, pp. 7171–7179, 2015.

[36] Q. Han *et al.*, "Long-period grating inscribed on concatenated double-clad and single-clad fiber for simultaneous measurement of temperature and refractive index," *IEEE Photonics Technol. Lett.*, vol. 24, no. 13, pp. 1130–1132, 2012.

[37] J. Huang, X. Lan, A. Kaur, H. Wang, L. Yuan, and H. Xiao, "Temperature compensated refractometer based on a cascaded SMS/LPFG fiber structure," *Sensors Actuators B. Chem.*, vol. 198, pp. 384–387, 2014.

[38] X. Lan *et al.*, "Reflection based extraordinary optical transmission fiber optic probe for refractive index sensing," *Sensors Actuators, B Chem.*, vol. 193, pp. 95–99, 2014.

[39] R. R. Gattass and E. Mazur, "Femtosecond laser micromachining in transparent materials," *Nat. Photonics*, vol. 2, 2008.

[40] K. A. Robert and M. B. Thompson, "Finer features for functional microdevices," *Nature*, vol. 412, pp. 697–698, 2001.

[41] S. Mueller, B. Kruck, and P. Baudisch, "LaserOrigami : Laser-Cutting 3D Objects," *CHI 2013 Chang. Perspect. Paris, Fr.*, pp. 2585–2592, 2013.

[42] B. Lee, S. Roh, and J. Park, "Optical Fiber Technology Current status of micro- and nano-structured optical fiber sensors," *Opt. Fiber Technol.*, vol. 15, no. 3, pp. 209–221, 2009.

[43] D. Psaltis, S. R. Quake, and C. Yang, "Developing optofluidic technology through the fusion of microfluidics and optics," *Nature*, vol. 442, no. July, pp. 381–386, 2006.

[44] A. Ghazanfari, W. Li, M. C. Leu, Y. Zhuang, and J. Huang, "Advanced ceramic components with embedded sapphire optical fiber sensors for high temperature

applications," *Mater. Des.*, vol. 112, pp. 197–206, 2016.

[45] J. Klein *et al.*, "Additive Manufacturing of Optically Transparent Glass," *Glas. 3D Print.*, vol. 2, no. 3, pp. 92–105, 2015.

[46] F. Kotz *et al.*, "Three-dimensional printing of transparent fused silica glass," *Nature*, vol. 544, no. 7650, pp. 337–339, 2017.

[47] D. T. Nguyen *et al.*, "3D-Printed Transparent Glass," *Adv. Mater.*, vol. 1701181, pp. 1–5, 2017.

[48] Y. Xu *et al.*, *The Boom in 3D-Printed Sensor Technology*, vol. 17, no. 5. 2017.

[49] C. Schubert, M. C. Van Langeveld, and L. A. Donoso, "Innovations in 3D printing : a 3D overview from optics to organs," *Innovations*, pp. 159–161, 2014.

[50] Y. Hong *et al.*, "Fabricating ceramics with embedded microchannels using an integrated additive manufacturing and laser machining method," *J. Am. Ceram. Soc.*, vol. 102, no. 3, pp. 1071–1082, 2019.

[51] M. C. Leu and A. Arbor, "Additive Manufacturing : Current State , Future Potential , Gaps and Needs , and Recommendations," *J. Manuf. Sci. Eng.*, vol. 137, no. February, pp. 1–10, 2015.

[52] M. Attaran, "The rise of 3-D printing : The advantages of additive manufacturing over traditional manufacturing," *Bus. Horiz.*, vol. 60, no. 5, pp. 677–688, 2017.

[53] S. V Murphy and A. Atala, "review 3D bioprinting of tissues and organs," *Nat. Publ. Gr.*, vol. 32, no. 8, pp. 773–785, 2014.

[54] J. Lei, Y. Hong, Q. Zhang, F. Peng, and H. Xiao, "Additive Manufacturing of Fused Silica Glass Using Direct Laser Melting," *CLEO Appl. Technol.*, no. AW31-4, pp.

4–5, 2019.

[55] X. Wang, M. Jiang, Z. Zhou, J. Gou, and D. Hui, “3D printing of polymer matrix composites : A review and prospective,” *Compos. Part B*, vol. 110, pp. 442–458, 2017.

[56] C. L. Manzanares Palenzuela and M. Pumera, “(Bio)Analytical chemistry enabled by 3D printing: Sensors and biosensors,” *Trends Anal. Chem.*, vol. 103, pp. 110–118, 2018.

[57] S. Z. Guo, K. Qiu, F. Meng, S. H. Park, and M. C. McAlpine, “3D Printed Stretchable Tactile Sensors,” *Adv. Mater.*, vol. 29, no. 27, pp. 1–8, 2017.

[58] C. L. M. Palenzuela and M. Pumera, “(Bio)Analytical chemistry enabled by 3D printing : Sensors and biosensors,” *Trends Anal. Chem.*, vol. 103, pp. 110–118, 2018.

[59] Q. Zhang, J. Lei, Y. Chen, Y. Wu, C. Chen, and H. Xiao, “3D Printing of All-Glass Fiber-Optic Pressure Sensor for High Temperature Applications,” *IEEE Sens. J.*, vol. 19, no. 23, pp. 11242–11246, 2019.

[60] J. Lei *et al.*, “Thick Er-doped silica fi lms sintered using CO 2 laser for scintillation applications,” *Opt. Mater. (Amst).*, vol. 68, pp. 63–69, 2017.

[61] J. Lei *et al.*, “The effect of laser sintering on the microstructure , relative density , and cracking of sol - gel – derived silica thin films,” *J. Am. Ceram. Soc.*, vol. 103, no. November 2018, pp. 70–81, 2020.

[62] R. Di Sante, “Fibre optic sensors for structural health monitoring of aircraft composite structures: Recent advances and applications,” *Sensors*, vol. 15, no. 8, pp. 18666–18713, 2015.

[63] J. Huang, Z. Zhou, D. Zhang, and Q. Wei, "A fiber bragg grating pressure sensor and its application to pipeline leakage detection," *Adv. Mech. Eng.*, vol. 2013, 2013.

[64] W. J. Pulliam, P. M. Russler, and R. S. Fielder, "High-temperature high-bandwidth fiber optic MEMS pressure-sensor technology for turbine-engine component testing," *Proc. SPIE, Fiber Opt. Sens. Technol. Appl. 2001*, vol. 4578, no. May, pp. 229–238, 2002.

[65] H. Y. Fu *et al.*, "High pressure sensor based on photonic crystal fiber for downhole application," *Appl. Opt.*, vol. 49, no. 14, p. 2639, 2010.

[66] C. Zhu, Y. Chen, Y. Zhuang, G. Fang, X. Liu, and J. Huang, "Optical Interferometric Pressure Sensor Based on a Buckled Beam with Low-Temperature Cross-Sensitivity," *IEEE Trans. Instrum. Meas.*, vol. 67, no. 4, pp. 950–955, 2018.

[67] A. Leal-Junior, A. Frizera, C. Díaz, C. Marques, M. Ribeiro, and M. J. Pontes, "Material features based compensation technique for the temperature effects in a polymer diaphragm-based FBG pressure sensor," *Opt. Express*, vol. 26, no. 16, p. 20590, 2018.

[68] J. Berthold, "Historical review of microbend fiber-optic sensors," *J. Light. Technol.*, vol. 13, no. 7, 1995.

[69] Y. Zhang, J. Huang, X. Lan, L. Yuan, and H. Xiao, "Simultaneous measurement of temperature and pressure with cascaded extrinsic Fabry–Perot interferometer and intrinsic Fabry–Perot interferometer sensors," *Opt. Eng.*, vol. 53, no. 6, p. 67101, 2014.

[70] J. Liu *et al.*, "Micro-cantilever-based fiber optic hydrophone fabricated by a

femtosecond laser," *Opt. Lett.*, vol. 42, no. 13, p. 2459, 2017.

[71] N. Bhattacharjee, A. Urrios, S. Kang, and A. Folch, "The upcoming 3D-printing revolution in microfluidics," *Lab Chip*, vol. 16, no. 10, pp. 1720–1742, 2016.

[72] J. Li *et al.*, "Fabricating optical fibre-top cantilevers for temperature sensing," *Meas. Sci. Technol.*, vol. 25, no. 035206, 2014.

[73] X. Fan, I. M. White, S. I. Shopova, H. Zhu, J. D. Suter, and Y. Sun, "Sensitive optical biosensors for unlabeled targets: A review," *Anal. Chim. Acta*, vol. 620, no. 1–2, pp. 8–26, 2008.

[74] O. S. Wolfbeis, "Fiber-Optic Chemical Sensors and Biosensors," *Anal. Chem.*, vol. 80, no. 12, pp. 4269–4283, 2008.

[75] L. Yuan, J. Huang, X. W. Lan, H. Z. Wang, L. Jiang, and H. Xiao, "All-in-fiber optofluidic sensor fabricated by femtosecond laser assisted chemical etching," *Opt. Lett.*, vol. 39, no. 8, pp. 2358–2361, 2014.

[76] T. Wei, Y. Han, Y. Li, H.-L. Tsai, and H. Xiao, "Temperature-insensitive miniaturized fiber inline Fabry-Perot interferometer for highly sensitive refractive index measurement.," *Opt. Express*, vol. 16, no. 8, pp. 5764–5769, 2008.

[77] Y. Du, S. Jothibasu, Y. Zhuang, C. Zhu, and J. Huang, "Chemical Rayleigh backscattering based macrobending single mode fiber for distributed refractive index sensing," *Sensors Actuators, B Chem.*, vol. 248, pp. 346–350, 2017.

[78] A. Iadicicco, A. Cusano, S. Campopiano, A. Cutolo, and M. Giordano, "Thinned fiber Bragg gratings as refractive index sensors," *IEEE Photonics Technol. Lett.*, vol. 16, no. 4, pp. 1149–1151, 2004.

[79] W. Liang, Y. Huang, Y. Xu, R. K. Lee, and A. Yariv, "Highly sensitive fiber Bragg grating refractive index sensors," *Appl. Phys. Lett.*, vol. 86, p. 151122, 2005.

[80] J. Huang, X. Lan, A. Kaur, H. Wang, L. Yuan, and H. Xiao, "Reflection-based phase-shifted long period fiber grating for simultaneous measurement of temperature and refractive index," *Opt. Eng.*, vol. 52, no. 1, p. 014404, 2013.

[81] J. Zhao *et al.*, "Surface plasmon resonance refractive sensor based on silver-coated side-polished fiber," *Sensors Actuators, B Chem.*, vol. 230, pp. 206–211, 2016.

[82] D. Liu *et al.*, "High sensitivity refractive index sensor based on a tapered small core single-mode fiber structure," *Opt. Lett.*, vol. 40, no. 17, pp. 4166–4169, 2015.

[83] D. K. C. Wu, B. T. Kuhlmey, and B. J. Eggleton, "Ultrasensitive photonic crystal fiber refractive index sensor," *Opt. Lett.*, vol. 34, no. 3, pp. 322–324, 2009.

[84] L. Bo, P. Wang, Y. Semenova, and G. Farrell, "High Sensitivity Fiber Refractometer Based on an Optical Microfiber Coupler," *IEEE Photonics Technol. Lett.*, vol. 25, no. 3, pp. 228–230, 2013.

[85] F. Chiavaioli, F. Baldini, S. Tombelli, C. Trono, and A. Giannetti, "Biosensing with optical fiber gratings," *Nanophotonics*, vol. 0, no. 0, 2017.

[86] Y. Chen, S. Yan, X. Zheng, F. Xu, and Y. Lu, "A miniature reflective micro-force sensor based on a microfiber coupler," *Opt. Express*, vol. 22, no. 3, pp. 757–759, 2014.

[87] M. Ding, P. Wang, and G. Brambilla, "A microfiber coupler tip thermometer," *Opt. Express*, vol. 20, no. 5, pp. 5273–5278, 2012.

[88] S. Yan, Y. Chen, C. Li, F. Xu, and Y. Lu, "Differential twin receiving fiber-optic

magnetic field and electric current sensor utilizing a microfiber coupler," *Opt. Express*, vol. 23, no. 7, pp. 24326–24331, 2015.

[89] L. Luo, S. Pu, J. Tang, X. Zeng, and M. Lahoubi, "Highly sensitive magnetic field sensor based on microfiber coupler with magnetic fluid," *Appl. Phys. Lett.*, vol. 106, p. 193507, 2015.

[90] S. Pu, L. Luo, J. Tang, L. Mao, and X. Zeng, "Ultrasensitive Refractive-Index Sensors Based on Tapered Fiber Coupler With Sagnac Loop," *IEEE Photonics Technol. Lett.*, vol. 28, no. 10, pp. 1073–1076, 2016.

[91] W. Lin *et al.*, "Magnetically controllable wavelength-division- multiplexing fiber coupler," *Opt. Express*, vol. 23, no. 9, pp. 113–119, 2015.

[92] Y. Zhang *et al.*, "Fringe visibility enhanced extrinsic Fabry-Perot interferometer using a graded index fiber collimator," *IEEE Photonics J.*, vol. 2, no. 3, pp. 469–481, 2010.

[93] J. E. Sauders, C. Sanders, H. Chen, and H.-P. Loock, "Refractive indices of common solvents and solutions at 1550 nm," *Appl. Opt.*, vol. 55, no. 4, 2016.

[94] F. Chiavaioli, C. A. J. Gouveia, P. A. S. Jorge, and F. Baldini, "Towards a Uniform Metrological Assessment of Grating-Based Optical Fiber Sensors : From Refractometers to Biosensors," *Biosensors*, vol. 7, no. 23, 2017.

[95] C. Wu, W. Liao, and Y. Tung, "Integrated ionic liquid-based electrofluidic circuits for pressure sensing within polydimethylsiloxane microfluidic systems," *Lab Chip*, vol. 11, pp. 1740–1746, 2011.

[96] S. Agaoglu, P. Diep, M. Martini, S. Kt, M. Baday, and I. E. Araci, "Ultra-sensitive

microfluidic wearable strain sensor for intraocular pressure monitoring," *Lab Chip*, vol. 18, pp. 3471–3483, 2018.

[97] W. Song and D. Psaltis, "Optofluidic pressure sensor based on interferometric imaging," *Opt. Lett.*, vol. 35, no. 21, pp. 3604–3606, 2010.

[98] H. An, L. Chen, X. Liu, B. Zhao, H. Zhang, and Z. Wu, "Microfluidic contact lenses for unpowered , continuous and non-invasive intraocular pressure monitoring," *Sensors Actuators A. Phys.*, vol. 295, pp. 177–187, 2019.

[99] G. M. Whitesides, "The origins and the future of microfluidics," *Nature*, vol. 442, no. July, 2006.

[100] A. C. Fernandes, K. V Gernaey, and U. Krühne, "' Connecting worlds – a view on microfluidics for a wider application ,'" *Biotechnol. Adv.*, vol. 36, no. 4, pp. 1341–1366, 2018.

[101] R. Mukhopadhyay, "When PDMS isn't the best," *Anal. Chem.*, vol. 79, pp. 3248–3253, 2007.

[102] Q. Zhang, J. Lei, Y. Chen, Y. Wu, C. Chen, and H. Xiao, "3D printing of all-glass fiber-optic pressure sensor for high temperature application," *IEEE Sens. J.*, vol. PP, no. c, p. 1, 2019.

[103] F. Kotz *et al.*, "Fabrication of arbitrary three-dimensional suspended hollow microstructures in transparent fused silica glass," *Nat. Commun.*, vol. 10, p. 1439, 2019.

[104] L. Hua, Y. Song, B. Cheng, W. Zhu, Q. Zhang, and H. Xiao, "Coherence-length-gated distributed optical fiber sensing based on microwave-photonic interferometry,"

Opt. Express, vol. 25, no. 25, pp. 31362–31376, 2017.

[105] M. S. Cheri, H. Latif, J. Sadeghi, M. S. Moghaddam, H. Shahraki, and H. Hajghassem, "Real-time measurement of flow rate in mcirofluidc devices using a cantilever-based optofluidic sensor," *Analyst*, vol. 139, pp. 431–438, 2014.

[106] L. Yuan, J. Huang, X. Lan, H. Wang, L. Jiang, and H. Xiao, "All-in-fiber optofluidic sensor fabricated by femtosecond laser assisted chemical etching," *Opt. Lett.*, vol. 39, no. 8, pp. 2358–2361, 2014.

[107] Q. Zhang, J. Lei, Y. Chen, Y. Wu, and H. Xiao, "Glass 3D Printing of Microfluidic Pressure Sensor Interrogated by Fiber-Optic Refractometry," *IEEE Photonics Technol. Lett.*, vol. 32, no. 7, pp. 414–417, 2020.

[108] W. Zhu, B. Cheng, Y. Li, R. Nygaard, and H. Xiao, "A Fluidic-Based High-Pressure Sensor Interrogated by Microwave Fabry-Perot Interferometry," *IEEE Sens. J.*, vol. 17, no. 14, pp. 4388–4393, 2017.

[109] M. Bao, "Mechanics of Beam and Diaphragm Structures," *Anal. Des. Princ. MEMS Devices*, pp. 33–114, 2005.

[110] C. Li *et al.*, "Liquid level measurement based on a no-core fiber with temperature compensation using a fiber Bragg grating," *Sensors Actuators A. Phys.*, vol. 245, pp. 49–53, 2016.

[111] J. M. López-Higuera, L. R. Cobo, A. Q. Incera, and A. Cobo, "Fiber optic sensors in structural health monitoring," *J. Light. Technol.*, vol. 29, no. 4, pp. 587–608, 2011.

[112] J. Huang *et al.*, "Microwave Interrogated Sapphire Fiber Michelson Interferometer for High Temperature Sensing," *IEEE Photonics Technol. Lett.*, vol. 27, no. 13, pp.

1398–1401, 2015.

[113] D. Hu *et al.*, “Acoustic Fiber Bragg Grating and Its Application in High Temperature Sensing,” *IEEE Sens. J.*, vol. 18, no. 23, pp. 9576–9583, 2018.

[114] D. Havermann, J. Mathew, W. N. Macpherson, R. R. J. Maier, and D. P. Hand, “Temperature and Strain Measurements With Fiber Bragg Gratings Embedded in Stainless Steel 316,” *J. Light. Technol.*, vol. 33, no. 12, pp. 2474–2479, 2015.

[115] C. M. Petrie, N. Sridharan, M. Subramanian, A. Hehr, M. Norfolk, and J. Sheridan, “Embedded metallized optical fibers for high temperature applications,” *Smart Mater. Struct.*, vol. 28, no. 055012, p. 12pp, 2019.

[116] J. Lei, Q. Zhang, Y. Song, J. Tang, J. Tong, and F. Peng, “Laser-assisted embedding of all-glass optical fi ber sensors into bulk ceramics for high-temperature applications,” *Opt. Laser Technol.*, vol. 128, no. February, p. 106223, 2020.

[117] Q. Zhang *et al.*, “Information integrated glass module fabricated by integrated additive and subtractive manufacturing,” *Opt. Lett.*, vol. 45, no. 7, pp. 1–4, 2020.

[118] Q. Zhang, J. Lei, J. Tang, Y. Wu, L. Hua, and H. Xiao, “Information integrated glass module fabricated by integrated additive and subtractive manufacturin,” *Opt. Lett.*, 2020.

[119] D. Grobnic, C. W. Smelser, S. J. Mihailov, and R. B. Walker, “Long-term thermal stability tests at 1000C of silica fibre Bragg gratings made with ultrafast laser radiation,” *Meas. Sci. Technol.*, no. 17, pp. 1009–1013, 2006.